UNIVERSITY OF CALGARY

Analysis of microseismic event picking with applications to landslide and oil-field monitoring settings

by

Kimberly Anne Munro

A THESIS
SUBMITTED TO THE FACULTY OF GRADUATE STUDIES
IN PARTIAL FULFILMENT OF THE REQUIREMENTS FOR THE
DEGREE OF MASTER OF SCIENCE

DEPARTMENT OF GEOLOGY AND GEOPHYSICS

CALGARY, ALBERTA

June, 2005

UNIVERSITY OF CALGARY

FACULTY OF GRADUATE STUDIES

The undersigned certify that they have read, and recommend to the Faculty of Graduate Studies for acceptance, a thesis entitled " Analysis of microseismic event picking with applications to landslide and oil-field monitoring settings" submitted by Kimberly Anne Munro in partial fulfilment of the requirements of the degree of Master of Science.

Supervisor, Dr. Robert Stewart, Department of Geology and Geophysics

Co-Supervisor, Dr. Larry Lines, Department of Geology and Geophysics

Dr. Donald Lawton, Department of Geology and Geophysics

Dr. Jocelyn Grozic, Department of Civil Engineering

Date

Abstract

The methods considered for microseismic event detection consist of energy, multi-window, autoregressive-Akaike Information Criterion (AR-AIC) and S-transform techniques. Synthetic seismic data were developed to analyze each method under various conditions. The application of an onset time correction resulted in the energy and multi-window techniques selecting waves to within 1ms and 0.01ms, respectively. The energy and multi-window techniques were found unsuitable for detecting the P-and S-wave arrivals in low signal-to-noise ratio environments.

Having obtained sound results with the synthetic data, specific methods were applied to data acquired in an oilfield at Cold Lake, Alberta and in an unstable topographic area at Turtle Mountain, Alberta. While the AR-AIC and S-transform techniques resolved emergent events from Turtle Mt., the multi-window technique had much more accurate results on the few events it could detect. The energy and multi-window procedures had difficulties detecting the S-wave arrivals at Cold Lake as a result of the amplitudes being clipped.

Acknowledgements

I would like to take this opportunity to show gratitude to those who have assisted in my research. I am thankful to the sponsors of CREWES for their financial support and for the technical assistance from Henry Bland and Kevin Hall at the University of Calgary. I would like to show appreciation to Dr. Zuolin Chen in the CREWES project at the University of Calgary and express gratitude to Richard Smith and Dr. Colum Keith at Esso for sharing their insights. As well, I am appreciative of Pierre Lemire and Dr. Rob Pinnegar at Calgary Scientific for evaluating the S-transforms of my synthetic data and data acquired from Turtle Mt., Alberta. Many thanks are expressed towards Drs. Larry Lines, Rob Stewart, and Ed Krebes at the University of Calgary for their time and encouragement.

I would like to show appreciation to Amber Kelter and Chad Hogan for their time and sharing of knowledge.

Table of Contents

List of Tables

List of Figures

CHAPTER ONE: Introduction

1.1 Motivation

An early motivation for accurate event detection and location of seismic activities evolved in the 1960's during the development of the Limited Nuclear Test Ban Treaty (LTBT); an agreement between the United States, Soviet Union, and Great Britain that prohibited nuclear testing in space, the atmosphere, and under water (FAS, 2004). According to the Federation of American Scientists (FAS, 2004) these countries were in favour of a comprehensive test ban, however, such a treaty was not perceived as plausible, as seismology was not considered an adequate means of monitoring underground nuclear explosions until the 1990's.

The need for accurate, dependable event detection and onset-time picking is of significant importance to the seismological community for a variety of additional applications. The necessity for automatic detection systems is increasing in our era of large volumes of digital data and real-time seismic acquisition. Further, manual reviewing of seismograms and phase picking is extremely time-consuming and subjective, as similarly qualified persons will pick onsets at different times.

Seismic monitoring of the subsurface is of interest on all scales from global to microscopic. The methods intended for global and regional seismic networks are applicable to surveillance of microseismic induced earthquakes at more local scales (Lee and Stewart, 1981). Seismic monitoring networks have been installed in regionally tectonic unstable locations such as Japan (Takanami, 1991) and California (BDSN, 2004), as well as in locally unstable structures such as Turtle Mt., Alberta (Stewart et al., 2004).

When considering a local event, the accuracy of event detection is of great interest. Any errors in the picking of onset times associated with a microseismic event may be amplified in the computations for locating the position of the event. The event location or hypocentre is the vital information that is desired by seismologists, geologists and geotechnical engineers.

Most recently, further motivation for accurate event detection and hypocenter location is based on reservoir characterization. Microseismic monitoring networks have been installed in a variety of arrays at oil field locations to examine changes in the reservoirs before, during and after production periods (Talebi et al., 1998; Kendall et al., 2005). Long-term examination of microseismicity in hydrocarbon reservoirs has the ability to reveal fracture geometry (Rutledge et al., 1998) as well as indicate the advancement of fluid fronts throughout production (Maxwell and Urbancic, 2001). Hydraulic fracturing in hydrocarbon reservoirs is another significant application of real time microseismic monitoring. The ability to retrieve immediate knowledge of the migration of fractures and thus fluids is vital to the process of opening flow paths and increasing productivity (Oye and Roth, 2003).

There is also a demand for accurate onset time selection in passive seismic tomography where a 3-dimensional velocity model of the subsurface can be recovered. This application of onset-time picking for passively recorded seismic events is becoming increasingly popular in our age of environmental sensitivity.

1.2 Literature Review

The algorithms commonly used for detection and selection of onset-times include analysis of energy (or amplitude), frequency, and polarization combined with prefiltering of data, as well as, autoregressive techniques and waveform correlation. Although there is a distinction in the literature between the drive for development of analysis techniques for broadband and short-period seismograms, the resultant knowledge can be applicable to both. There is also a separation of algorithms into trigger and onset-time pickers. Some techniques are proficient in both, while others are suitable when there is a separate trigger algorithm.

The various techniques for detecting and picking arrival times of seismic waves have been employed on single component and three-component (3-C) recordings. Energy analysis techniques have been used by many (Saari, 1991; Earle and Shearer, 1994; Tong and Kennett, 1996; Withers et al, 1998) to detect and pick the onset-time of phases. Most energy techniques employ the ratio of a short-term-average estimate of the energy content to the long-term-average energy level (STA/LTA). The various algorithms differ in the selection of the energy ratio between the components, the choice of coordinate systems, and the type of time window employed to calculate the energy ratios. These techniques tend to fail when used in environments with a low signal-to-noise ratio (SNR), when phase arrivals are characterized by a change in frequency, with little to no change in amplitude. They are especially ineffective when applied to emergent arrivals (Earle and Shearer, 1994).

Recently, Chen and Stewart (2005) formulated a multi-window technique similar to that used previously in energy analysis, except it uses the amplitude of the signal. This multi-window technique uses windows positioned before, after, and a delayed time after the arrival of a signal and is believed to reduce the number of false triggers in a microseismic monitoring system.

Frequency techniques using the S-transform (Pinnegar and Mansinha, 2003) have been proposed to aid in the process of onset-time picking of seismic waves. This method has yet to be scrutinized in detail for time picking but will be considered in Chapters 2 and 3. Instantaneous frequency techniques have been considered by Bai and Kennett (2000, 2001); they encountered a number of false detections when the SNR was low. Withers et al. (1998) have also compared trigger algorithms in the frequency domain, as well as in the time domain and waveform correlation. Vidale (1986) has employed polarization analysis to complex traces to identify Rayleigh and Love waves. Autoregressive techniques have been employed by a variety of researchers in broadband and short-period seismology to pick arrivals (Ozaki and Tong, 1975; Kitagawa and Akaike, 1978; Maeda, 1985; Takanami and Kitagawa, 1988; Takanami, 1991; Takanami and Kitagawa, 1991; Takanami and Kitagawa, 1993; Sleeman and Eck, 1999, Leonard and Kennett, 1999; Bai and Kennett, 2000 and 2001; Leonard, 2000). This technique requires an initial trigger algorithm and is computationally extensive, despite Takanami and Kitagawa’s (1993) applications of more efficient methods.

1.3 Overview of Onset-time Picking

Accurate and dependable picking of the first P-wave arrival and perhaps more importantly, the first S-wave arrival are of considerable significance in event location and recognition. The S-wave arrival time pick will provide stability to the computation of the event location. Figure 1-1 illustrates the true onset-time locations and my definition of onset-time picks for the P-and S-wave arrivals, with an arrival time interval of 50ms.

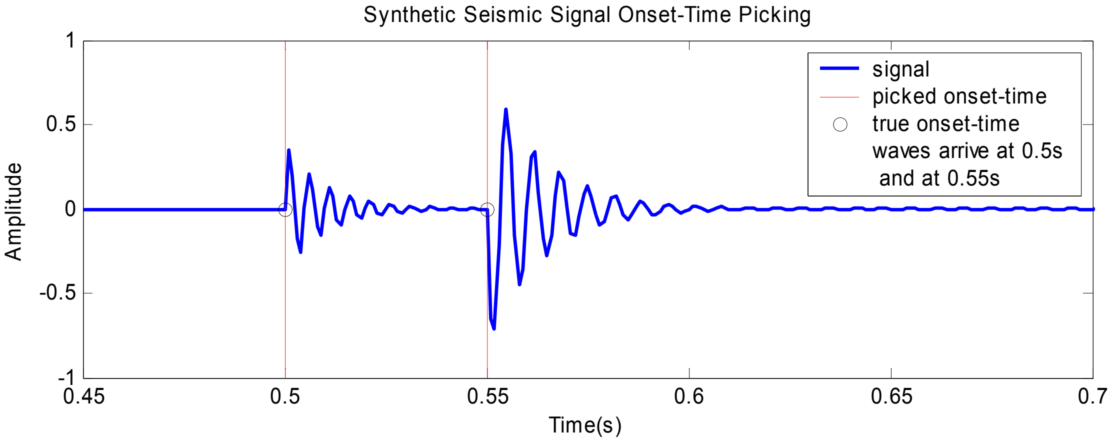

Figure 1-1 Synthetic seismogram showing onset-time picks for a P-and S-wave arrival.

As mentioned previously, manual P- and S-phase picking is extremely time-consuming and subjective, as similarly qualified persons will pick onsets at different times, some before and some after the true arrival time (Freeman, 1966a; 1966b; 1968). The ambiguity of phase picking results from seismic signals having an unknown shape and being contaminated with noise (Takanami, 1991). Thus, the selection of the arrival time for a specific wave is inherently biased. In first motion studies, it has been shown that the wrong sense of first motion is frequently picked when the signal-to-noise ratio (SNR) is below a critical value (Aki, 1976; Pearce and Barley, 1977).

Aki and Richards (1980) proposed an expression relating the error, Δt, of the first-break pick on a single channel seismogram to the frequency of the arrival, f_m and the SNR as follows:

$$\Delta t = \frac{1}{f_m \log_2\left[1+(SNR)^2\right]}. \qquad (1.2\text{-}1)$$

Although the SNR is difficult to delineate, Aki and Richards (1980) did empirically determine the RMS amplitude, S, to be equivalent to 1/20th of the maximum amplitude of the arrival, while N was found as the standard RMS amplitude of the noise. Consider a seismic event with an $f_m = 100$ Hz and SNR = 3, from equation (1.2-1), these resolve an error in the arrival time measurement of the first motion of $\Delta t = 3$ ms (Stewart et al., 1984); this value may be realistic for a single-component seismogram, but certainly quite large for 3-component recordings. Studies performed using vertical seismic profiling (VSP) suggested an arrival time error in the P-and S-wave of 2ms and 3ms, respectively (Stewart et al., 1984).

1.4 Introduction

Methods used to detect a seismic event, as well as to pick its onset time, are based upon identifying the different characteristics of the signal and surrounding noise in an assortment of domains, e.g. energy, frequency, waveform similarity, wave vector similarity, polarization, power and frequency spectrums. Unfortunately, there is no single method yet that provides reliable, accurate onset-time picks for all seismic events. Any particular method will be unsuccessful when a certain part of the noise is not sufficiently distinct from the signal, or when the signal-to-noise ratio (SNR) is minimal. The most common approach to detecting a seismic event is in the energy domain; however, current methods fall short when the noise level is high and/or when later phases are buried in the coda of an earlier event. Other techniques include band-pass filtering, which fails when the signal and noise have similar frequency content. These short falls may be overcome by introducing updated methods in hopes of generating dependable time picks.

In this research, I follow the concept ‘the less filtering, the better the algorithm’ (Douglas, 1997). Thus, I will not be analyzing any methods that require frequency filtering. Chapter two analyses updated event detection techniques in the energy, amplitude, and frequency domains; as well as using locally stationary autoregressive models in conjunction with the Akaike Information Criteria (AIC) and finally, the application of the S-transform to the energy of the signal. In Chapters three and four these techniques are applied to two different case studies; a locally unstable landslide region at Turtle Mt., Alberta and an oilfield-monitoring reservoir at Cold Lake, Alberta. Chapter five presents a summary of this work and provides further recommendations.

CHAPTER TWO: Analysis of Event Detection and Picking Techniques

2.1 Introduction

The detection of microseismic events is based on separating the seismic events from ambient noise. Since seismic events and background noise usually differ in character and frequency content, it is often possible to distinguish them on a seismogram. Microseismic events are generally characterized by impulsive onsets, high frequency, an exponential envelope, and decreasing signal frequency with time, while background signals are distinguished by their low amplitude, low-frequency signature (Lee and Stewart, 1981); the algorithms I have selected to analyze depend on such assumptions.

A number of techniques are currently employed for identification and picking of seismic waves using single- or three-component recordings (one vertical; two horizontal components of motion). In this study, I concentrate on three-component recordings. I separate the procedures into algorithms that are efficient in triggering and picking onset times, and algorithms that are only useful for picking onset times. I define ‘trigger and onset time picking’ as the methods that are used to detect an event and are also concerned with the accuracy or identification of the event. While the ‘onset-time picking’ algorithms require a separate program to initially detect the event. In this work ‘onset-time picking’ algorithms are thought to be more robust and have a greater ability to characterize the events.

Here, I employ an energy-domain technique that uses the ratio of the short-term average to the long-term average (STA/LTA); an amplitude-domain technique that uses ratios of averages that are taken before, after and a delayed time after a signal arrives (BTA, ATA, DTA); an auto-regressive technique in conjunction with the Akaike

Information Criterion (AR-AIC) that is also performed in the amplitude-domain; and lastly, an S-transform technique using the energy of the signal (based on software from Calgary Scientific Ltd.). Using synthetic data, I analyze and illustrate these methods for detecting and picking onset arrival times for P- and S-waves in three-component recordings.

Section 2.2 describes the synthetic microseismic data that will be evaluated in section 2.3 using the energy, and multi-window techniques and in section 2.4 using the AR-AIC and S-transform techniques. Each technique, except the S-transform, is assessed by varying the dominant frequencies and relative amplitudes of the P-and S-waves, and finally, by changing the type of background noises and their signal-to-noise ratios (SNR). Specific techniques are selected to evaluate their capabilities for resolving the S-wave arrival from the P-wave coda. Lastly, section 2.5 presents a discussion and conclusion of this chapter.

2.2 Overview of Synthetic data

To determine the effectiveness of these automatic event detection and picking methods, I will be contrasting their onset-time pick values for the P-and S-waves with known event times by using synthetic data. The synthetic microseismic event consists of two exponentially decaying sine waves, one for the P-wave, $f(\tau)$, with time, τ, and the other for the S-wave, $g(\tau)$, see equation (2.2-1). For some methods, the dominant frequencies of these waves will be altered to determine their effectiveness'. I have chosen a dominant frequency range of 20-400 Hz and selected a mid-range value, as indicated below, to evaluate examples. Dominant frequency values were selected accordingly with previous studies performed by others on Turtle Mt., Alberta (Wiechert and Horner, 1981;

Kanasewich, 1986; Bingham, 1996; Stewart et al., 2004), and in the North Sea (Oye and Roth, 2003). Stewart et al. (2004) assessed microseismic events recorded at the Blairmore Quarry, Alberta that had dominant energy in the 100-200Hz band. Multiple studies performed in the same area find a range of dominant frequencies from 10-100Hz (Wiechert and Horner, 1981; Kanasewich, 1986; Bingham, 1996). Oye and Roth (2003) evaluated microseismic events recorded at the Ekofisk oil field in the North Sea with signal frequencies of 150-400Hz.

I use a P-wave with a dominant frequency of 200 Hz, and an S-wave with a dominant frequency of 150 Hz, both with a sample rate of 1 kHz.

$$\begin{aligned} &f(\tau) = A_p \sin(400\pi\tau)\exp(-100\tau), \\ &g(\tau) = A_s \sin(300\pi\tau)\exp(-75\tau), \qquad (2.2\text{-}1) \\ &A_p = 0.8A_s, \end{aligned}$$

with A_p as the amplitude of the P-wave, set to be 80% of the amplitude of the S-wave, A_s at time τ. For some methods, the amplitude relationship will also be adjusted to test the algorithms success. The synthetic microseismic signal, I have described is illustrated in Figure 2-1, where the S-wave arrives at a time, τ =0.070 seconds. The time interval between the arrival times of the P and S-waves will be changed to examine the methods sensitivity. Two types of background noise will be added to this signal. The first form of background noise will be generated as random noise that is normally distributed with a mean of zero and with a specified amplitude (signal-to-noise ratio). The other form uses background noise that will be taken directly from real data. For example, a random noise signal that is normally distributed with a specified signal-to-noise ratio of 10 is added to our waveform, see Figure 2-3.

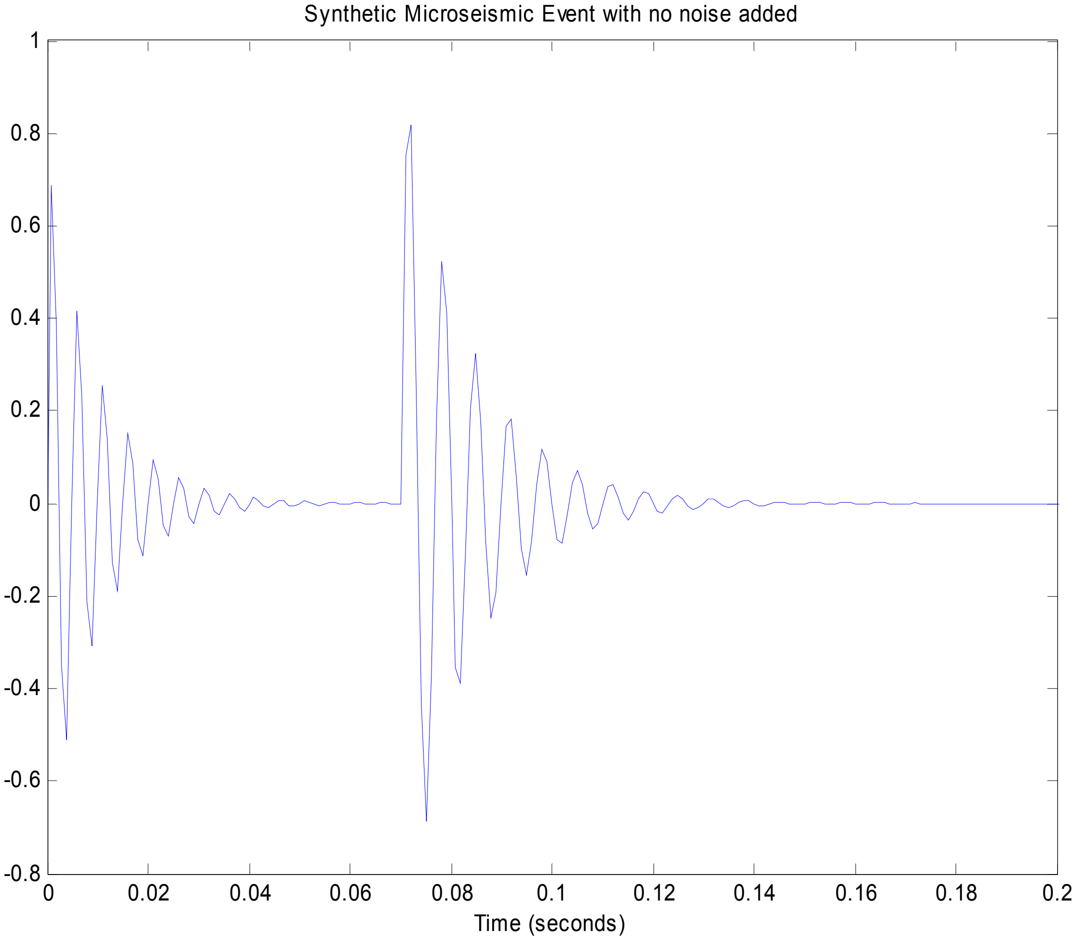

Figure 2-1 Synthetic microseismic event signal prior to addition of noise. Note that the P-wave arrives at a time of 0 seconds, while the S-wave arrives at a time of 0.070 seconds.

To generate three-component synthetic seismic recordings, I follow Aki and Richards (2002) geometric definitions for P- and S-unit vectors in Cartesian coordinate directions ($\hat{\mathbf{x}}, \hat{\mathbf{y}}, \hat{\mathbf{z}}$), where φ and θ represent the wave propagation's azimuth and inclination values, respectively and $\hat{\mathbf{x}} = \text{North}$, $\hat{\mathbf{y}} = \text{East}$, and $\hat{\mathbf{z}} = \text{vertically downward}$, as shown in Figure 2-2. In terms of these unit vectors,

$$P - \text{unit vector} = \sin\theta\cos\varphi\,\hat{\mathbf{x}} + \sin\theta\sin\varphi\,\hat{\mathbf{y}} + \cos\theta\,\hat{\mathbf{z}}, \tag{2.2-2}$$

$$S - \text{unit vector} = (\cos\theta\cos\varphi - \sin\varphi)\hat{\mathbf{x}} + (\cos\theta\sin\varphi + \cos\varphi)\,\hat{\mathbf{y}} - \sin\theta\,\hat{\mathbf{z}}, \tag{2.2-3}$$

The case where the microseismic signal is incoming at an angle to the z-axis of 30°, and the same angle from the x-axis is shown in Figure 2-2.

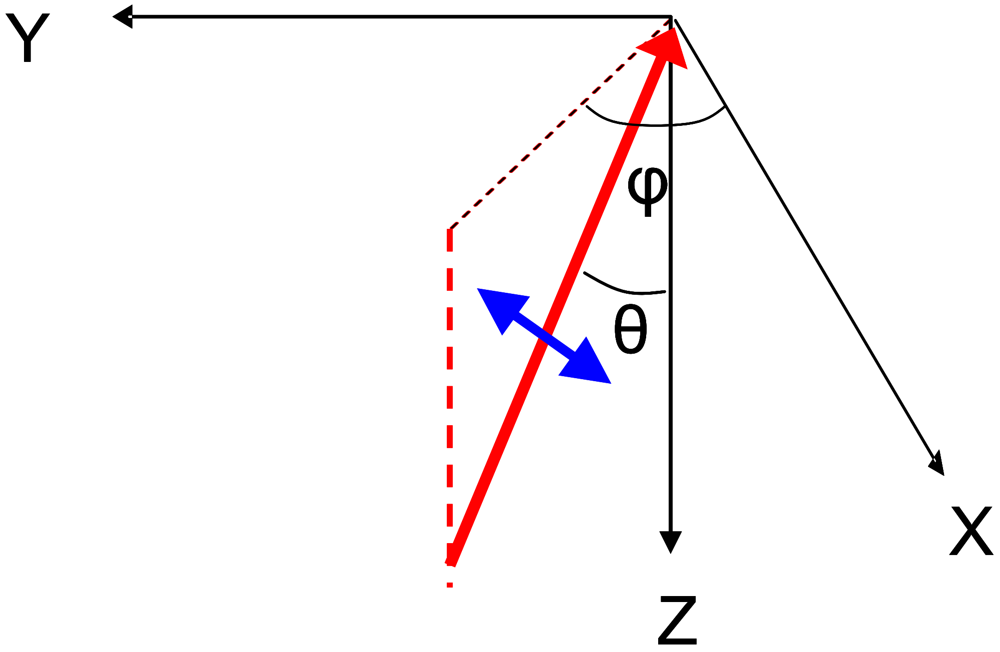

Figure 2-2: Propagation and wave motion of the synthetic microseismic event. Note that the solid red arrow is in the direction of propagation of all waves and the direction of motion for the P-wave. The blue arrow is the direction of motion for the S-wave. The angle φ represents the azimuth, and θ the inclination.

Figure 2-3 displays the recordings from the three-component geophone for this microseismic event. The P-wave is positioned at 0.600 seconds, and the S-wave positioned at 0.670 seconds.

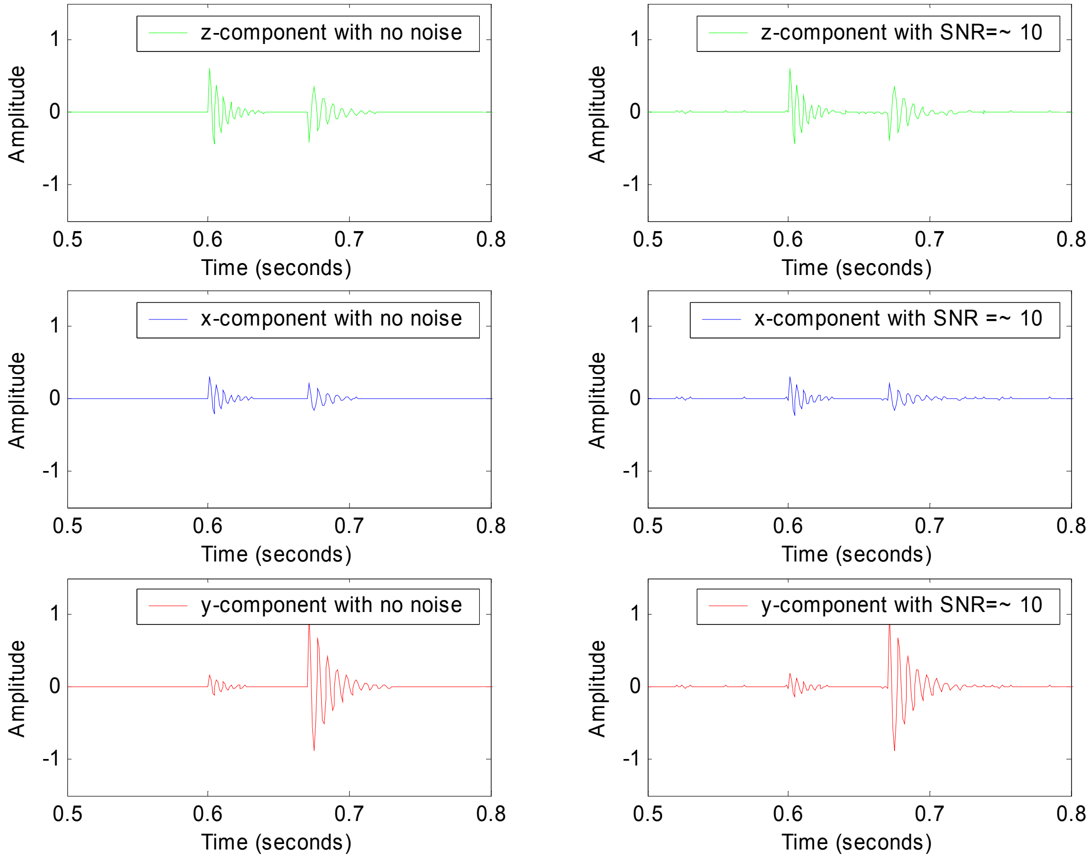

Figure 2-3 Synthetic seismograms for the three-component geophones of the microseismic event prior to, and with the addition of background noise with a specified SNR of approximately 10, propagating in the direction with an azimuth and an inclination of 30° as illustrated in Figure 2-2. The P-wave arrival time is at 0.600 seconds, while the S-wave arrives 0.070 seconds later.

The SNR is evaluated according to equation (2.3-4);

$$SNR = \left(\frac{\sqrt{Amp_{event} \times \overline{Amp_{event}}}}{\sqrt{Amp_{noise} \times \overline{Amp_{noise}}}} \right), \tag{2.3-4}$$

where Amp_{event} represents the maximum amplitude of the smallest event recorded on any of the three components according to the ray orientation; Amp_{noise} represents the maximum amplitude of the random noise vector; and lastly, $\overline{Amp_{event}}$ and $\overline{Amp_{noise}}$ represent their complex conjugates, respectively.

The onset time that I am choosing to pick is the first break, not the maximum amplitude, as illustrated previously in section 1.2.

2.3 Microseismic Event Detection Trigger and Onset Time Picking Algorithms

Energy Techniques

2.3.1 Energy Technique Theory

It is possible to take advantage of the characteristics of microseismic events by using the notion of short-term and long-term averages of the incoming signal's energy (STA and LTA, respectively). I follow the expressions of Bai and Kennett (2000) in an un-rotated data system.

$$\begin{aligned} &\text{The total energy} && E_e = Z^2 + N^2 + E^2. \\ &\text{The vertical energy} && Z_e = Z^2. && (2.3\text{-}5) \\ &\text{The energy in the horizontal plane} && H_e = N^2 + E^2, \end{aligned}$$

where Z, N, and E are the amplitude of the three un-rotated components that were previously noted in the z-,x- and y-directions. The identification format is based on the use of the STA/LTA. For example, the computation of the STA, $\alpha(\tau)$ and LTA, $\beta(\tau)$, at time τ, for the total energy of the signal, E_e are as follows:

$$\alpha(\tau) = \frac{\sqrt{\sum_{-n_1}^{0} E_e(t_k)}}{n_1}, \qquad (2.3\text{-}6)$$

$$\beta(\tau) = \frac{\sqrt{\sum_{-n_2}^{0} E_e(t_k)}}{n_2}.$$

Here n_1 is the number of data points (i.e., the length of the time window for the short-term average divided by the sample rate of the data) and n_2 is the number of data points (i.e., the length of the time window for the long-term 'average' divided by the sample rate of the data). These calculations are L2 norms evaluated over the specified windows.

The long-term average (LTA) characterizes the slow trend of signal energy, while the short-term average (STA) is more responsive to sudden increases in energy (Oye and Roth, 2003). The ratio, STA/LTA is used as a measure of the signal-to-noise ratio (SNR). When the ratio, STA/LTA exceeds a pre-defined constant threshold a detection time is assigned to that specific geophone. I have also added an additional threshold to the value of the STA for the situation where the STA/LTA is triggered. This supplementary threshold should help to combat false triggers by low-amplitude, harmonic noises.

Although the main purpose of the energy analysis technique is to pose as an event trigger algorithm, I can obtain onset times from the trigger information with some additional computations. To more accurately determine the arrival time of the waves, I propose using the time associated with the maximum gradient of the STA/LTA ratio within a window centred about the event's trigger time. This will remove the influence of the STA/LTA threshold value. In a seismic monitoring system, once a number of geophones are triggered, an event is considered detected and the system computes the time at which this event has arrived and then proceeds to compute the location of the event or the hypocenter.

The lengths of the STA and LTA window are dependent upon the distance between the receivers and the average distance to the seismically active region (Oye and

Roth, 2003). The STA is usually longer than a few periods of the typically expected signal, and the LTA is longer than a few periods of typically irregular seismic noise fluctuations.

For a relatively large signal-to-noise ratio, which can be the case for microseismic data, this procedure used to detect microseismic events also evaluates the first P-wave arrival, and possibly the S-wave arrival times.

Since the STA/LTA threshold is defined to be greater than the pre-existing noise levels, when this threshold is surpassed the triggered time must be delayed in comparison to the true onset time in accordance with the formation of the first arrival of a seismic event. An onset-time correction is used to counteract this. For my assumptions of an impulsive seismic event arrival, I can perform the correction using a few simplistic calculations. As discussed previously, I am considering the point at which the maximum gradient of the STA/LTA, t_{gmax} occurs within a window centred on the triggered time, t_r, see Figure 2-4 for a schematic diagram showing the steps performed. Next, from the amplitude and the gradient of the STA/LTA evaluated at the maximum gradient time, t_{gmax}, I can perform a linear correction in time; effectively, taking the t_{gmax} time backwards by an amount of correction, Δt_c, to a corrected onset time, t_{oc}, that is closer to the real onset time, t_0. Figure 2-5 contains a schematic diagram illustrating the components used to perform the onset-time correction.

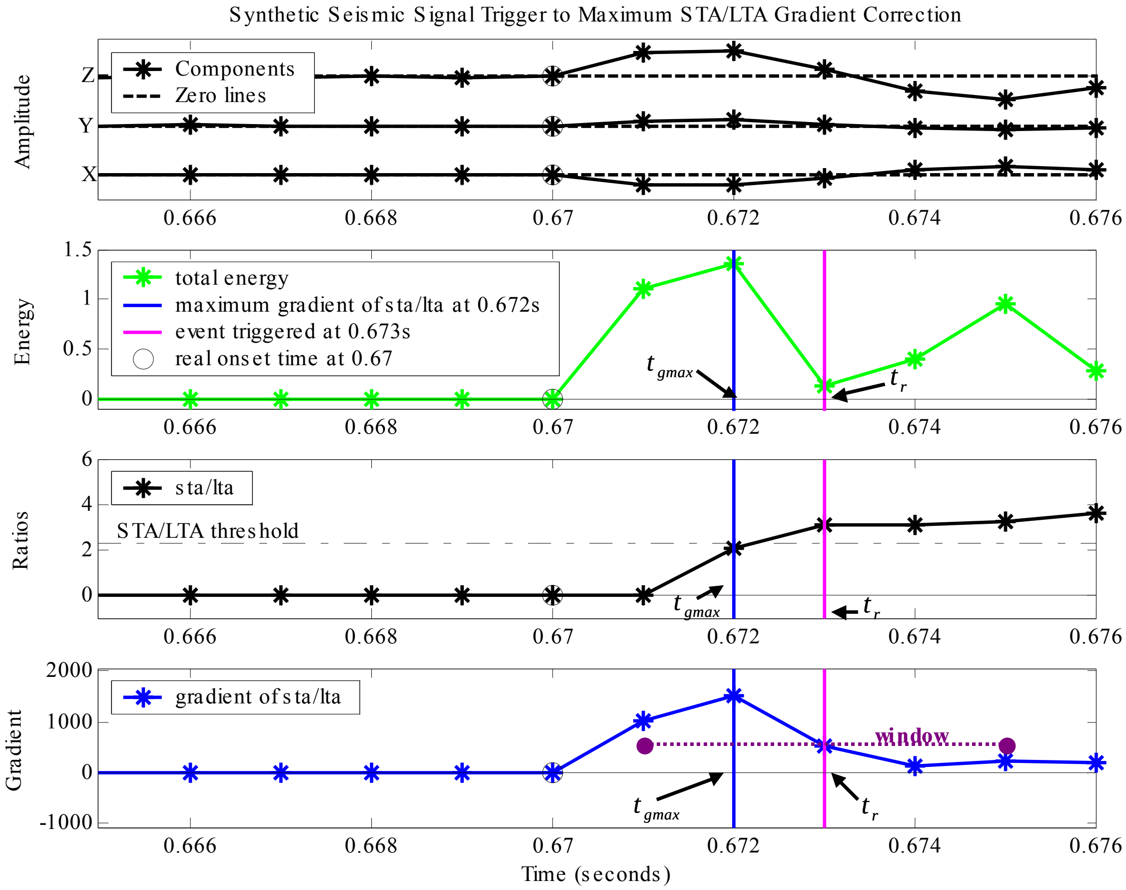

Figure 2-4 Schematic diagram showing the items used in the correction of the trigger time (t_r) to the maximum gradient of STA/LTA time (t_{gmax}) of an event. The purple line indicates the window used to find the maximum gradient of the STA/LTA; Open circle is the real onset time (t_0).

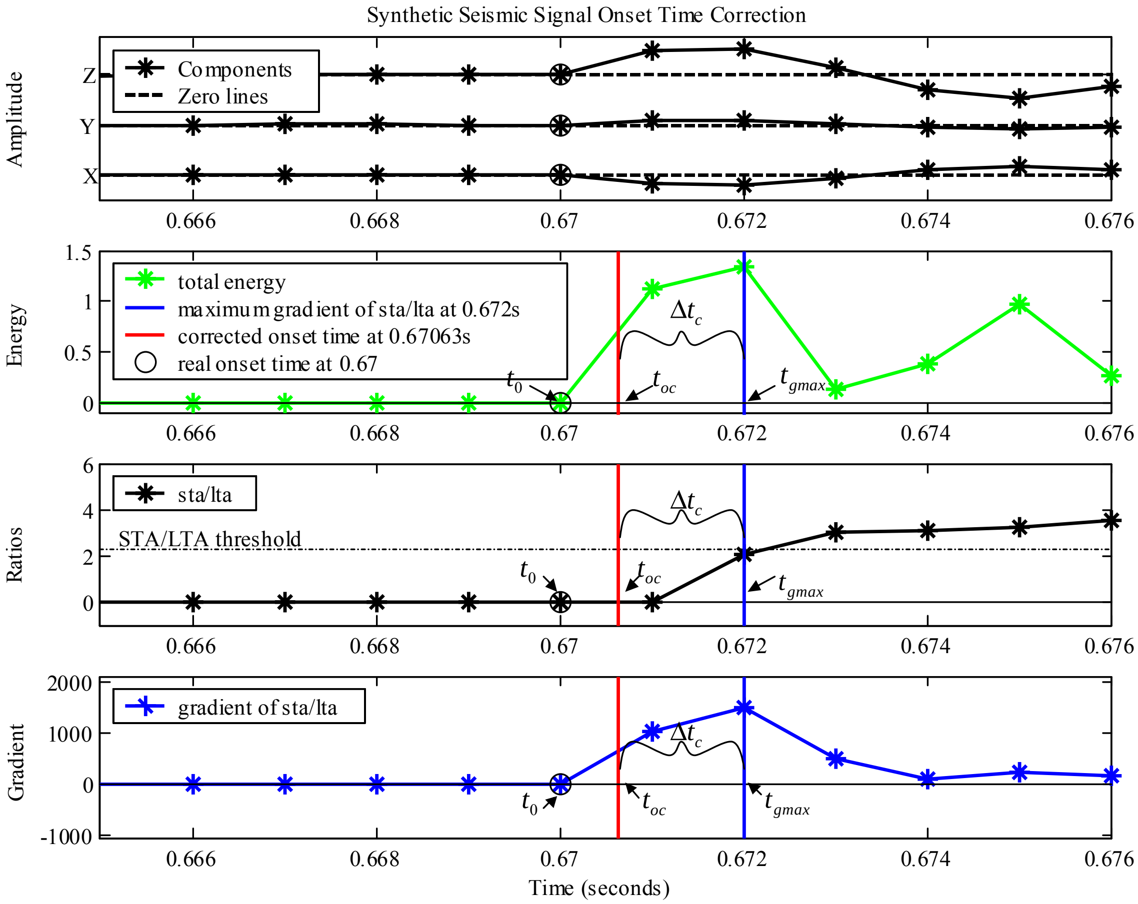

Figure 2-5 Schematic diagram showing the items used in the onset time correction performed on the maximum gradient of STA/LTA time (t_{gmax}) for corrected onset time (t_{oc}) of an event. The calculated amount of onset time correction is (Δt_c); Open circle is the real onset time (t_0).

To discern the usefulness of taking this additional step to correct the onset-time picked according to the STA/LTA technique described above, I first analyze the energy technique with only the maximum gradient computation applied to the synthetic data computation (see section 2.3.2); second, I compare this to the energy technique while applying the onset-time correction (see section 2.3.3).

2.3.2 Analysis of Energy Technique using Synthetic data without an Onset-time Correction

Using the synthetic microseismic events as depicted in the previous sections I aim to determine the competence of this energy procedure for detecting and picking events, and how sensitive it is under various conditions. The standard synthetic model that I will be altering will be the same one that is described in section 2.2 that has a P-wave with a dominant frequency of 200 Hz and an S-wave with a dominant frequency of 150 Hz and amplitude that is 25 % greater than the P-wave. Random background noise is also embedded with a SNR of 10.

Frequency dependency of picking

The dominant frequencies of the waves have been varied to examine their effects on the event picking. The dominant frequency of the P-wave was kept greater than that of the S-wave. I have attempted frequencies between 20 Hz, and 400 Hz, with various relative ratios. To ensure that picking errors are not based on the added random background noise, the procedure was performed one hundred times, and then the root square mean (RMS) of the errors was resolved. Wave propagation was evaluated for an azimuth of (0-90)°, since wave propagation is symmetric. That is for an azimuth of (30-60)°, the same results are seen for (120-150)°, (210-240)°, and (300-330)°, however with the x-and y-component records switched.

The calculations preformed in detecting an event and determining its onset time for a P-wave frequency of 200 Hz, and an S-wave frequency of 150 Hz are illustrated for a wave propagating with an azimuth and an inclination of 30° in Figure 2-6. The overall results for a ray oriented with an azimuth and an inclination ranging from (0 to 90)° and for a P-and S-wave dominant frequency ranging from 20 Hz to 400 Hz are illustrated in

Figure 2-7. Figure 2-7 displays a graph of the RMS errors and a histogram demonstrating the percentage of events not detected or having a RMS error greater than 10 ms. The STA threshold values were 0.055, 0.04, 0.02, and 0.01 when the dominant frequencies for the P-wave were set to 40Hz, 100Hz, 200Hz, and 400Hz, respectively.

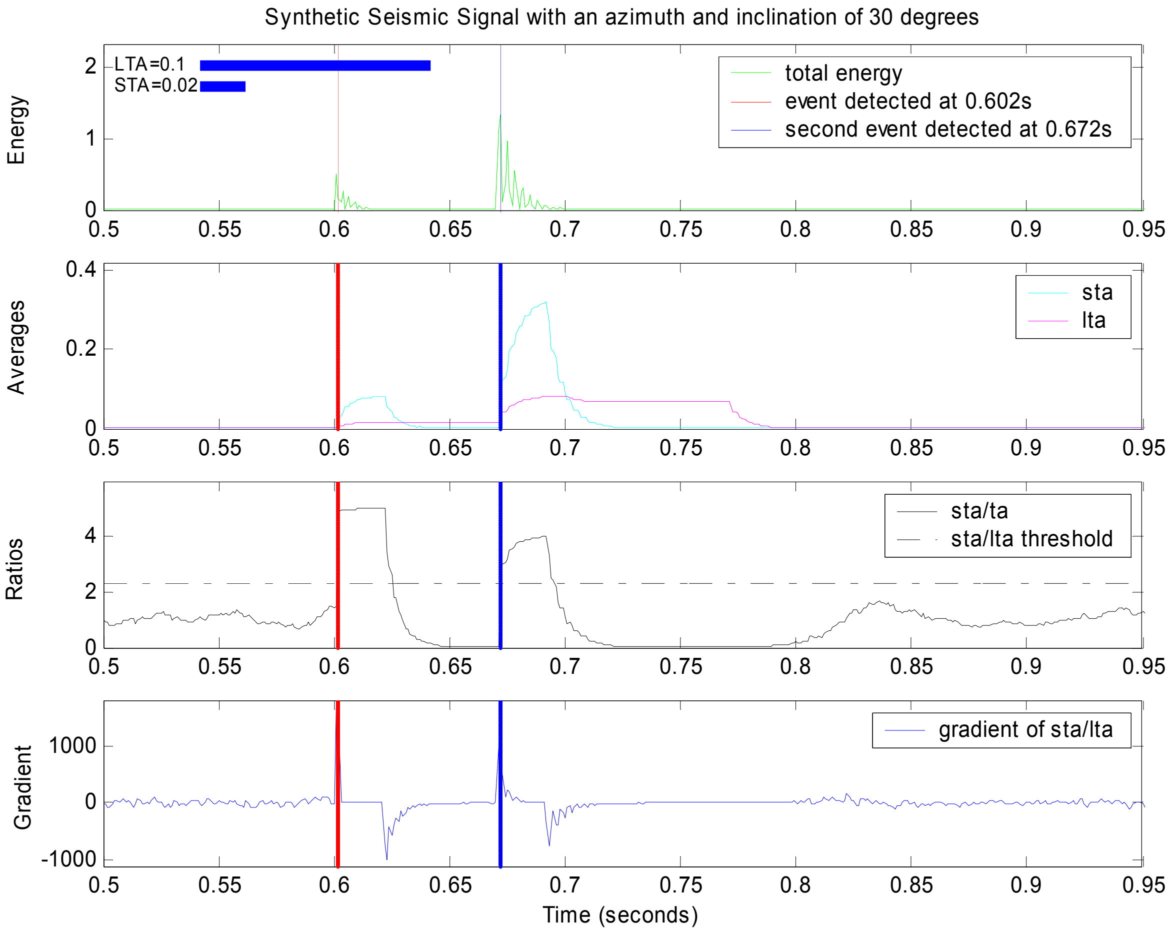

Figure 2-6 top to bottom: Total energy for synthetic event with an azimuth and inclination of 30° and a P-and S-wave dominant frequency of 200 Hz, and 150 Hz respectively; STA and LTA; STA/LTA; Gradient of the STA/LTA. Red line indicates the first P-wave arrival time picked with the STA threshold of 0.02 and STA/LTA threshold of 2.3. Blue line represents the second event arrival time, corresponding here to the S-wave.

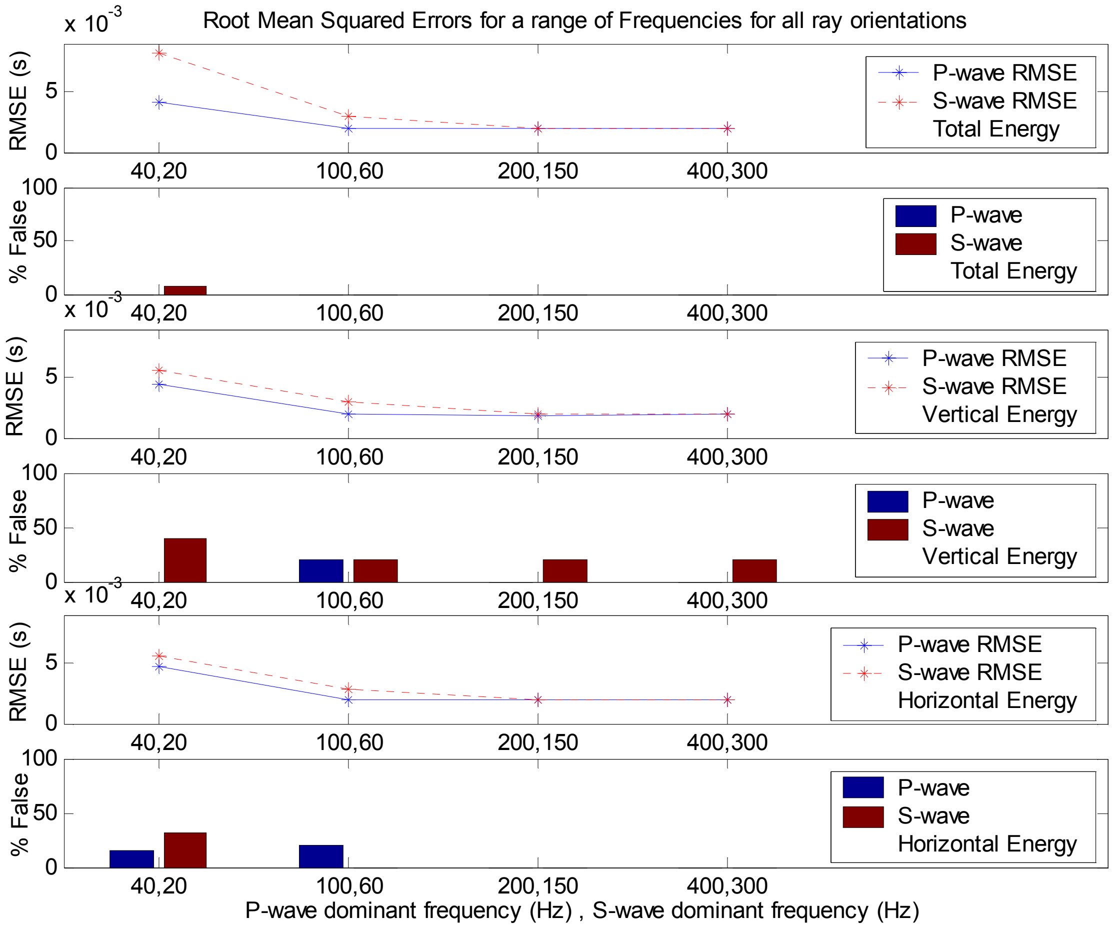

Figure 2-7 RMS errors and percentage of false triggered or undetected events for wave frequencies ranging from 20Hz to 400Hz.

Figure 2-7 demonstrates that the higher the frequency contents, the less error in the onset-times picked by the algorithm for all ray orientations. The mean onset-time pick for the P- and S-waves detected at dominant frequencies of 200 Hz and 150 Hz, respectively, and at higher frequencies, was found to be approximately 2 ms, or 2 sample points. From the three energy functions computed it can be seen that the RMS errors for the vertical and horizontal energy have a very similar response to change in frequency for both the P-and S-wave. As anticipated the percentage of false triggers is largest on the vertical energy calculations for the S-wave. Overall the total energy function appears to be the most robust, having only a small percentage of false triggers; yet still having a larger RMS error for the S-wave on the lowest frequencies.

Amplitude dependency of picking

To inspect the influence of varying the relative amplitudes of the waves, I have attempted the following five amplitude relations:

1. $A_P = A_S = 1$
2. $A_P > A_S$
3. $A_P < A_S$
4. $A_P >> A_S$
5. $A_P << A_S$.

Again, to make certain that the picking errors are not based on the random background noise added, the algorithm was performed one hundred times, and the RMS errors were resolved. The calculations preformed in detecting an event and determining its onset time for a P-wave amplitude 25% greater than the S-wave's are illustrated for a wave propagating with an azimuth and an inclination of 30° in Figure 2-8. The overall results for a ray oriented with an azimuth and an inclination ranging from (0-90)° and a P-to S-wave relative amplitude ratio ranging from 0.5 to 2 are illustrated in Figure 2-9.

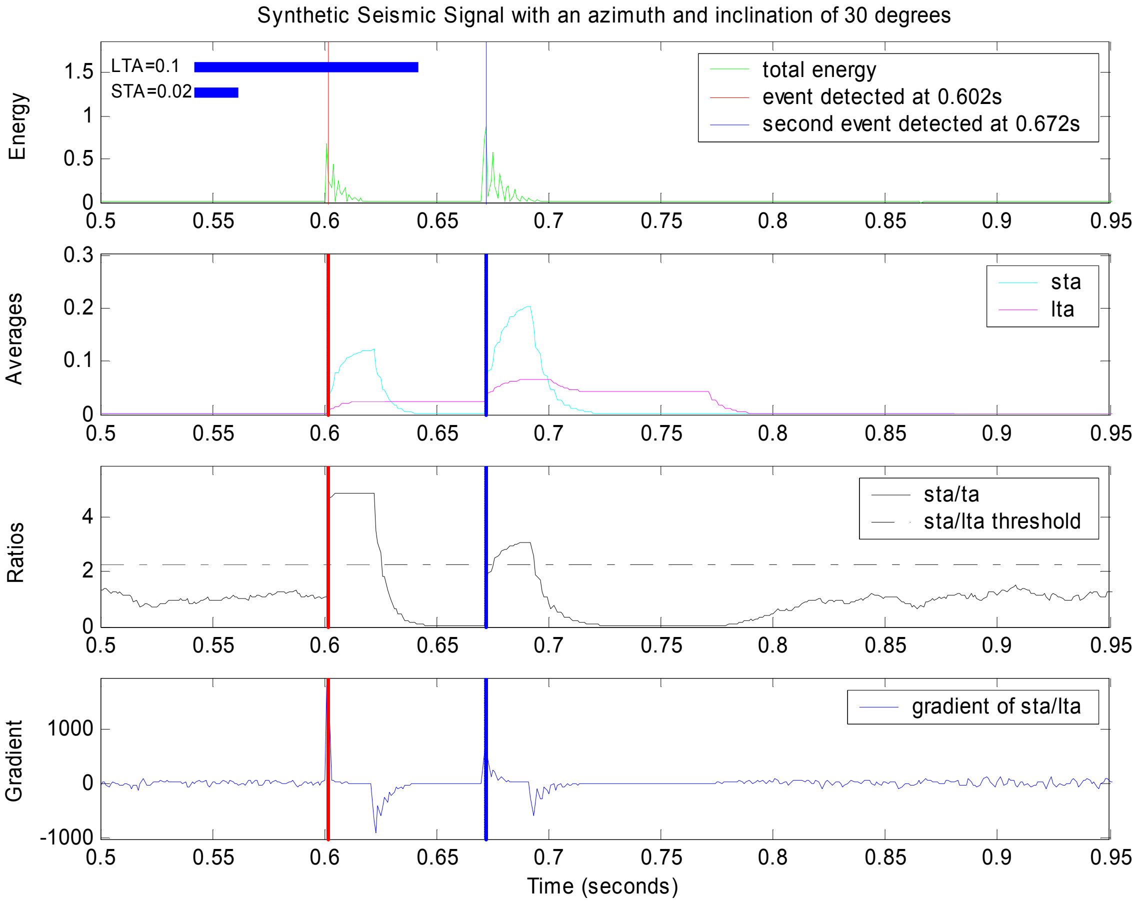

Figure 2-8 top to bottom: Total energy for synthetic event with an azimuth and inclination of 30°, and the P-wave amplitude 25% greater than the S-wave amplitude; STA and LTA; STA/LTA; Gradient of the STA/LTA. Red line indicates the first P-wave arrival time with the STA threshold of 0.02. Blue line represents the second event arrival time, corresponding here to the S-wave.

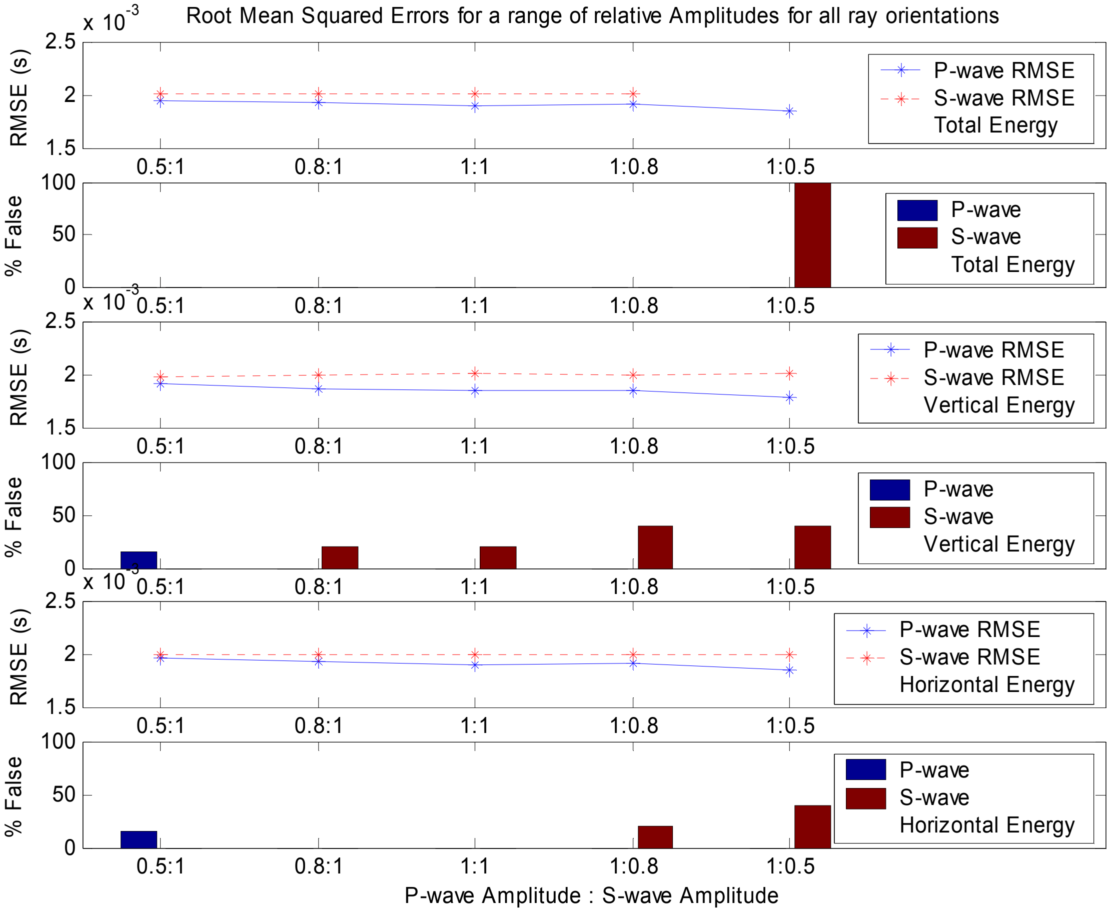

Figure 2-9 RMS errors and percentage of false triggered or undetected events for relative wave amplitudes ratios ranging from 0.5 to 2.

By varying the relative amplitudes of the P-and S-waves it is seen that the RMS error of the S-wave onset-time is not influenced and remains consistently around 2ms. The P-wave RMS error becomes slightly larger as its amplitude decreases with respect to that of the S-wave's. The P-wave's RMS error still remains below the S-wave's RMS error. As expected for the relative amplitudes that are two times as large as the P-or S-waves amplitude's there appears to be more events that go undetected for the smaller amplitude, especially when the S-wave is lowest. In terms of the different energy functions used the RMS error for the waves remains consistent as the relative amplitudes are adjusted, with the exception of the S-wave not being detected at all by the total energy function when its amplitude is half that of the P-wave's.

Background Noise Influence on Picking

To inspect the impact of background noise on the onset-time picks and the detection of the P- and S-wave arrivals, I have attempted a variety of signal-to-noise ratios (SNR) from 1.5 to 10, as well as taking background noise off of a recording from geophones situated at Turtle Mt., AB. The standard background noise I have used to alter the SNR is a series of random numbers that are normally distributed, with zero mean. The calculations preformed in detecting an event and determining its onset time for a background noise with a SNR of 3 are illustrated for a wave propagating with an azimuth and an inclination of 30° in Figure 2-10. The overall results for a ray oriented with an azimuth and an inclination ranging from (0-90)° and a random background noise with a SNR ranging from 10 to 1.5 are illustrated in Figure 2-11. I did attempt the same variation of SNR with a random noise that was uniformly distributed and very similar results were found. The other type of background noise investigated was taken directly from an event at Turtle Mt., AB, on November 13, 2004. The SNR was amplified from around 100 to be a variety of SNR's. The calculations preformed in detecting an event and determining its onset time for a background noise from Turtle Mt., AB, with a SNR of 3 are illustrated for a wave propagating with an azimuth and an inclination of 30° in Figure 2-12. The overall results for a ray oriented with an azimuth and an inclination ranging from (0-90)° and background noise taken from Turtle Mt., AB, with a SNR ranging from 10 to 1.5 are illustrated in Figure 2-13.

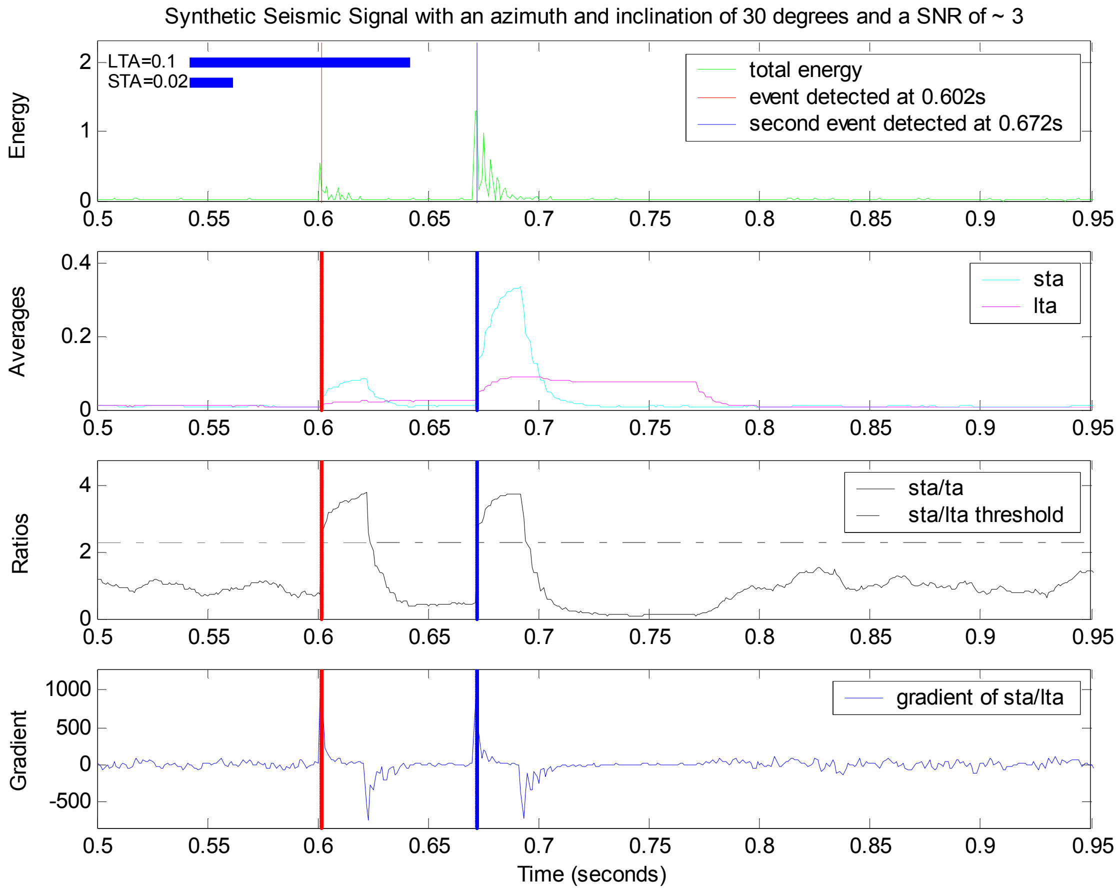

Figure 2-10 top to bottom: Total energy for synthetic event with an azimuth and an inclination of 30° and a SNR around 3; STA and LTA; STA/LTA; Gradient of STA/LTA. Red line indicates the maximum gradient corrected time for the first P-wave arrival time. The blue line represents the second event arrival time, corresponding here to the S-wave.

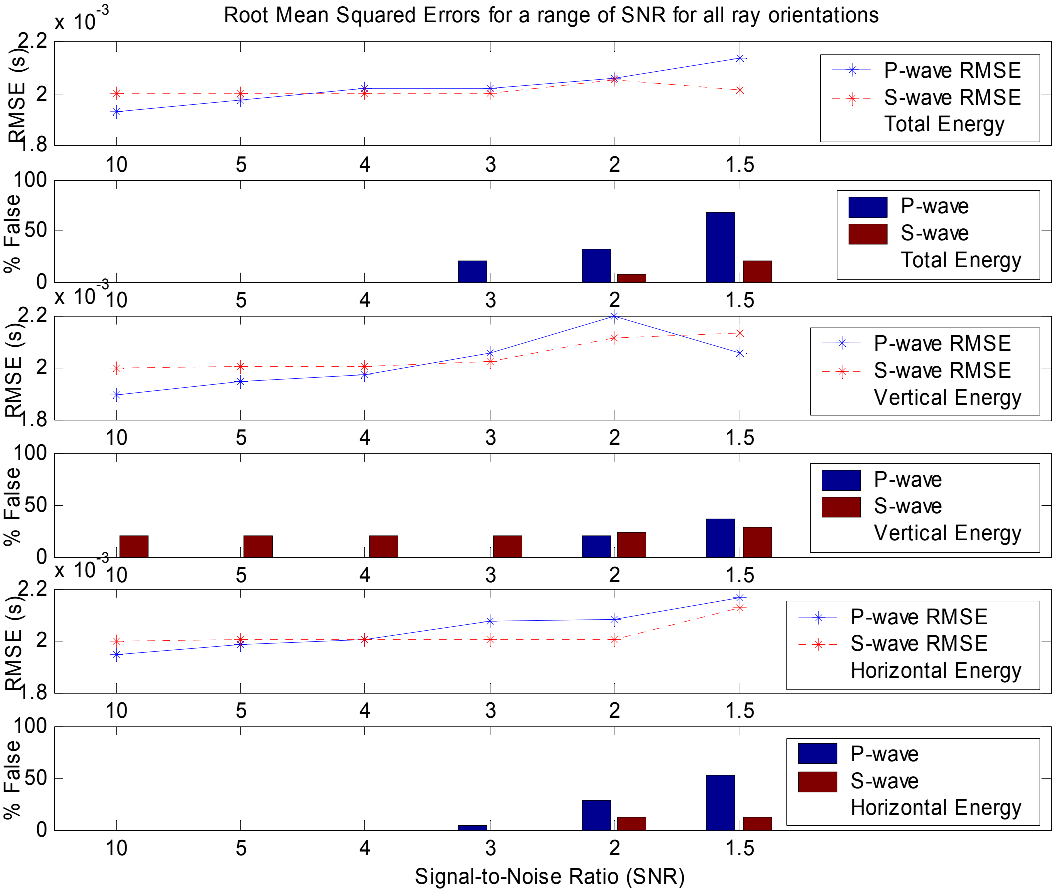

Figure 2-11 RMS errors and percentage of false triggered or undetected events for random background noise with a SNR ranging from 10 to 1.5.

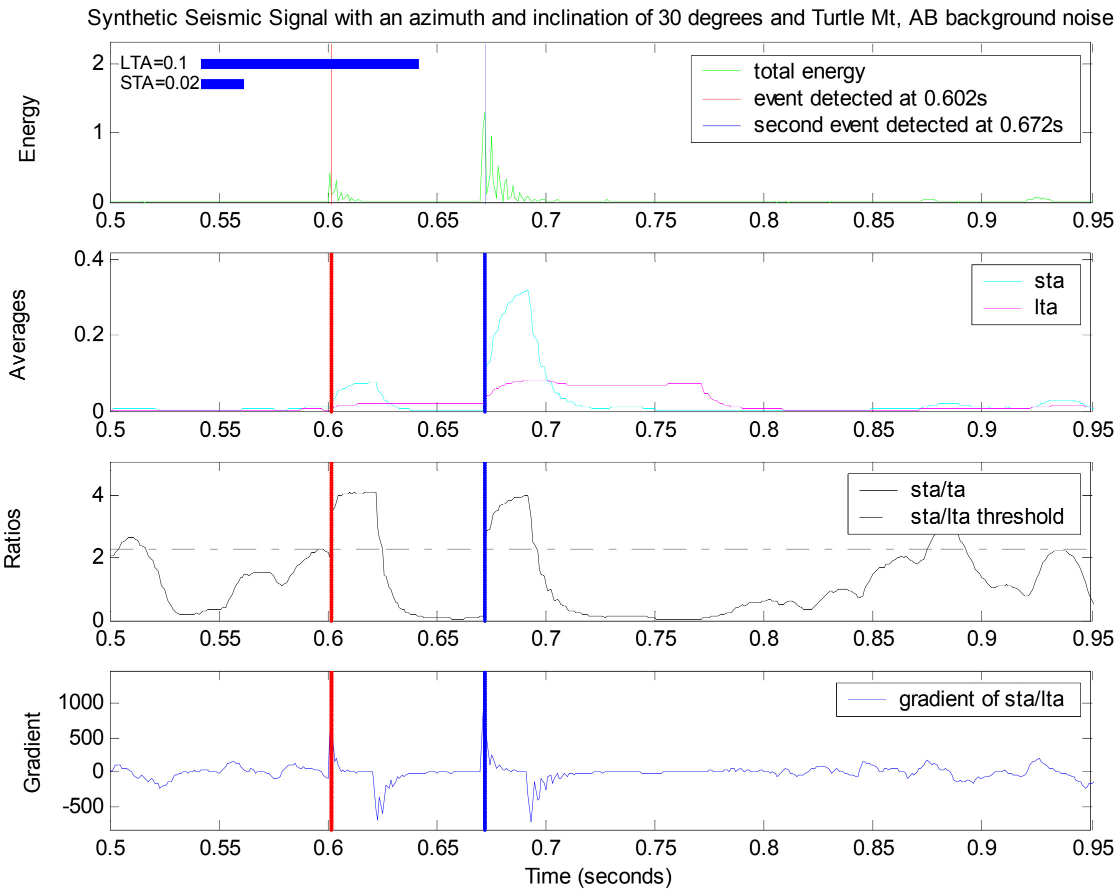

Figure 2-12 top to bottom: Total energy for synthetic event with an azimuth and an inclination of 30° and a SNR of 3 using noise taken directly from a microseismic event recorded at Turtle Mt., AB, on November 13, 2004; STA and LTA; STA/LTA; Gradient of STA/LTA. Red line indicates the maximum gradient corrected time for the first P-wave arrival time. The blue line represents the second event arrival time, corresponding here to the S-wave.

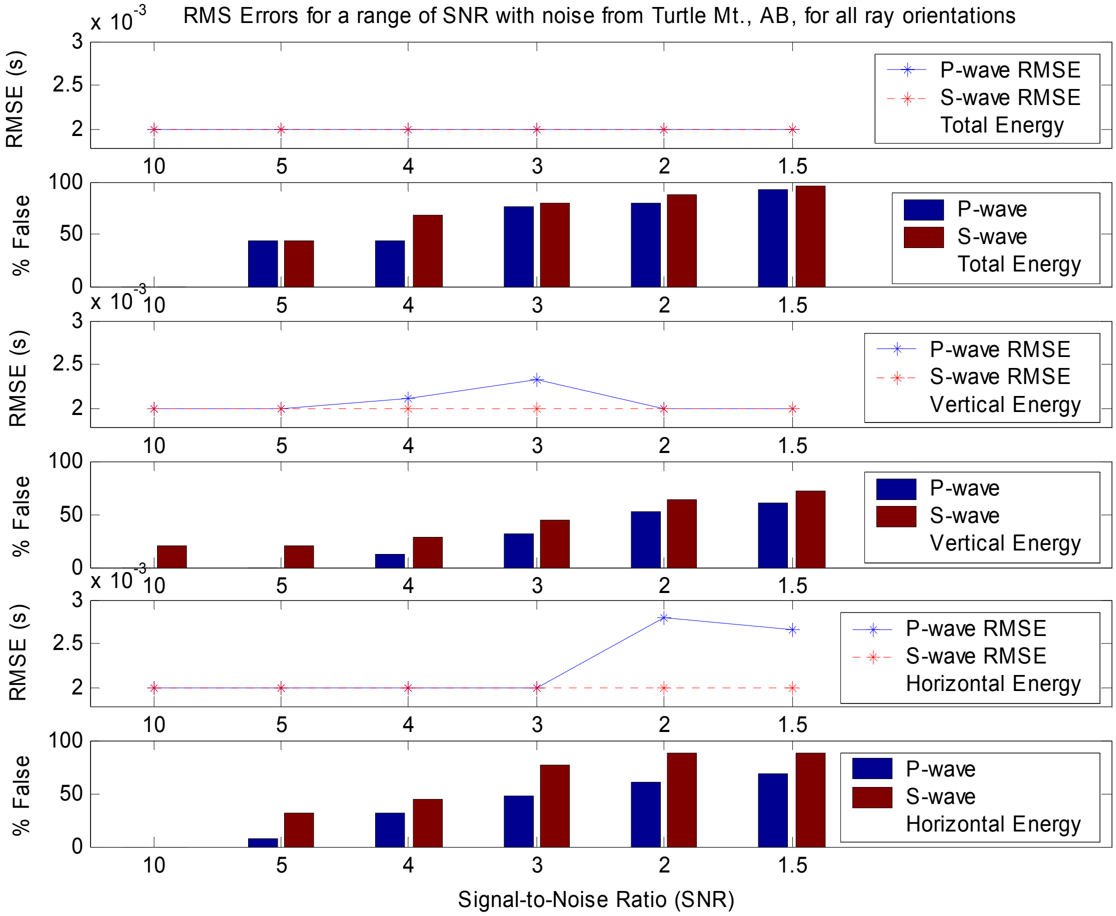

Figure 2-13 RMS errors and percentage of false triggered or undetected events for background noise taken from Turtle Mt., AB, with a SNR ranging from 10 to 1.5.

Varying the SNR using random background noise does appear to have a minor influence on the onset-time errors, although still only fluctuating between 1.9ms to 2.2ms. As the SNR was decreased, the errors increased as anticipated, with the exception of the P-wave on the vertical energy calculations at a SNR of 1.5, where a slight decrease was observed, see Figure 2-11. As the SNR was decreased the RMS errors of the P-wave was found to be more sensitive than the S-wave's. The S-wave errors do not vary from 2ms until the SNR goes below 3. For the horizontal energy calculations the S-wave errors do not change until the SNR is less than 2. As the SNR was reduced the volume of events that were considered not detected or detected with an error greater than 10ms did rise. The P-wave results appeared to be most sensitive. This may be a result of the amplitude of the P-wave being slightly less than that of the S-wave.

When the background noise was taken directly from a microseismic event recorded at Turtle Mt., AB, the P-wave picking errors were effected as the SNR was decreased, especially on the horizontal energy function as shown in Figure 2-13. The S-wave errors remained constant at 2ms for all SNR's on all energy functions, however, the number of events that were considered undetected increased dramatically in comparison to the random noise background, see Figure 2-11 and Figure 2-13. The P-wave picking error remained constant at 2ms for all SNR's on the total energy function; fluctuated slightly only at a SNR of 4 and 3 on the vertical energy function; and lastly, jumped form 2ms to around 2.8ms when the SNR was less than 3 on the horizontal energy function.

Figure 2-12 emphasizes the importance of the STA threshold to avoid false triggers. The STA/LTA threshold of 2.3 is surpassed around 0.88s, and prior to the actual arrival of the P-wave around 0.51s, thereby triggering false events in the absence of an STA threshold.

The energy technique applied to synthetic data using the total, vertical and horizontal energy functions was assessed here in section 2.3.2. From such evaluations I conclude that the total energy function is the more robust function. Thus from now on, I will not be performing event picking on the horizontal and vertical energy functions.

2.3.3 Evaluation of Onset-time Correction Applied to the Energy Technique

Using the synthetic microseismic events depicted in the previous sections, I aim to evaluate the value of the onset-time correction applied to the energy procedure for detecting and picking events. I will be comparing only the final onset-time picks for the energy technique with and without the onset-time correction as the trigger procedure for this algorithm is the same as that performed in section 2.3.2. Furthermore, I aspire to determine how sensitive this energy procedure is under various conditions such as the minimum arrival time interval, and specific false triggers. The standard synthetic model that I will be altering is the same one that is described in the section 2.3.

Similar to section 2.3.2, I have varied the dominant frequencies and relative amplitudes of the P-and S-waves, as well as changing the SNR and the background noise type. The overall results for a ray oriented with an azimuth and an inclination ranging from (0 to 90)° are compared in Figure 2-14.

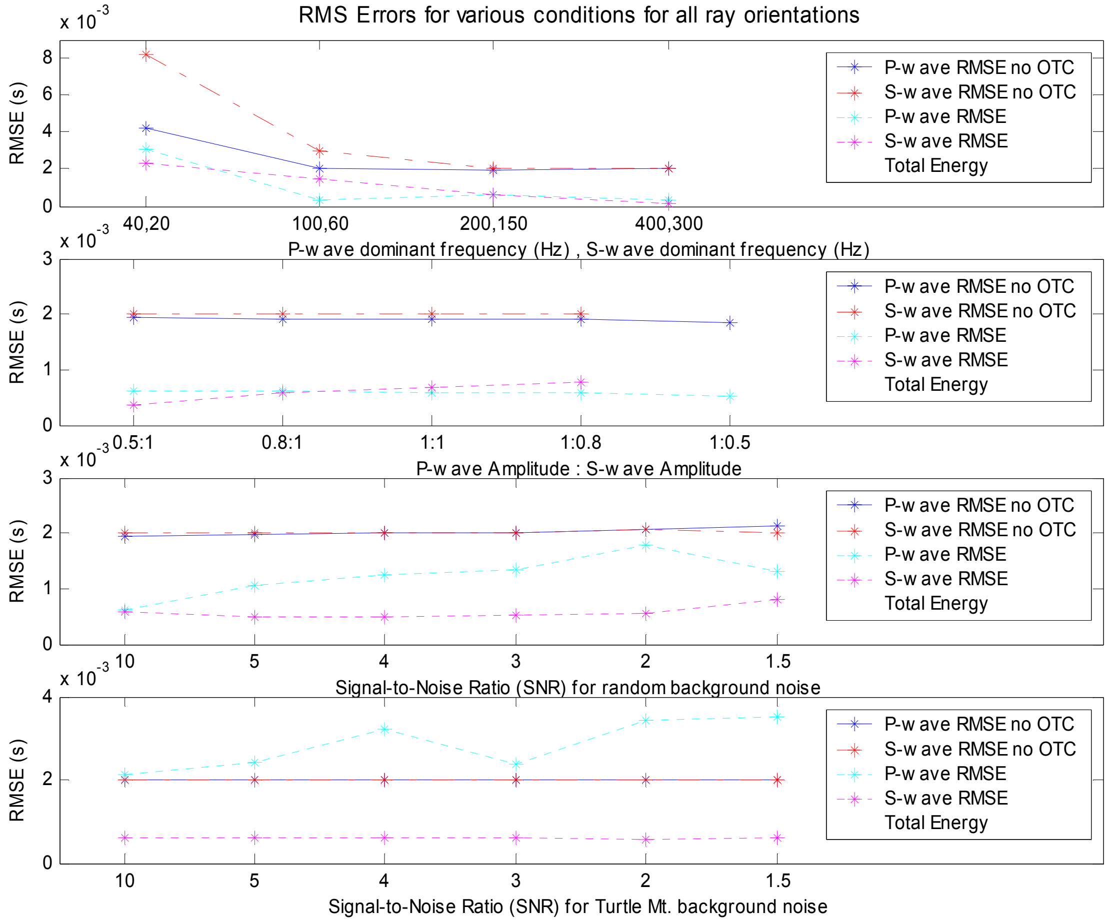

Figure 2-14 RMS errors for various conditions comparing the energy technique without an onset-time correction (OTC) and with an OTC applied.

When the dominant frequencies of the seismic waves were varied, the arrival time errors for the S-wave and especially the P-wave have noticeably decreased in comparison to the energy technique where an onset time correction was not applied. The mean time pick for the P- and S-waves detected at dominant frequencies of 200Hz and 150Hz, respectively, and at higher frequencies was found to be of around 0.5ms, as opposed to 2ms for no onset-time correction see Figure 2-14. It should be noted that for the P-wave the number of events that are undetected or grossly erroneous for the lowest frequency attempted at 40Hz, and 20Hz, were found to change in comparison to the results prior to the onset time correction. The onset-time correction was found to have an adverse effect on the number of erroneous events for the P-wave, increasing the value from (0 to 28) %. This undesirable outcome is directly related to the value of the maximum gradient of the STA/LTA around the trigger time being lesser for lower frequencies, thus the onset-time correction has moved the time pick more than 10ms behind the true arrival of the event.

Varying the relative amplitudes of the P- and S-waves for this energy technique with an onset-time correction led to the same amount of undetected events as the energy technique without the onset correction time applied, as expected. The S-wave errors fluctuated from 0.5ms to 0.7ms as its amplitude was reduced with respect to the P-wave's see Figure 2-14. The P-wave was found to be insensitive to changing relative amplitudes, remaining almost constant at around 0.6ms. Overall the P-and S-wave RMS errors were reduced by around 1.5ms with the application of the onset-time correction.

As the random background SNR was decreased the P-wave errors always remained equal to or greater than the S-wave error with the onset-time correction applied. Again the number of undetected or grossly erroneous triggers was identical to that seen without the onset time correction applied. The S-wave errors decrease slightly from 0.5ms to 0.4ms as the SNR goes from 10 to 4. The errors then rise a little to 1ms as the SNR is reduced to 1.5. P-wave errors start at about 0.5ms for a SNR of 10, and increase steadily to around 1.8ms for a SNR of 2, then decrease slightly as the SNR reaches 1.5, see Figure 2-14. Generally the RMS errors are reduced for both the P-and S-wave with the application of the onset-time correction. The S-wave RMS errors were reduced by

1.5ms on the whole, while the reduction of the P-wave RMS errors diminished as the SNR was reduced.

When the background noise was taken directly from a microseismic event recorded at Turtle Mt., AB, the P-wave picking errors were exacerbated as the SNR was decreased. The S-wave errors remained constant at 0.5ms for all SNR's, although the number of events considered undetected did increase dramatically in comparison to the random noise background alike the results prior to the onset-time correction. P-wave picking errors fluctuated between 2ms and 3.8ms as the SNR was reduced. In general the S-wave RMS errors were reduced by the application of the onset-time correction by 1.5ms, while the P-wave RMS errors were actually increased by varying amounts to a maximum of 1.8ms for a SNR of 1.5, see Figure 2-14.

P-and S-wave arrival time interval's influence on picking

The response of the energy technique with an onset time correction applied to a decrease in the time interval between the arrival times of the primary and secondary waves (P-and S-waves) is investigated by using synthetic data with known arrival times. For this technique the intervals were set to 70ms, 40ms, 30ms, 25ms, 20ms, and 10ms to illustrate the extent that this energy technique can be compelled before the S-wave arrival cannot be distinguished from the P-wave coda for all ray orientations. Notice that the time interval used for the 'standard' synthetic model is taken to be 0.070s.

Figure 2-15 illustrates the total energy of the signal and the STA/LTA for two arrival time intervals of 25ms and 20ms. Figure 2-16 displays the percentage of undetected or vastly erroneous events when varying the arrival time interval.

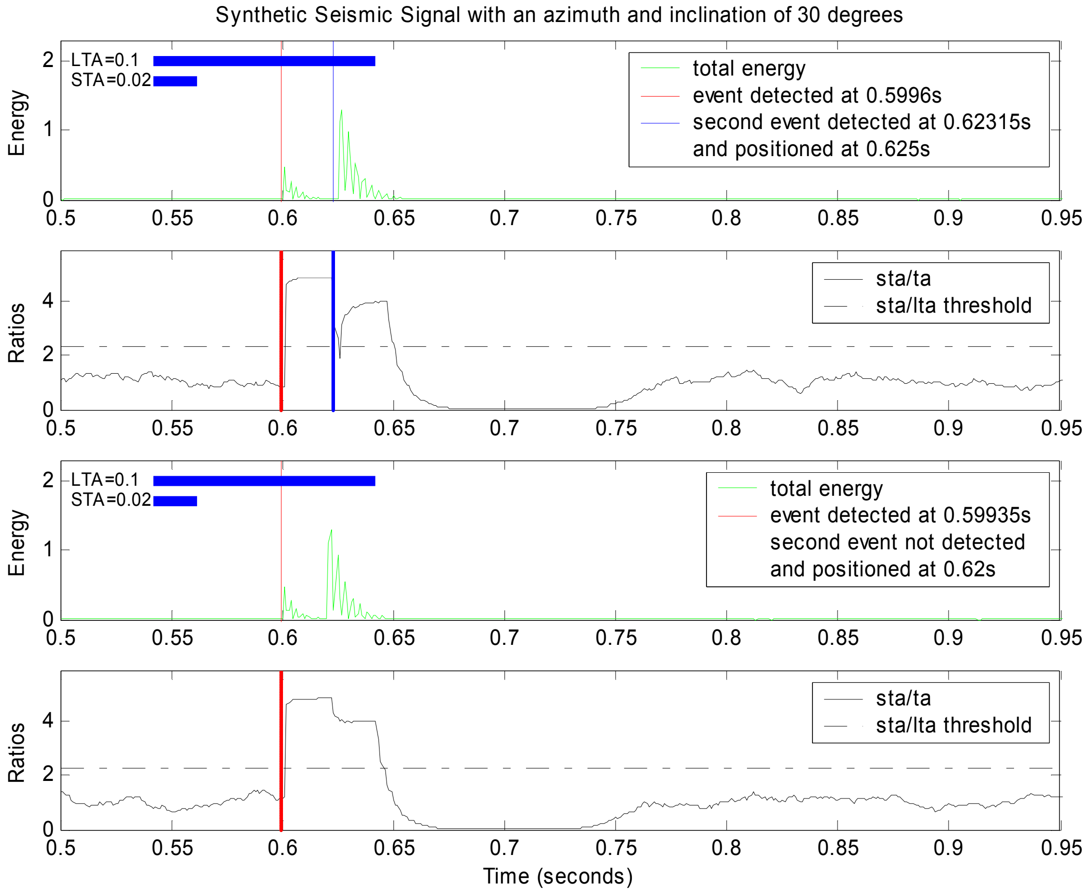

Figure 2-15 top to bottom: Total energy for synthetic event with an azimuth and an inclination of 30°, an onset time correction applied and an arrival time interval of 25ms; STA/LTA; total energy for synthetic event with the same orientation, an onset time correction applied and an arrival time interval of 20ms; STA/LTA. Red line indicates the maximum gradient corrected time for the first P-wave arrival time. The blue line represents the second event arrival time, corresponding here to the S-wave.

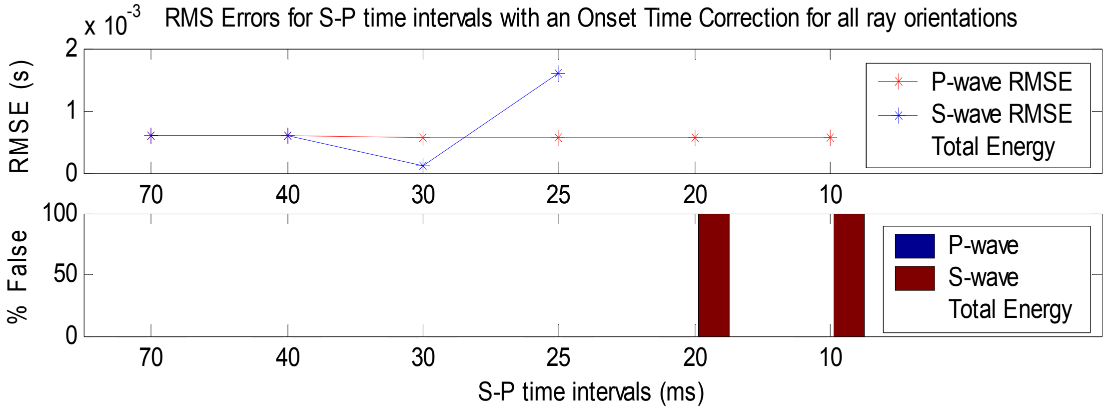

Figure 2-16 RMS errors and percentage of false triggered or undetected events for an arrival time interval ranging from 70ms to 10ms with an onset time correction applied.

Figure 2-15 illustrates the key limiting step in calculating the arrival of two distinct seismic phases for this energy technique. That is, the STA/LTA of the total energy of the 3-C signal loses the resolution of the two separate waves that rise above the background noise and surpass the pre-defined threshold as the time interval between arrivals in reduced from 25ms to 20ms. The time spans of these waves are dependent upon the size of the STA window. Thus, decreasing the STA window may allow the energy technique to resolve the two separate arrivals when the arrival time interval is smaller than between 25ms and 20ms. However, the size of the STA window selected is dependent upon the frequency of the anticipated arrivals.

From Figure 2-16 it can be seen that for the total energy function the resolution of the P-and S-wave arrivals has diminished between an arrival time interval of 25ms and 20ms. The onset picking errors for the S-wave fluctuate as the arrival time interval is reduced from 70ms to 10ms, however, the P-wave remained constant at around 0.5ms.

False Triggering on Selected Background Noises

False triggers from certain background noises are possible when using this energy procedure. Here I will examine its effectiveness on a high-amplitude short-duration impulse and a small-amplitude long-duration sine wave that are both representative of noises; the findings are portrayed in Figure 2-17 and illustrated in Figure 2-18. The sine wave is positioned at a time of 0.5s, and the impulses are positioned with increasing amplitudes of 0.25, 0.5, and 1 at times of 1.2s, 1.3s, and 1.4s, respectively.

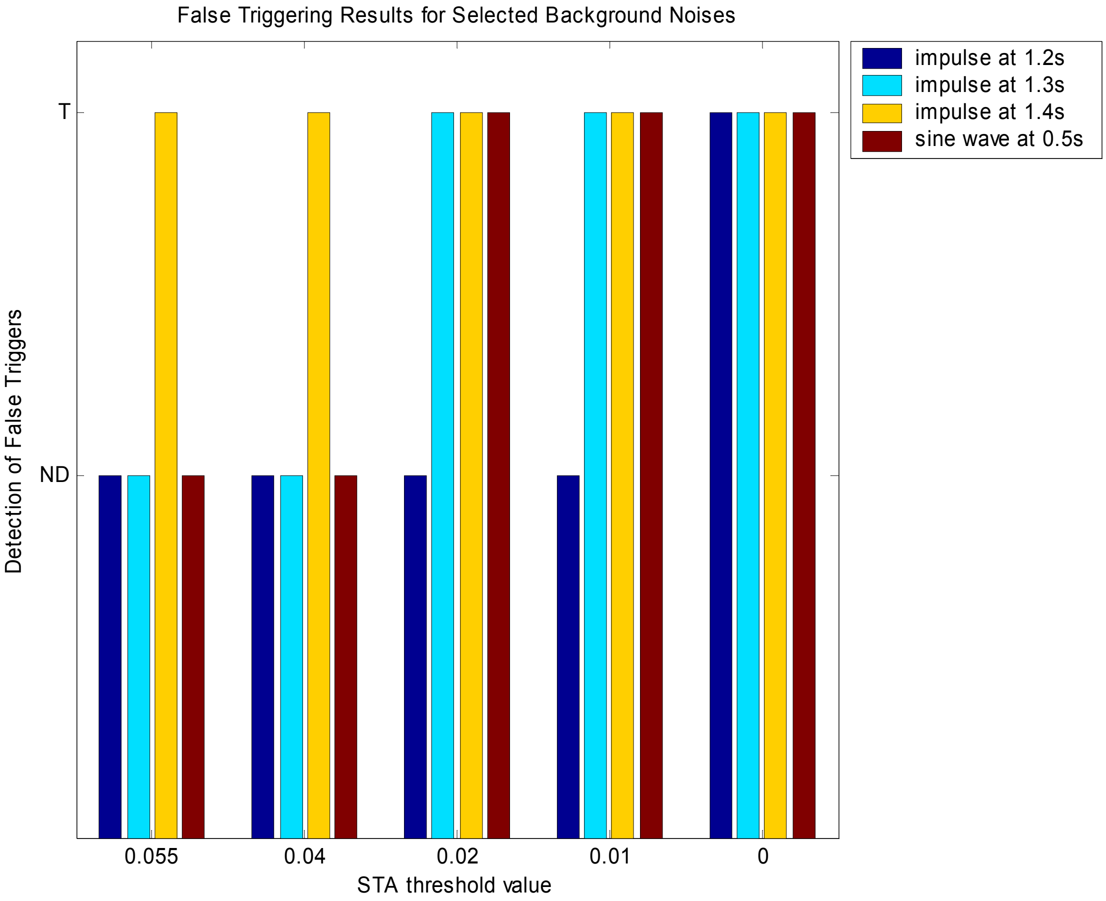

Figure 2-17 False triggering results for selected background noises. ND represents not detected, while T represents triggered.

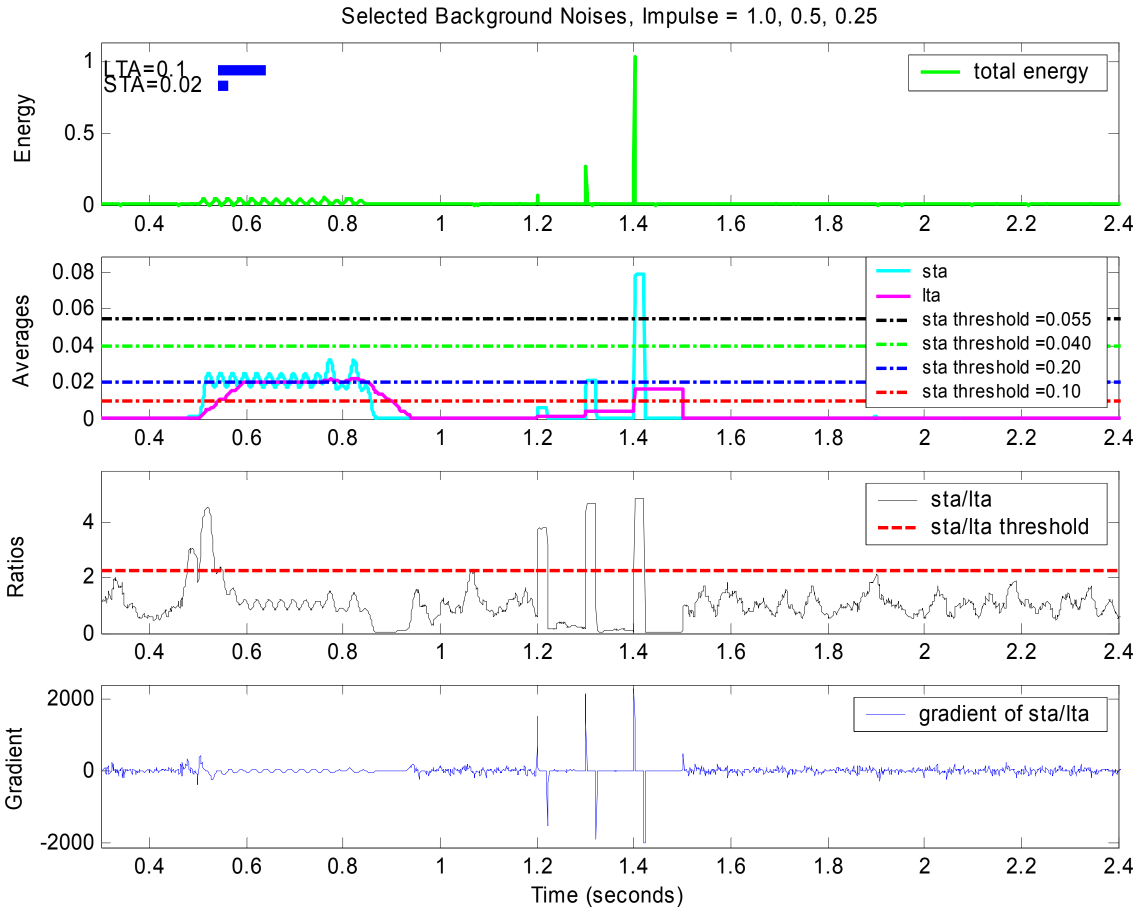

Figure 2-18 top to bottom: Total energy for selected background noises as indicated in the text; STA and LTA; STA/LTA; Gradient of the STA/LTA.

To investigate the false triggers that would be detected using this energy technique I attempted three impulse signals ranging in maximum amplitude from 1 to 0.25, as well as a low-amplitude harmonic noise. Figure 2-18 illustrates the false trigger signals. From Figure 2-17 it is obvious that if there was no STA threshold imposed all the impulses and low-amplitude harmonic noises would trigger this system. The smallest impulse still generates a large STA/LTA and would trigger incorrectly. The same is true of the sine wave with a dominant frequency of 20 Hz. Thus, the addition of an STA threshold aids in suppressing false triggers.

Multi-window Amplitude Technique

2.3.4 Multi-window Amplitude Technique Theory

It is possible to distinguish a seismic signal from background noise using instantaneous amplitude computations from a 3-component geophone in conjunction with its averages over three moving windows in the time-domain (Chen and Stewart, 2005). This procedure is similar to energy techniques in that it involves a characteristic function of the absolute value, or the square of the seismic trace; moving windows alike the short-term average and long-term average windows; and ratios of the windows comparable to the STA/LTA.

The three moving windows are measurements of the SNR within time regions before, after, and after a delay of specified length. I define the absolute amplitudes within the BTA (Before Term Average), ATA (After Term Average) and DTA (Delayed Term Average) windows respectively, following (Chen and Stewart, 2005):

$$\overline{BTA(t)} = \frac{\sum_{i=1}^{m} | u(t-i) |}{m}, \tag{2.3-7}$$

$$\overline{ATA(t)} = \frac{\sum_{j=1}^{n} | u(t+j) |}{n}, \tag{2.3-8}$$

$$\overline{DTA(t)} = \frac{\sum_{k=1}^{q} | u(t+k+d) |}{q}, \tag{2.3-9}$$

where |*u(t)*| is calculated according to equation (2.3-10); m, n, and q represent the lengths of the windows in time respectively; d is the delay for a DTA window:

$$\begin{aligned} |u_E(t)| &= |x(t)| + |y(t)| + |z(t)| \\ |u_Z(t)| &= |z(t)| \end{aligned} \tag{2.3-10}$$

Here x, y, and z represent the amplitude of the seismic trace at a time point t corresponding to the three un-rotated components and u_E and u_Z will be called the 3-C magnitude and Z-component magnitude functions respectively.

Three standards are selected to evaluate the arrival of a seismic event. The first is based on the instantaneous absolute amplitudes |*u(t)*|; the other two standards $R_2(t)$ and $R_3(t)$ are based on the ratios of the averages ATA and DTA to BTA as follows:

$$\begin{aligned} R_2(t) &= \frac{\overline{ATA(t)}}{\overline{BTA(t)}} \\ & \qquad . \\ R_3(t) &= \frac{\overline{DTA(t)}}{\overline{BTA(t)}} \end{aligned} \tag{2.3-11}$$

The later two standards are intended to discern high-amplitude short-duration and long-duration noise respectively.

The basis of these functions is justified as follows. In the situation where the first threshold, $H_1(t)$, is exceeded at a particular point in time t, the second standard $R_2(t)$, is employed to separate a high-amplitude short-duration noise from a high-amplitude long-duration event. Notice from the definition of $R_2(t)$ in equation (2.3-11) that $R_2(t)$ will be faintly affected in the situation where the ATA window contains noise. This is because the length of this window, ATA, is thought to be a number of times longer than the duration of the noise; however, it will be greatly amplified when the ATA window contains only a segment of a seismic event; therefore $R_2(t)$ has the ability to exclude the short-duration noise. From the definition of $R_2(t)$ it is seen that it will no longer be able to discriminate a seismic event from noise when the high-amplitude noise has a duration that is comparable to the length of the ATA window. False triggers as a result of this high-amplitude long-duration noise will be avoided when the final standard $R_3(t)$ is considered, as with a suitable delay time it will not surpass the threshold; thus all three standards will not exceed the specified thresholds at the same time.

It is possible to pre-define the thresholds for the $R_2(t)$ and $R_3(t)$ standards, H_2 and H_3, respectively based on a fraction of the anticipated SNR. The threshold for the first standard, $H_1(t)$ is evaluated throughout time; it should be substantial in comparison to the fluctuations of most noise but subordinate to the expected signal. This can be achieved by measuring the mean (E_m) and the standard deviation (E_{sd}) of the envelope $(E(t))$ of the pre-existing noise within the BTA window. The envelope is obtained for a 3-component recording from the summation of the absolute values of the Hilbert transforms of a each seismic trace component (i.e., z(t),x(t),y(t)). The envelope for a single z-component trace is computed similarly, except only using the z(t) trace. In practice, $H_1(t)$ is shifted a few samples points backwards to evade the premature escalation of $H_1(t)$ instigated by the first arrival. Thus, they define an instantaneous $H_1(t)$ to be:

$$H_1(t) = E_m(t-p) + \alpha E_{sd}(t-p)\,, \tag{2.3-12}$$

where p is the number of shifted sample points in time; α is a coefficient to regulate the height of the first threshold; it is set to a value of 3, thereby insuring that $H_1(t)$ will not be surpassed by 99% of the noise (Chen and Stewart, 2005). Notice from equation (2.3-12) that $H_1(t)$ is automatically regulated according to the variance of the background noise.

Once again the delayed trigger time is compensated for by the onset time correction as described previously in section 2.3.1 with a few modifications. Instead of using the STA/LTA threshold I am now using the $H_1(t)$ threshold, and using the gradient of the absolute amplitude and its height at which the threshold is surpassed, not the maximum gradient taken within an envelope surrounding that trigger time, see Figure 2-19.

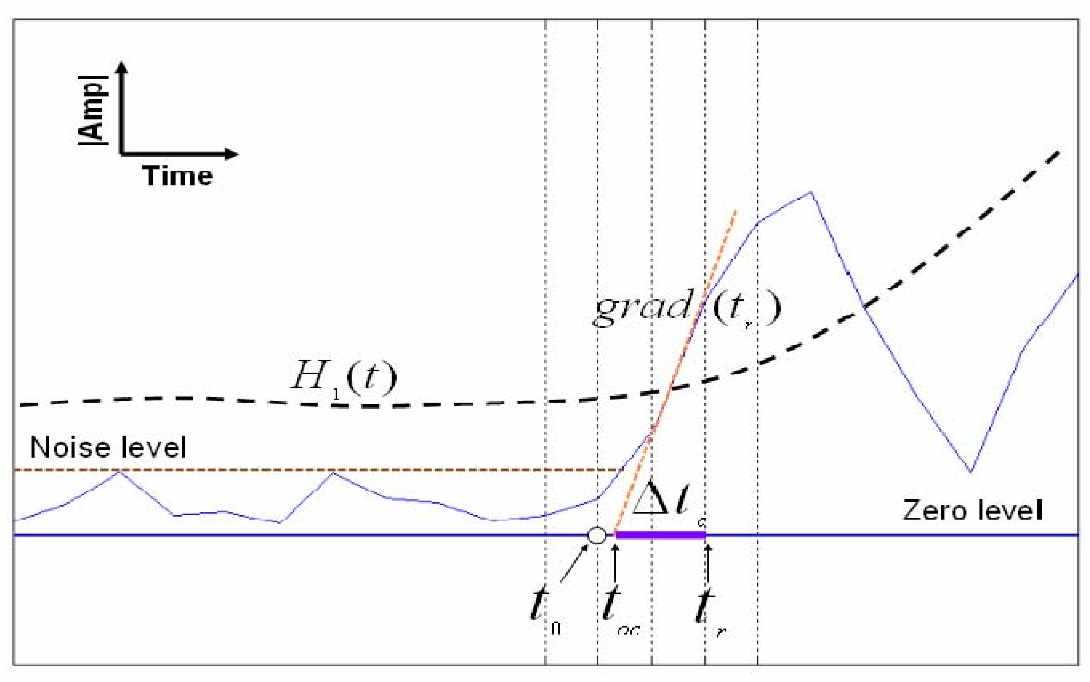

Figure 2-19 Schematic diagram showing the items used in the onset time correction to a trigger point (t_r) for corrected onset time (t_{oc}) of an event. Red dashed line represents the adopted gradient, which is the maximum gradient adjacent to time point t_r. The thick purple line represents the calculated amount of onset time correction (Δt_c); Open circle is the real onset time (t_0) (Chen and Stewart, 2005).

2.3.5 Analysis of Multi-window Amplitude Technique using Synthetic data

To determine the efficiency of the multi-window technique at detecting and picking events under various conditions I will use synthetic data with known arrival times as discussed previously in section 2.2. The length of the windows chosen are dependent upon the anticipated frequency of the events, thus, I aim to use such window lengths that may be suitable for all conditions attempted. Unfortunately, because of the vast range of frequencies I aspire to challenge, I was only able to find a window that suited all cases except the lowest frequencies.

Frequency dependency of picking

To inspect the effects of altering the dominant frequencies of the waves, while keeping the dominant frequency of the P-wave greater than that of the S-wave, I have attempted frequencies between 20 Hz and 400 Hz, with various relative ratios. Once again, to ensure that the picking errors are not based on the random background noise added, the algorithm was performed one hundred times, and then the mean of the absolute error was resolved. The calculations preformed in detecting an event and determining its onset time for a P-wave frequency of 200 Hz, and an S-wave frequency of 150 Hz are illustrated for a wave propagating with an azimuth and an inclination of 30° in Figure 2-20. The overall results for a ray oriented with an azimuth and an inclination ranging from (0 to 90)°and for a P-and S-wave dominant frequency ranging from 20 Hz to 400 Hz are illustrated in Figure 2-21.

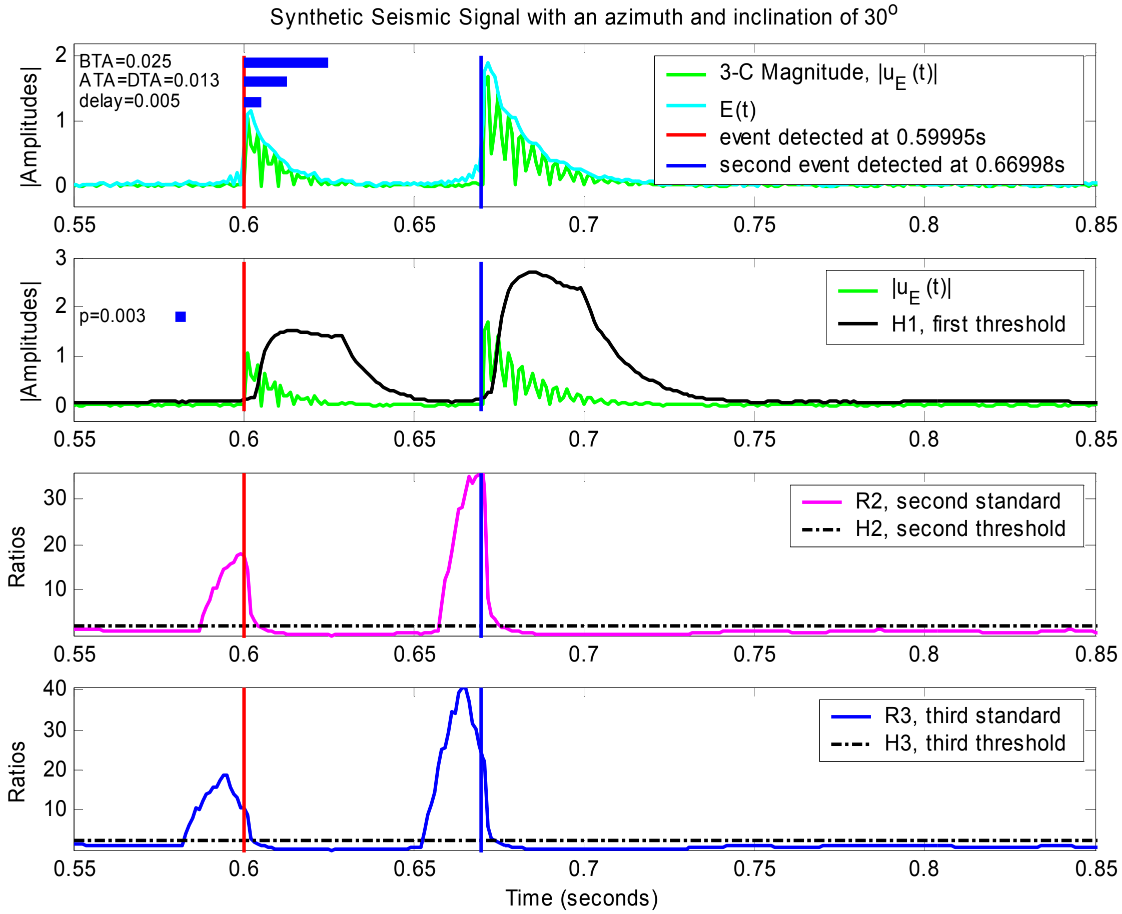

Figure 2-20 3-C Magnitude for synthetic event with an azimuth and an inclination of 30° and a P-wave and S-wave dominant frequency of 200 Hz, and 150 Hz, respectively. Diagrams from top to bottom represent the absolute value of the synthetic seismogram (green) and its envelope (light blue); first standard $|u(t)|$ (green) and variable threshold H_1 (black); second standard R_2 (magenta) and threshold H_2 (black, dashed); third standard R_3 (blue curve) and threshold H_3 (black,dashed). The lengths of the moving time windows are displayed in the top left corner, where delay is the length of the delay until the delayed time window of length is measured.

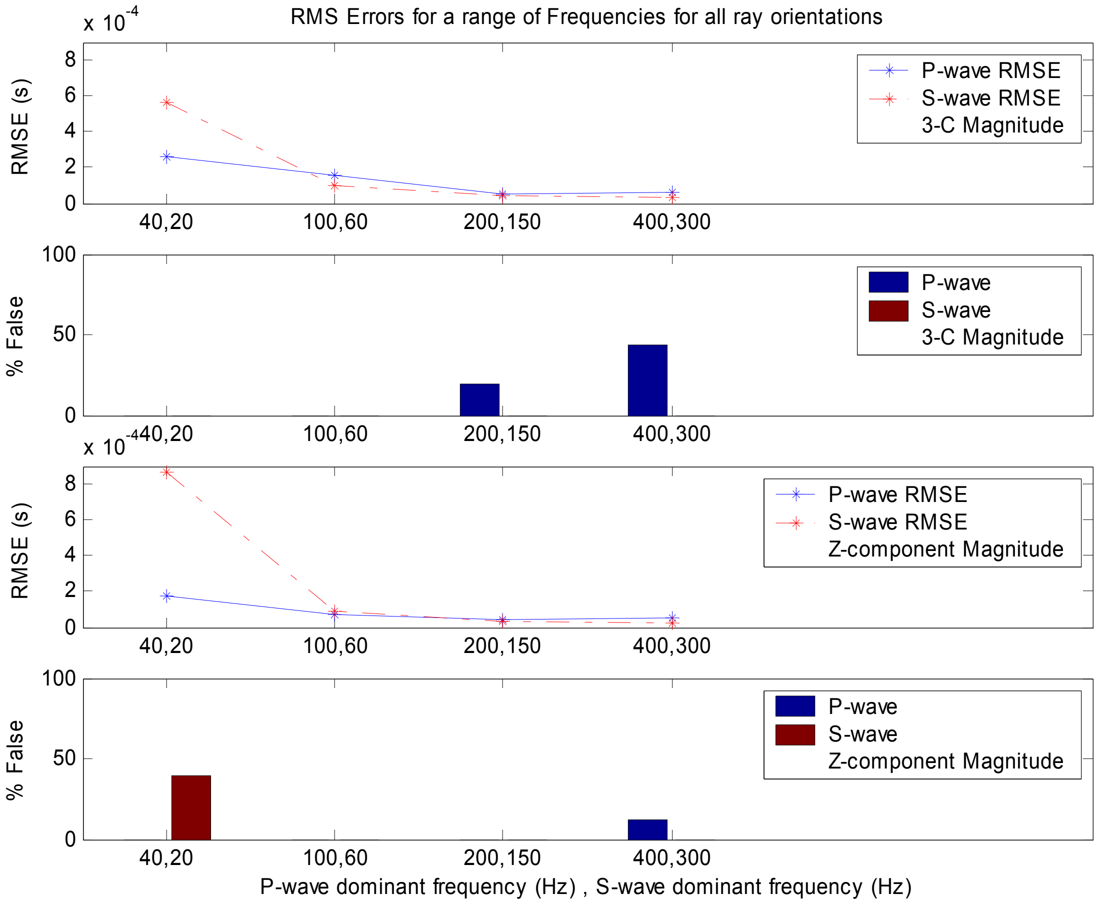

Figure 2-21 RMS errors and percentage of false triggered or undetected events for wave frequencies ranging from 20Hz to 400Hz and an onset time correction applied.

As the frequencies of the seismic waves were increased, once again, I see a decrease in arrival errors. As the dominant frequencies of the P-and S-waves were increased from 200Hz and 150Hz, respectively their errors diminished from around 0.1ms to around 0.01ms.

Amplitude dependence of Picking

To inspect the outcome of varying the relative amplitudes of the waves, I have attempted the following amplitude relations:

1. $A_P = A_S = 1$
2. $A_P > A_S$
3. $A_P < A_S$
4. $A_P >> A_S$
5. $A_P << A_S$.

The calculations preformed in detecting an event and determining its onset time for a P-wave amplitude 25% greater than the S-wave's are illustrated for a wave propagating with an azimuth and an inclination of 30° in Figure 2-22. The overall results for a ray oriented with an azimuth and an inclination ranging from (0 to 90)° and a P-to S-wave relative amplitude ratio ranging from 0.5 to 2 are illustrated in Figure 2-23.

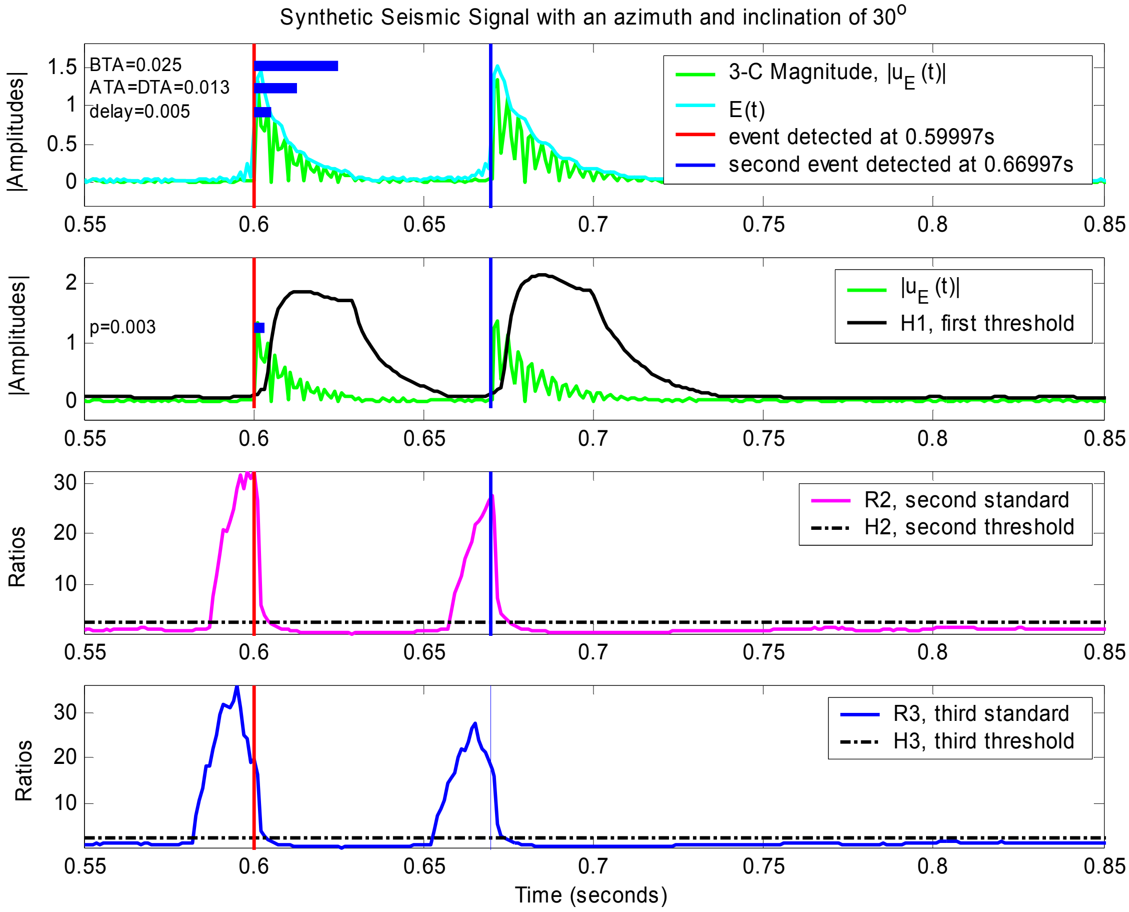

Figure 2-22 Total absolute amplitude for synthetic event with an azimuth and inclination of 30°, and a P-wave amplitude that is 25% greater than its S-wave's. The remarks are the same as in Figure 2-20.

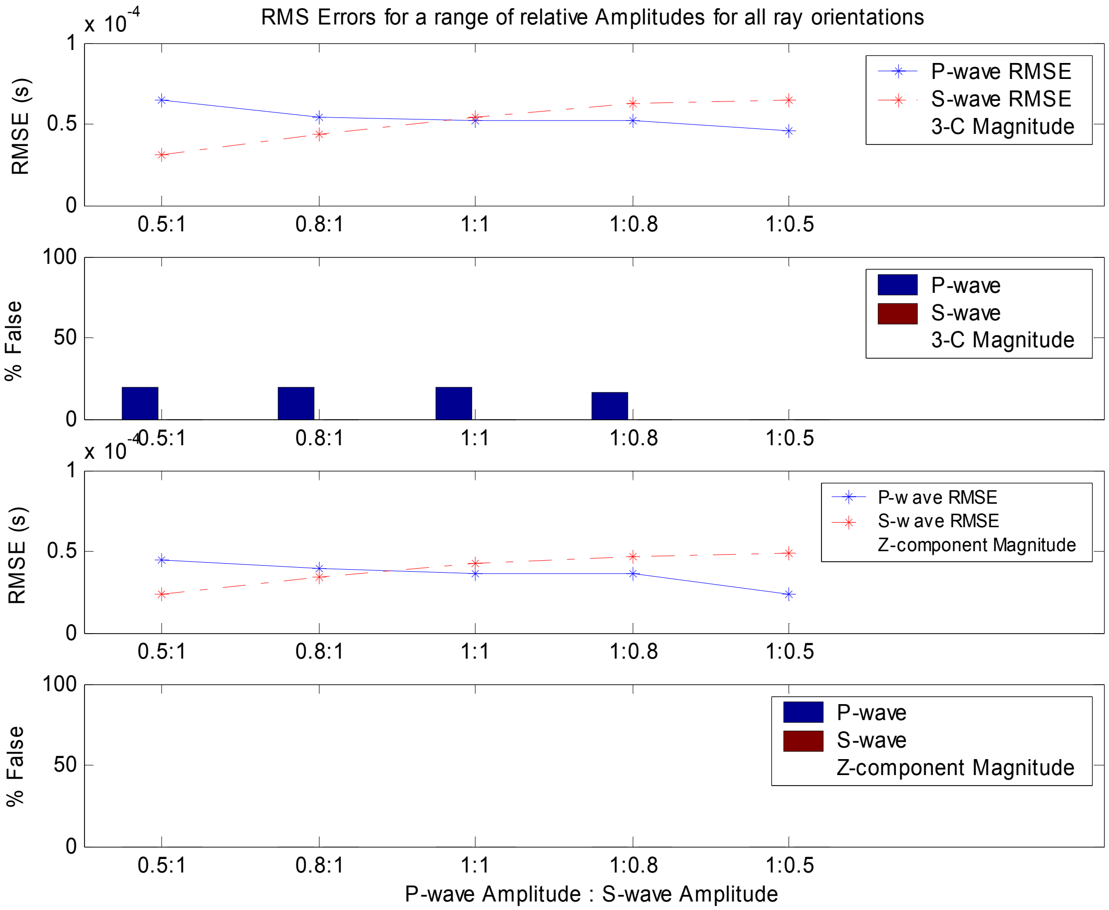

Figure 2-23 RMS errors and percentage of false triggered or undetected events for relative wave amplitudes ratios ranging from 0.5 to 2 with an onset time correction applied.

When altering the relative amplitude's of the two waves there appears to be a smaller error when their amplitudes are the largest. It is very interesting to see that the percentage of undetected or erroneous events for the secondary arrival did not appear, nor vary as the relative amplitudes were adjusted for the 3-C magnitude function. For the 3-C magnitude function the percent false did vary slightly for the P-wave arrival, increasing as the amplitude got smaller.

Background Noise Influence on Picking

To inspect the impact of background noise on the onset-time picks and the detection of the P- and S-wave arrivals with the onset time correction applied, I have attempted a variety of SNR's ranging from 1.5 to 10 and have taken background noise off of a recording from geophones situated at Turtle Mt., AB. The standard background noise I have used to alter the SNR is a series of random numbers that are normally distributed, with zero mean. The calculations preformed in detecting an event and determining its onset time for a background noise with a SNR of 3 are illustrated for a wave propagating with an azimuth and an inclination of 30° in Figure 2-24. The overall results for a ray oriented with an azimuth and an inclination ranging from (0-90)° and a random background noise with a SNR ranging from 10 to 1.5 are illustrated in Figure 2-25. I did attempt the same variation of SNR with a random noise that was uniformly distributed and very similar results were found.

Another form of background noise investigated was taken directly from an event at Turtle Mt., AB, on November 13, 2004 where the SNR of 100 was reduced to interrogate a variety of SNR's. The calculations preformed in detecting an event and determining its onset time for a background noise from Turtle Mt., AB, with a SNR of 3 are illustrated for a wave propagating with an azimuth and an inclination of 30° in Figure 2-26. The overall results for a ray oriented with an azimuth and an inclination ranging from (0-90)° and background noise taken from Turtle Mt., AB, with a SNR ranging from 10 to 1.5 are illustrated in Figure 2-27.

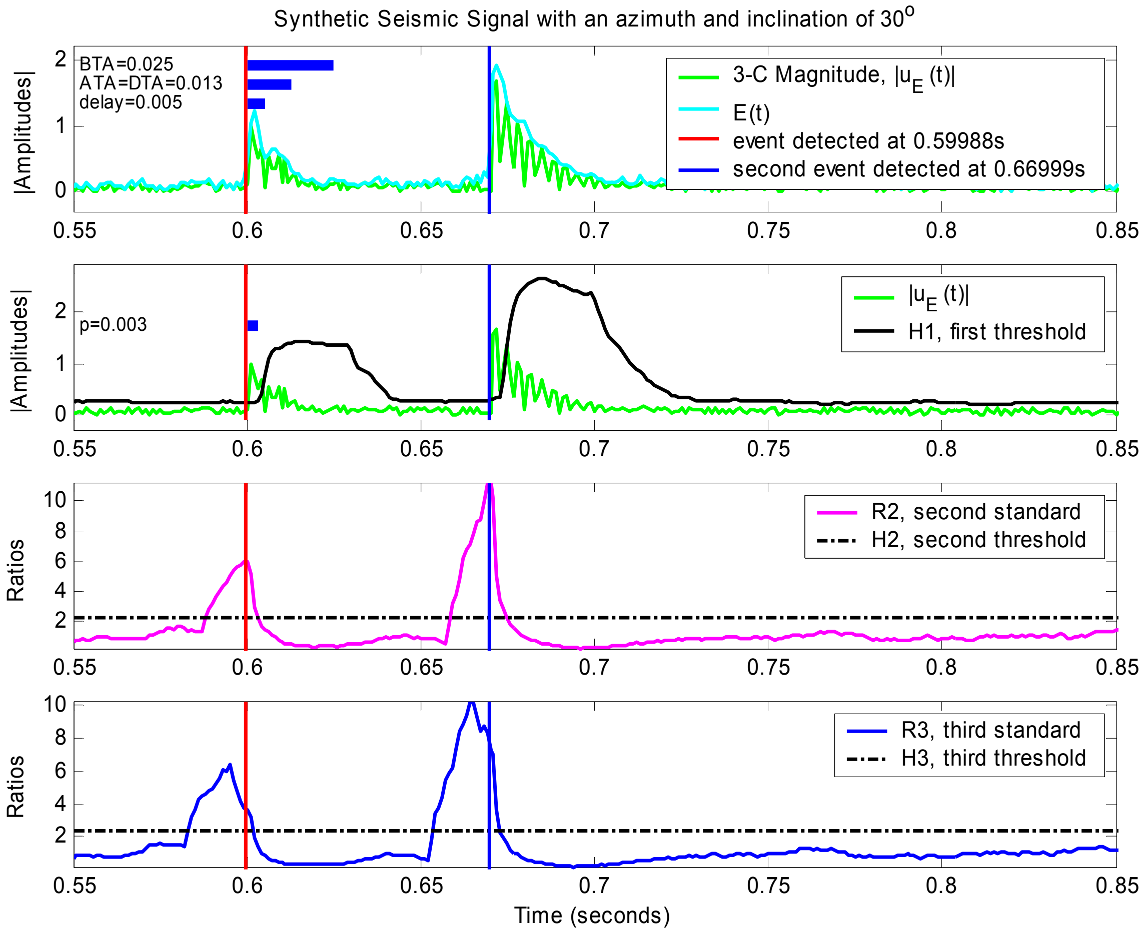

Figure 2-24 Total absolute amplitude for synthetic event with an azimuth and an inclination of 30° and a random background noise of a SNR ~ 3. Remarks are the same as in Figure 2-20.

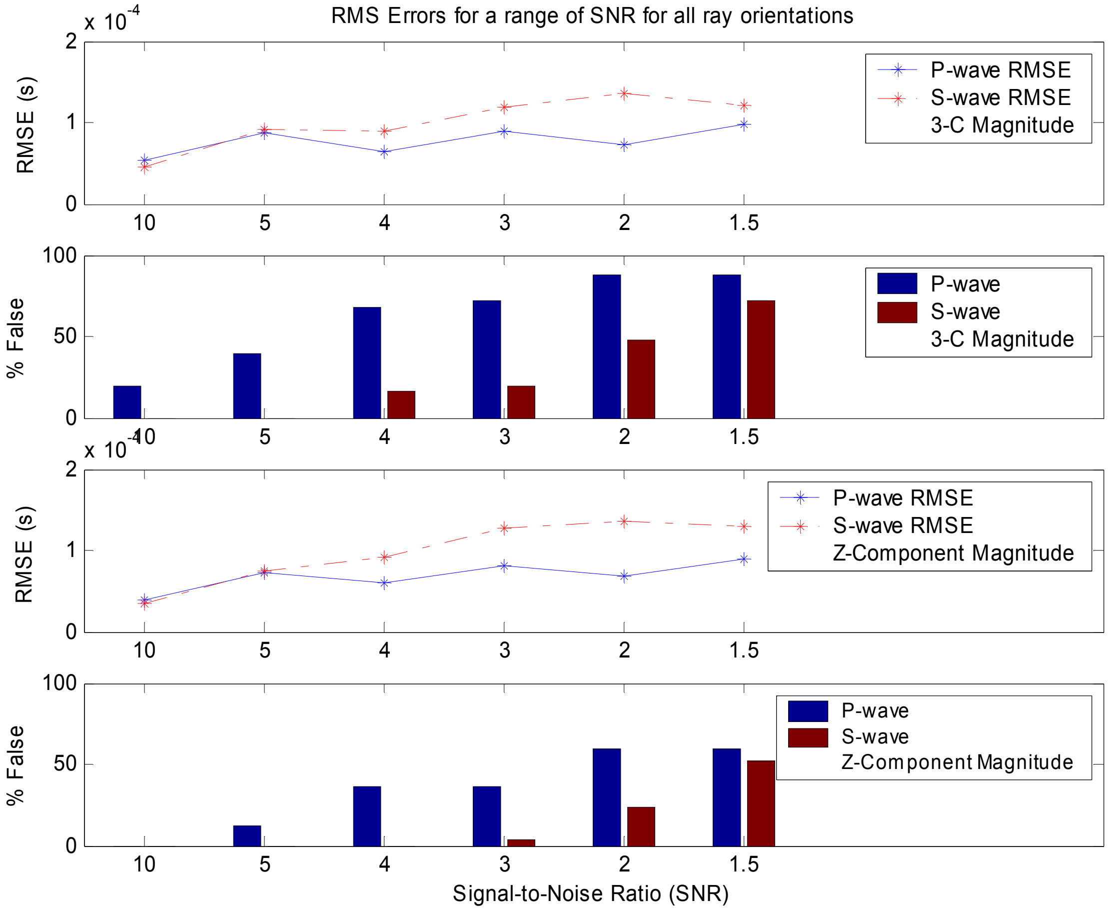

Figure 2-25 RMS errors and percentage of false triggered or undetected events for random background noise with a SNR ranging from 10 to 1.5 with an onset time correction applied.

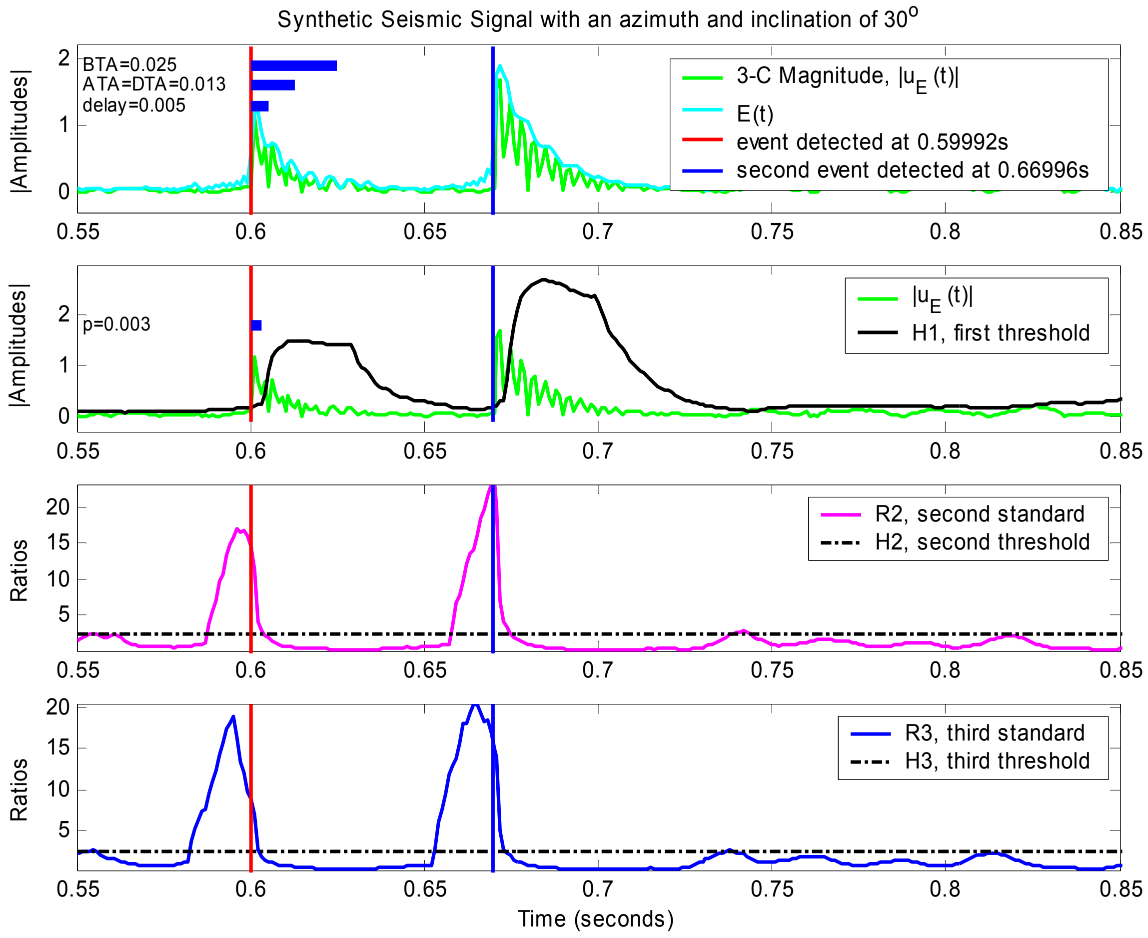

Figure 2-26 Total absolute amplitude for synthetic event with an azimuth and an inclination of 30° and a background noise taken from Turtle Mt., AB, with a SNR ~ 3. Remarks are the same as in Figure 2-20.

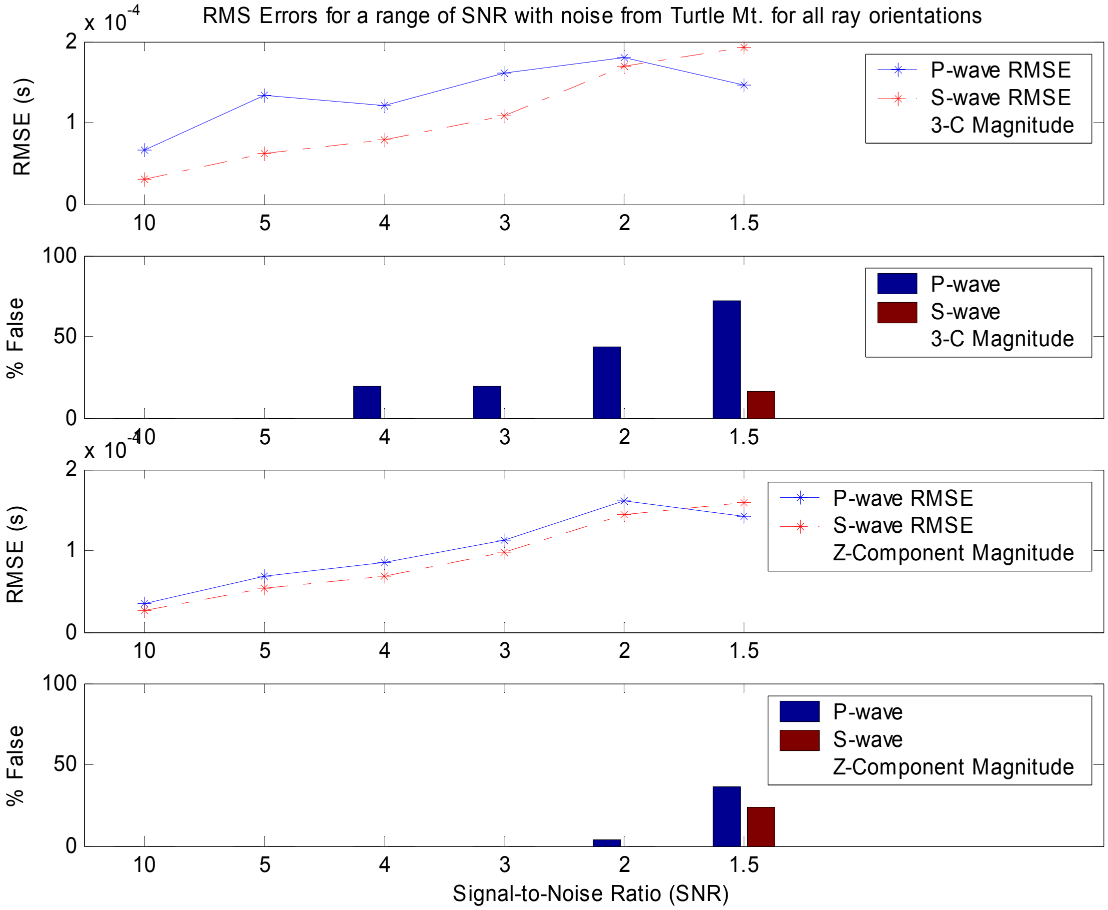

Figure 2-27 RMS errors and percentage of false triggered or undetected events for background noise taken from Turtle Mt., AB, with a SNR ranging from 10 to 1.5 and an onset time correction applied.

As the random background SNR was decreased the S-wave errors increased steadily from 0.04ms to 0.14ms for the z-component magnitude function, see Figure 2-25. Similar results were seen for the 3-C magnitude function, with the exception of a SNR of 1.5, where the S-wave error slightly decreased to 0.12ms. The P-wave errors fluctuated between 0.05ms and 0.09ms on both the functions. The number of undetected or grossly erroneous triggers for both the P- and S-wave were greater than those seen for the energy technique with the onset time correction applied. The attractive quality of the multi-window technique is that the RMS errors are an order of magnitude lower even for a low SNR.

When the background noise was taken directly from a microseismic event recorded at Turtle Mt., AB, the picking degraded as the SNR decreased, see Figure 2-27. As the SNR was reduced the P-wave errors fluctuated from 0.03ms to 0.18ms on both the functions and always remained greater than the S-wave's; the exception being for a SNR of 1.5 on both functions, where the P-wave's error is slightly less than the S-wave's. The S-wave errors also steadily increased as the SNR was lowered. The percentage of undetected or erroneous events for the P-wave, when using the Turtle Mt. background noise, increased when the SNR was decreased, however, not to the extent of the random background noise, see Figure 2-25. The S-wave's percentage of false triggers also increased with lessening SNR, however, a reduced amount of erroneous events were accounted for, in comparison to when random background noise was used.

Figure 2-26 illustrates the need for multi-windows and thresholds. Looking at Figure 2-26 at 0.745s you see that although the first threshold is surpassed by the noise, the second and third are not surpassed over the same time duration and thus no event is triggered. This is also noted at 0.825s.

P-and S-wave arrival time interval's influence on picking

Sensitivity to the time interval between the arrival times of the primary and secondary waves was investigated for the multi-window technique with an onset correction applied. For this technique I examine time intervals of 70ms, 30ms, 25ms, 20ms, 10ms and 5ms. These time intervals will illustrate the resolution capabilities for the multi-window technique or in other words to determine the point at which the S-wave arrivals cannot be distinguished from the P-wave coda. The time interval used for the ‘standard’ synthetic model is 0.070s.

Figure 2-28 illustrates the 3-C magnitude calculations for the three standards and thresholds of this signal for the two arrival time intervals of 30ms and 25ms. Figure 2-29 displays the percentage of undetected or vastly erroneous events when varying the arrival time interval. It is important to emphasize that as a result of the ray orientations examined, the maximum percentage of undetected events for the z-component’s P-and S-wave calculations are 80%, not 100%. This is because 20% of the ray orientations have only one wave arrival that could be detected.

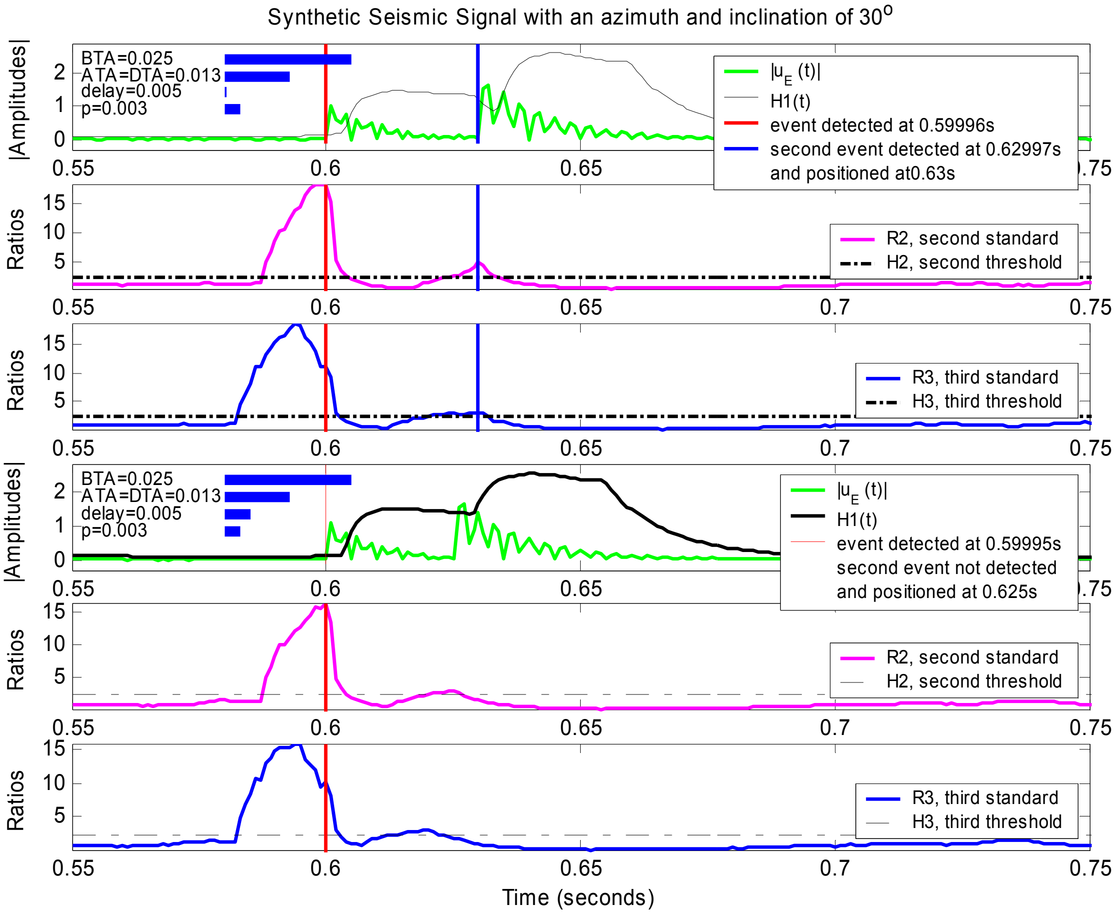

Synthetic Seismic Signal with an azimuth and inclination of 30°

Figure 2-28 Total absolute amplitude for synthetic event with an azimuth and an inclination of 30° and with arrival time intervals of 30ms and 25ms. Diagrams from top to bottom for each arrival time interval represent the first standard $|u(t)|$ (green) and variable threshold H_1 (black); second standard R_2 (magenta) and threshold H_2 (black, dashed); third standard R_3 (blue curve) and threshold H_3 (black,dashed). The lengths of the moving time windows are displayed in the top left corner, where delay is the length of the delay until the delayed time window of length is measured.

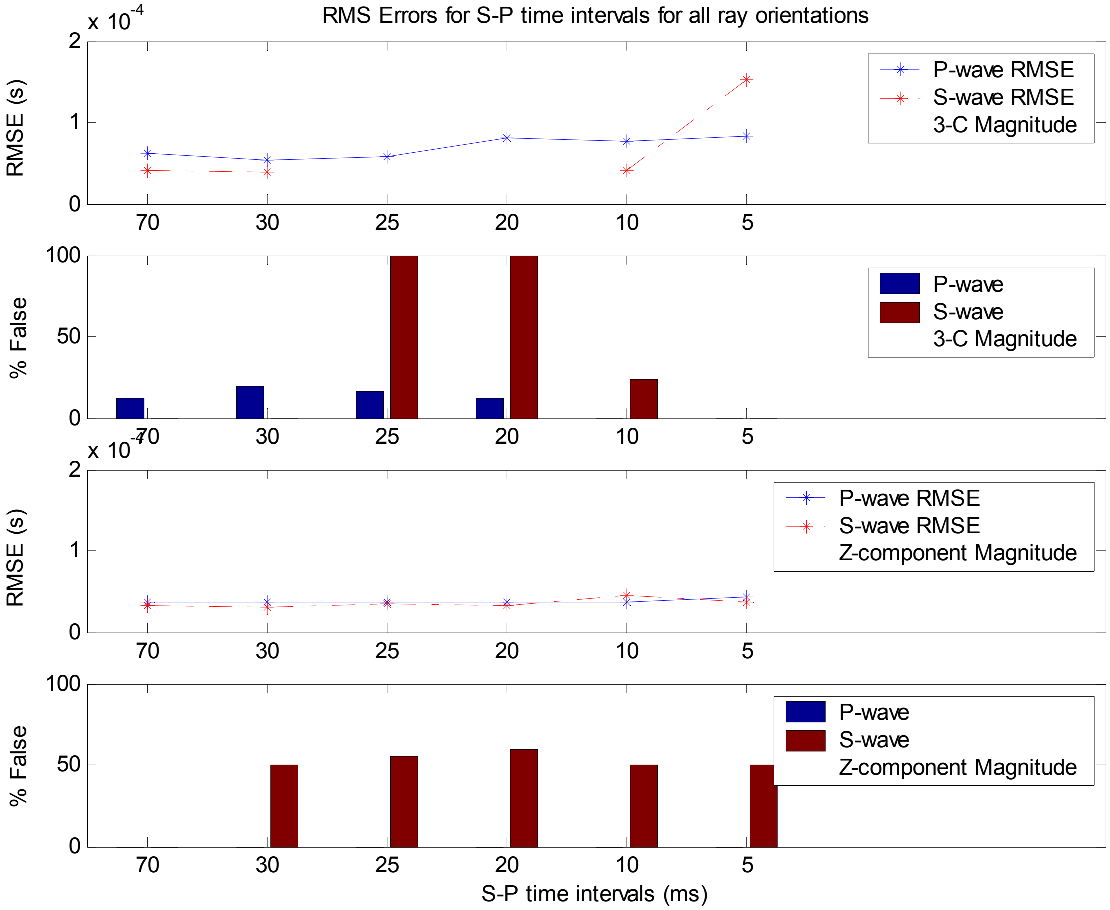

Figure 2-29 RMS errors and percentage of false triggered or undetected events for an arrival time interval ranging from 70ms to 5ms with an onset time correction applied.

Figure 2-28 illustrates the key restrictive steps in calculating the arrival of two distinct seismic events for this multi-window technique. That is when the arrival time interval is between 30ms and 25ms, despite the first threshold being surpassed, the second and third are not exceeded at the same point in time for the 3-C magnitude function.

From Figure 2-29 it can be seen that for all ray orientations the 3-C magnitude function loses its ability to resolve the P-and S-wave arrivals when the arrival interval is forced to 25ms and 20ms. This may be directly related to the relative amplitudes of the P-and S-waves. For example, if the P-wave's amplitude was greater than the S-waves, for a relatively small arrival time interval the first threshold likely will not be surpassed. The onset picking errors for the S-wave do fluctuate as the arrival time interval is reduced from 10ms to 5ms for the 3- and z-component magnitude calculations, however, the P-wave remained between 0.5 and 1ms for the 3-C function and constant at around 0.04ms for the z-component function. Programming limitations for this method do not allow the arrival time interval to be reduced beyond 5ms.

False Triggering on Selected Background Noises

To investigate false triggering from background noises with this multi-window procedure, a high-amplitude short-duration impulse and a small-amplitude long-duration sine wave are generated. The results from these selected background noises are portrayed in Figure 2-30 and illustrated in Figure 2-31. Where the sine wave is positioned at a time of 0.5s, and the impulses are positioned with increasing amplitudes of 0.25, 0.5, and 1 at 1.2s, 1.3s, and 1.4s, respectively.

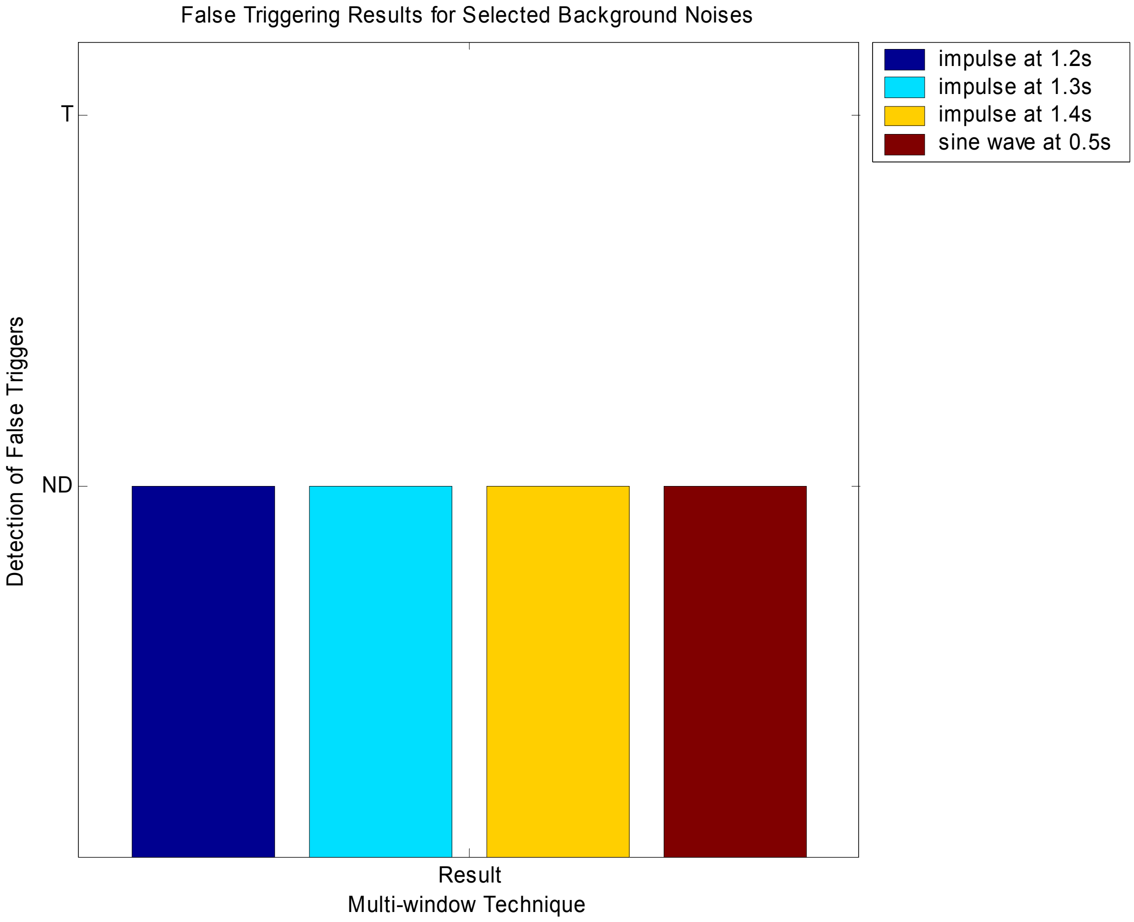

Figure 2-30 False triggering results for selected background noises using the multi-window technique. ND represents not detected, while T represents triggered.

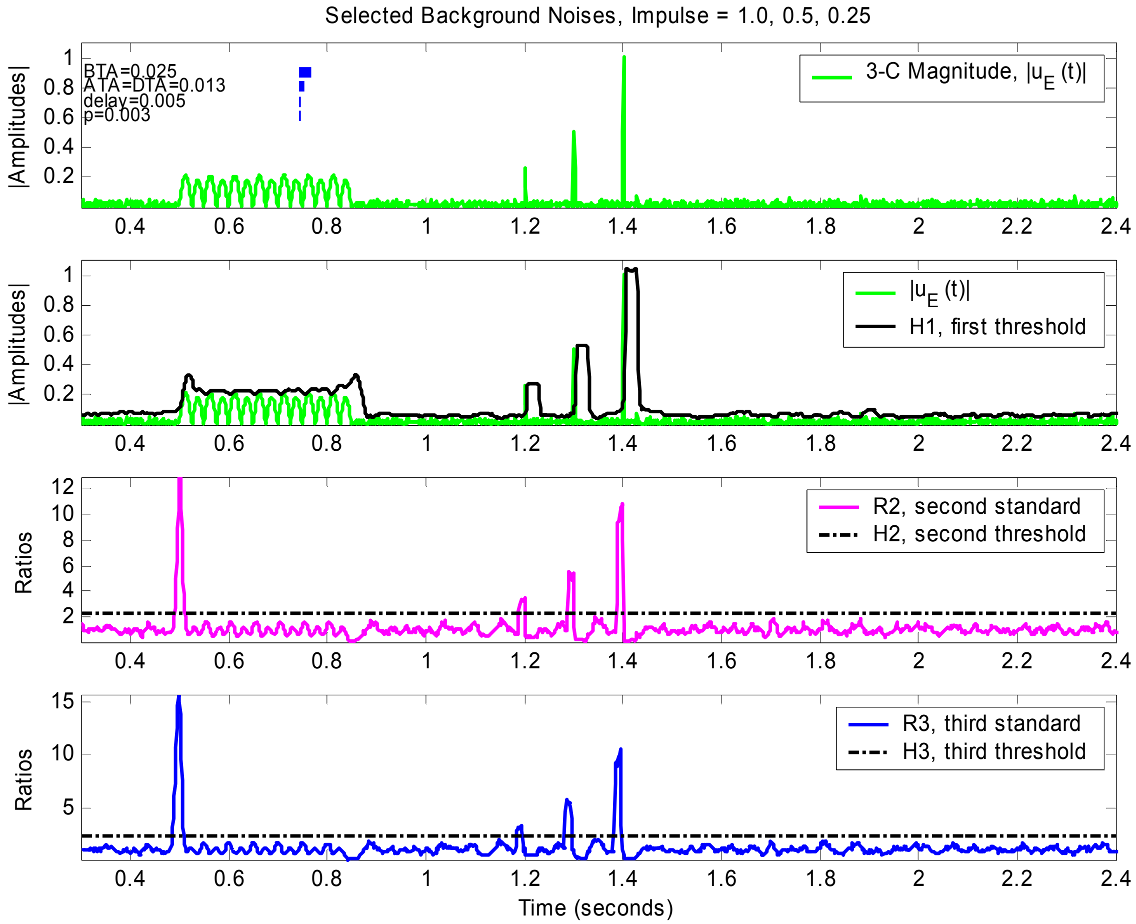

Figure 2-31 top to bottom: Total absolute amplitude for selected background noises; first standard and threshold; second standard and threshold; third standard and threshold.

I have modelled false triggering to see if the multi-window technique would detect these events. The false triggers included three impulse signals ranging in maximum amplitude from 1 to 0.25, as well as a low-amplitude harmonic noise. From Figure 2-30 it is satisfying to see that none of these noises would be detected by the multi-window technique.

2.4 Microseismic Event Detection Onset-time Picking Algorithms

Autoregressive – Akaike Information Criteria Techniques (AR-AIC)

2.4.1 AR-AIC Techniques Theories

It is possible to approximate seismic waves by an autoregressive (AR) or time series model on each properly divided time interval, i.e. a locally stationary AR model (Ozaki and Tong, 1975; Kitagawa and Akaike, 1978). Seismometers are affected by a variety of noises including traffic noise, electronic hum noise, and heavy microtremors, thus, random behaviour is observed on seismograms from mechanisms that don't generate white noise (Takanami and Kitagawa, 1988). It is sensible to presume that the spectral characteristics of a signal prior to, and after the arrival of a seismic event are dissimilar. This can be used to our advantage by selecting appropriate AR models to articulate the time series. Here I follow Takanami and Kitagawa's (1988) 'computationally efficient algorithm' for the fitting of the locally stationary AR model. This method was found to be useful for the automatic picking of onset arrival times for both P- and S-waves of microearthquakes occurring off Urakawa, Hokkaido, Japan that were recorded by the Research Centre for Earthquake Prediction (RCEP) of Hokkaido University (Takanami and Kitagawa, 1988).

The process of selecting AR model's for the background and seismic event models consists of dividing the given time series $\{ x_n ; n=1, \ldots, N\}$ into two sub-series:

$$\begin{aligned} x_n &= \sum_{m=1}^{M(1)} a_m^1 x_{n-m} + \varepsilon_n^1, \qquad (1 \le n < p_2), \\ x_n &= \sum_{m=1}^{M(2)} a_m^2 x_{n-m} + \varepsilon_n^2, \qquad (p_2 \le n \le N), \end{aligned} \tag{2.4-1}$$

where ε_n^i is a Gaussian white noise with a mean of zero and variance σ_i^2; a_m^i is the autoregressive coefficient; *M(i)* is the order of the *i*-th model, and p_2 is the unknown arrival time.

The maximum likelihood estimate of a_m^i can be obtained by minimizing σ_i^2. The estimates of the two AR models are obtained by independently fitting the AR models to $\{x_{p_1},...,x_{p_2-1}\}$ and $\{x_{p_2},...,x_N\}$ by a least squares method. The computationally efficient Householder method used for the AR model fitting is discussed by Takanami and Kitagawa (1988).

Since the model order, *M*(*i*), and the arrival time p_2 are unknown in practice, they must be obtained by minimizing the AIC criterion (Akaike Information Criterion); which was hypothesised for the discernment of the best statistical model by Akaike (1973). The AIC is computed by approximating the Kullback-Leibler information number (Kullback and Leibler, 1951) of the true distribution with regard to the presumed model, thus, it may be thought of as a ruler for the measurement of the goodness of the estimated model.

For this case of a locally stationary AR model, AIC can be computed according to Takanami and Kitagawa (1988) as:

$$AIC = -2(\text{maximum log likelihood}) + 2(\text{number of parameters}), \qquad (2.4\text{-}2)$$

where it may be evaluated as discussed by Takanami and Kitagawa (1988). The first term in equation (2.4-2) represents the prediction error for the AR model, while the second term corresponds to the degrees of freedom. As the numbers of parameters are increased the prediction errors tend to decrease.

Since the maximum likelihood depends on the value of p_2 and $M(i)$, one first fixes p_2, then minimizes the AIC to determine the best model orders, then using the orders, the selection of p_2 is altered until the minimum AIC is obtained, thus resolving the best estimate of the arrival time of the seismic waves.

This procedure is performed on the amplitudes of the three-component recordings, separately, as well as, using the summation of the AIC's over all three-components to determine an estimate for the arrival time of seismic waves. A third procedure called the multivariate locally stationary autoregressive model (MLSAR model) has been developed by Takanami and Kitagawa (1991) which removes the independence of the three-components, however despite all of the resources available I was not able to comprehend their mathematical computations. Thus, I only present an analysis on the procedures using the three-components independently.

2.4.2 Analysis of AR-AIC Techniques using Synthetic data

Using the synthetic microseismic events as depicted in previous sections I aspire to discern the efficiency of this AR-AIC procedure at picking events, and to determine how sensitive it can be under various conditions. The standard synthetic model that I will be altering is the same one that is described in section 2.2.

Frequency dependency of picking

To examine the effects of varying the dominant frequencies of the waves, while keeping the dominant frequency of the P-wave greater than that of the S-wave, I have attempted frequencies between 20 Hz and 400 Hz, with various relative ratios. To ensure that picking errors are not based on random background noise, the algorithm was performed one hundred times and the mean resolved. The computations required to detect an event and determine its onset time for a P-wave frequency of 200 Hz, and an S-wave frequency of 150 Hz are illustrated for a wave propagating with an azimuth and an inclination of 30° in Figure 2-32. The overall results for a ray oriented with an azimuth and an inclination ranging from (0-90°) and for a P-and S-wave dominant frequency ranging from 20Hz to 400Hz are illustrated in Figure 2-33. Figure 2-33 displays a graph of the RMS errors and a histogram portraying the percentage of events that are present but are not detected, or have an RMS error greater than 10ms.

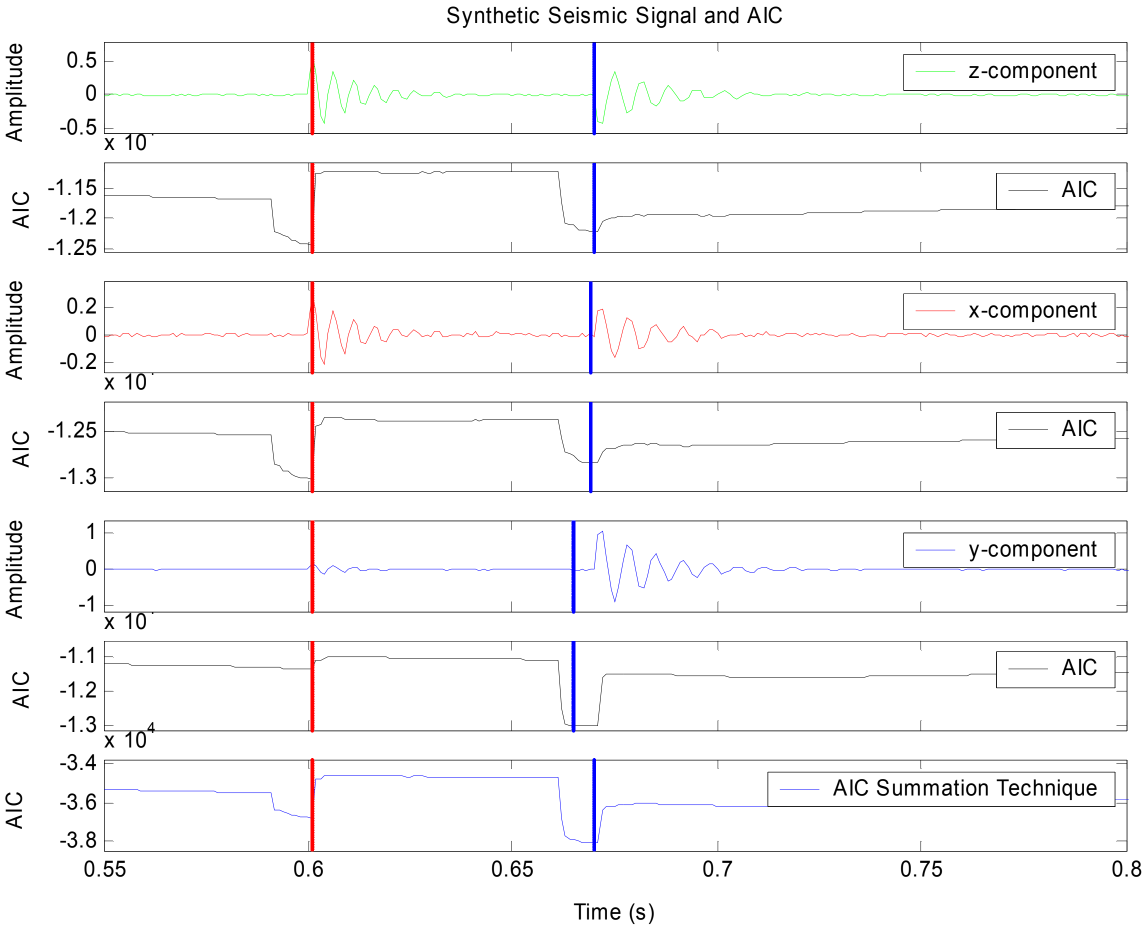

Figure 2-32 top to bottom: Z-component amplitude for synthetic event with an azimuth and an inclination of 30º and a P-wave and S-wave dominant frequency of 200Hz, and 150Hz, respectively; AIC for the AR model used above; X-component amplitude; AIC for the AR model used above; Y-component amplitude; AIC for the AR model used in above; AIC summed for all three-components. Red line indicates the detection of the P-wave arrival time. Blue line represents the second event arrival time, corresponding here to the S-wave.

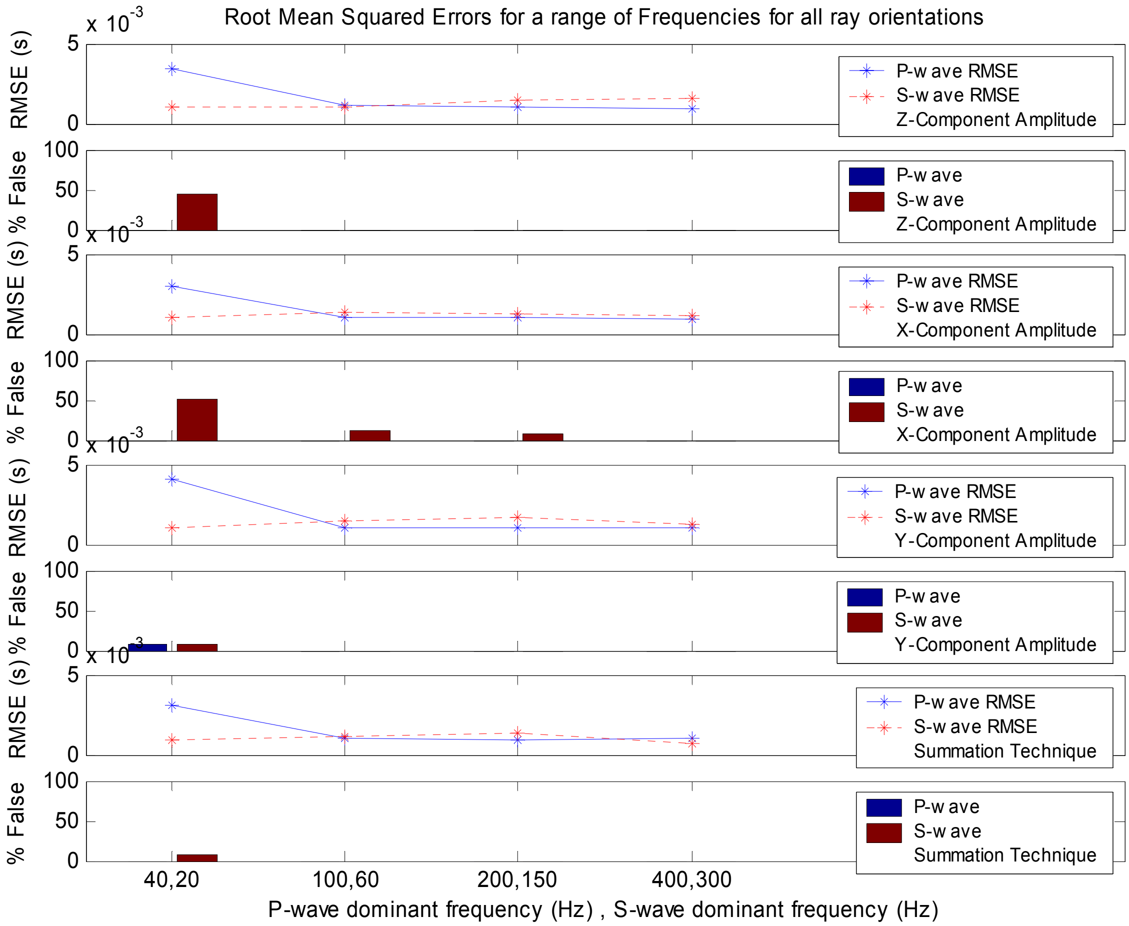

Figure 2-33 RMS errors and percentage of false triggered or undetected events for wave frequencies ranging from 20Hz to 400Hz and an onset time correction applied.

The higher the frequencies the more similar the errors are for the P-and S-waves, at around 1.5ms for all techniques. The P-wave errors were largest for the lowest frequencies. As the frequencies are varied the S-wave is more sensitive to events that are considered undetected or grossly erroneous. This is especially evident on the x-component. The summation technique has the smallest error from the combination of the three-components. Thus, this technique is considered more accurate than the components separately.

Amplitude dependence of Picking

To inspect the outcome of varying the relative amplitudes of the waves, I have attempted the following amplitude relations:

1. $A_P = A_S = 1$
2. $A_P > A_S$
3. $A_P < A_S$
4. $A_P >> A_S$
5. $A_P << A_S$.

The calculations preformed to detect an event and determine its onset time for a P-wave amplitude 25% greater than the S-wave's are illustrated for a wave propagating with an azimuth and an inclination of 30° in Figure 2-34. The overall results for a ray oriented with an azimuth and an inclination ranging from (0 to 90)° and a P-to S-wave relative amplitude ratio ranging from 0.5 to 2 are illustrated in Figure 2-35.

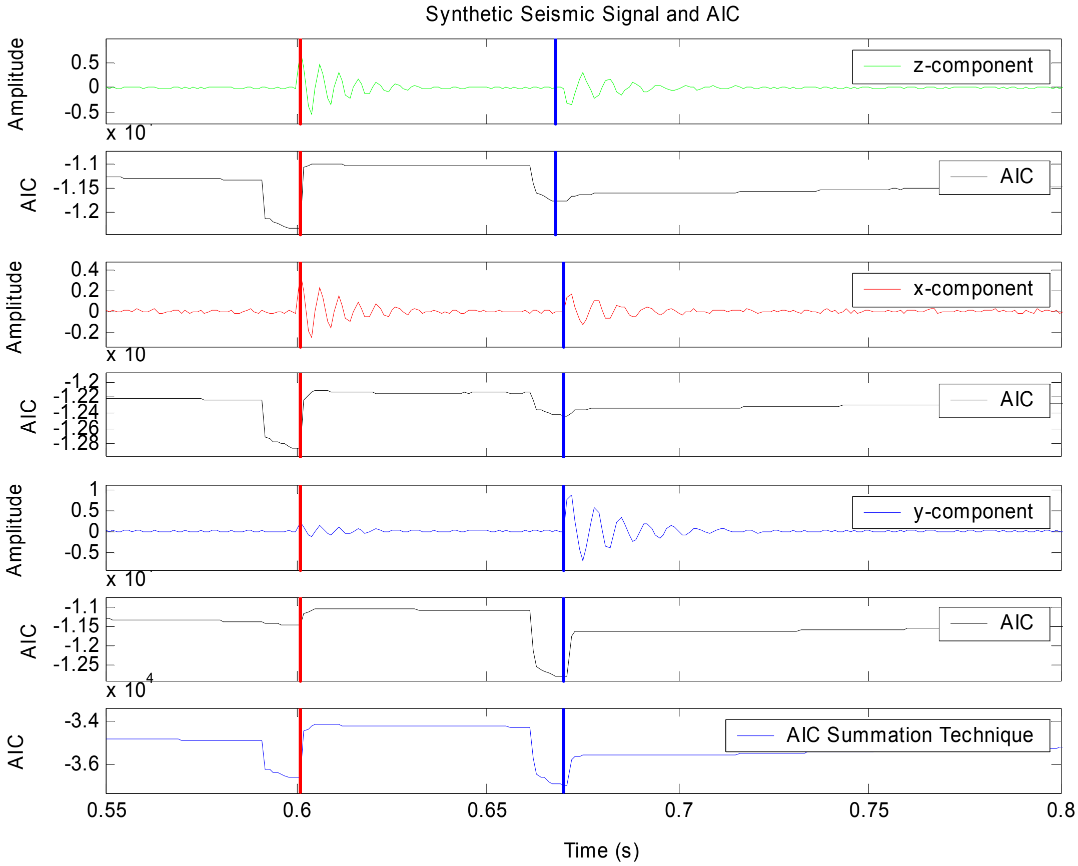

Figure 2-34 top to bottom: Z-component amplitude for synthetic event with an azimuth and an inclination of 30º and a P-wave amplitude that is 25% greater than its S-wave amplitude; AIC for the AR model used above; X-component amplitude.; AIC for the AR model used above; Y-component amplitude; AIC for the AR model used above; AIC summed for all three-components. Red line indicates the detection of the P-wave arrival time. Blue line represents the second event arrival time, corresponding here to the S-wave.

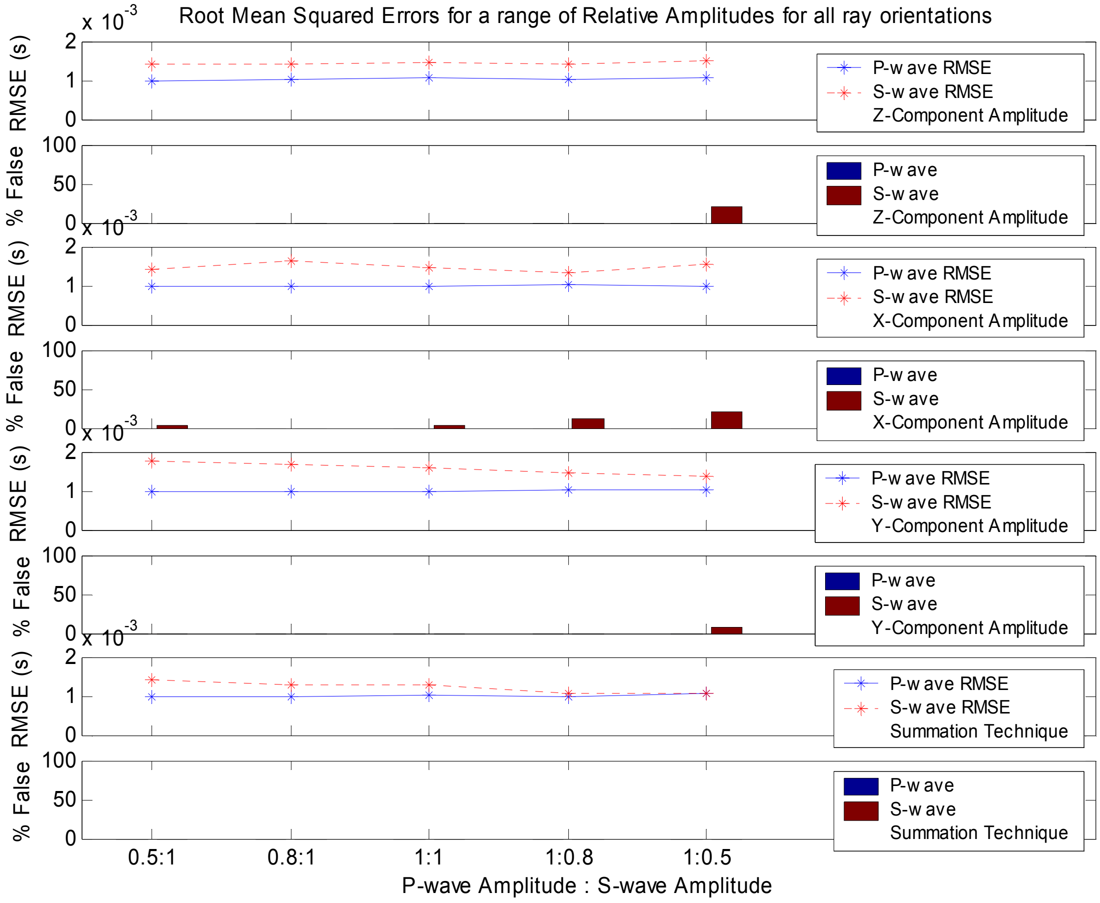

Figure 2-35 RMS errors and percentage of false triggered or undetected events for relative wave amplitudes ratios ranging from 0.5 to 2 with an onset time correction applied.

When varying the relative amplitudes of the wave arrivals the P-wave errors remain fairly constant at around 1ms. The S-wave errors, for the individual components vary between 1.6ms and 1.4ms and always remain larger than the P-waves for all relative amplitudes attempted. The S-wave errors are largest for the summation technique when the amplitude was larger relative to the P-wave's. This contradicts all previous methods errors when the relative amplitudes were varied.

Background Noise Influence on Picking

To inspect the impact of background noise on the onset-time picks and the detection of the P- and S-wave arrivals with the onset time correction applied, I have attempted a variety of SNR's ranging from 1.5 to 10 and have taken background noise off of a recording from geophones situated at Turtle Mt., AB. The standard background noise I have used to alter the SNR is a series of random numbers that are normally distributed, with zero mean.

The calculations preformed in detecting an event and determining its onset time for a signal with a SNR of 3 are illustrated for a wave propagating with an azimuth and an inclination of 30° in Figure 2-36. The overall results for a ray oriented with an azimuth and an inclination ranging from (0-90)° and a random background noise with a SNR ranging from 10 to 1.5 are illustrated in Figure 2-37. I did attempt the same variation of SNR with a random noise that was uniformly distributed, very similar results were found.

The other form of background noise investigated was taken directly from an event at Turtle Mt., AB, on November 13, 2004. The SNR of 100 was amplified to emulate a variety of SNR's. The calculations preformed in detecting an event and determining its onset time for a background noise from Turtle Mt., AB, with a SNR of 3 are illustrated for a wave propagating with an azimuth and an inclination of 30° in Figure 2-38. The overall results for a ray oriented with an azimuth and an inclination ranging from (0-90)° and background noise taken from Turtle Mt., AB, with a SNR ranging from 10 to 1.5 are illustrated in Figure 2-39.

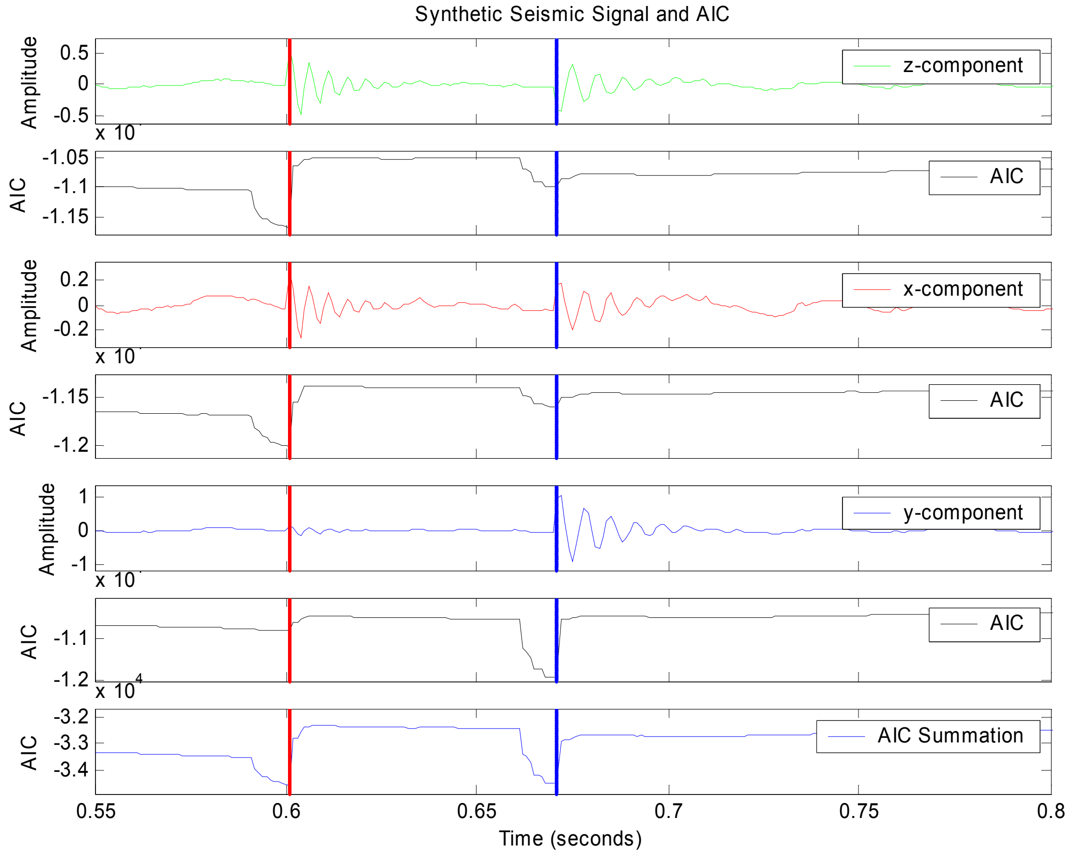

Figure 2-36 top to bottom: Z-component amplitude for synthetic event with an azimuth and an inclination of 30º and a random background noise with a SNR~3; AIC for the AR model used above; X-component amplitude; AIC for the AR model used above; Y-component amplitude; AIC for the AR model used above; AIC summed for all three-components. Red line indicates the detection of the P-wave arrival time. Blue line represents the second event arrival time, corresponding here to the S-wave.

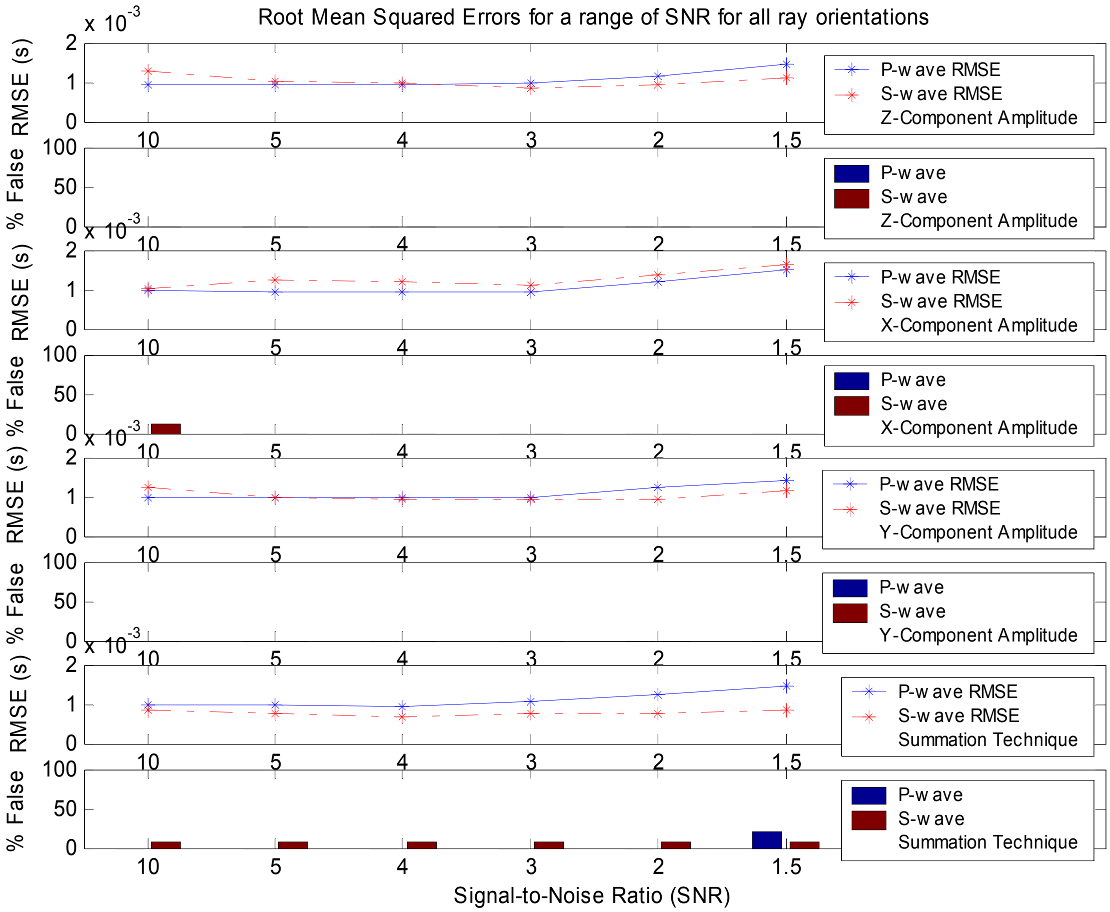

Figure 2-37 RMS errors and percentage of false triggered or undetected events for random background noise with a SNR ranging from 10 to 1.5 with an onset time correction applied.

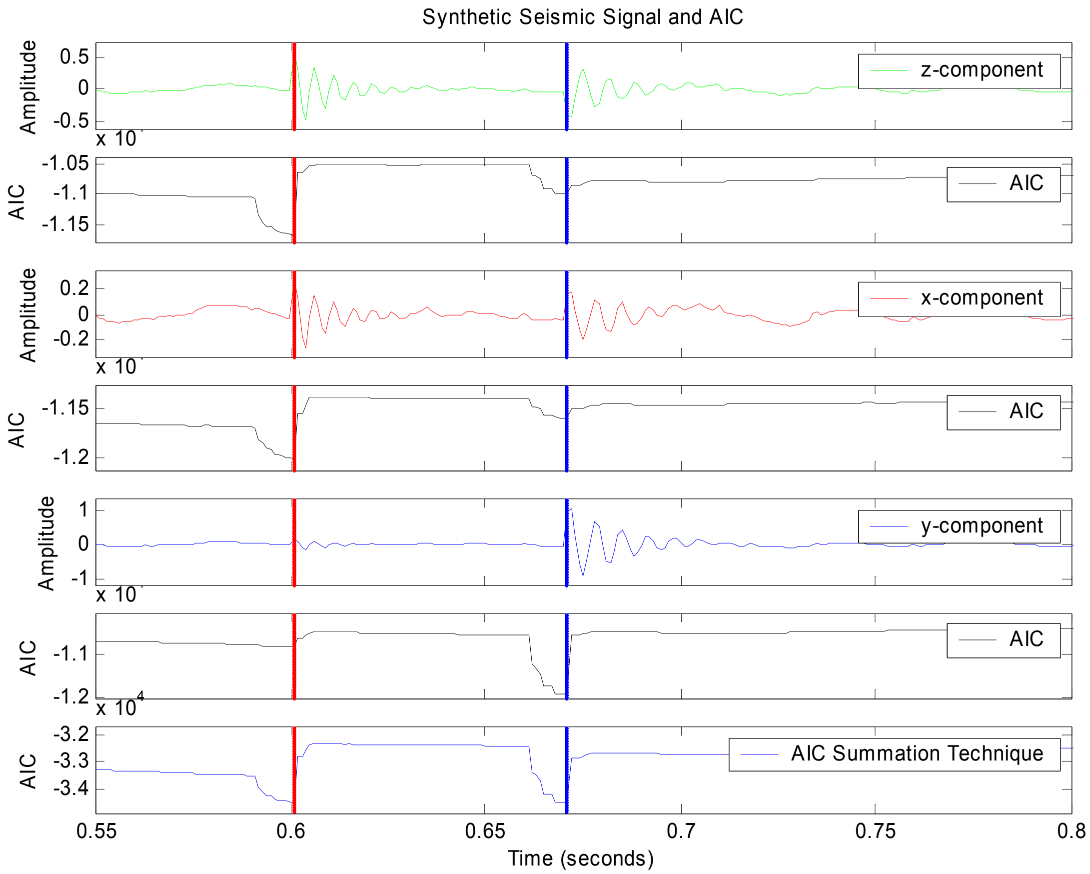

Figure 2-38 top to bottom: Z-component amplitude for synthetic event with an azimuth and an inclination of 30º and with the background noise taken from a microseismic event recorded at Turtle Mt., AB, on November 13, 2004; AIC for the AR model used above; X-component amplitude; AIC for the AR model used above; Y-component amplitude; AIC for the AR model used above; AIC summed for all three-components. Red line indicates the detection of the P-wave arrival time. Blue line represents the second event arrival time, corresponding here to the S-wave.

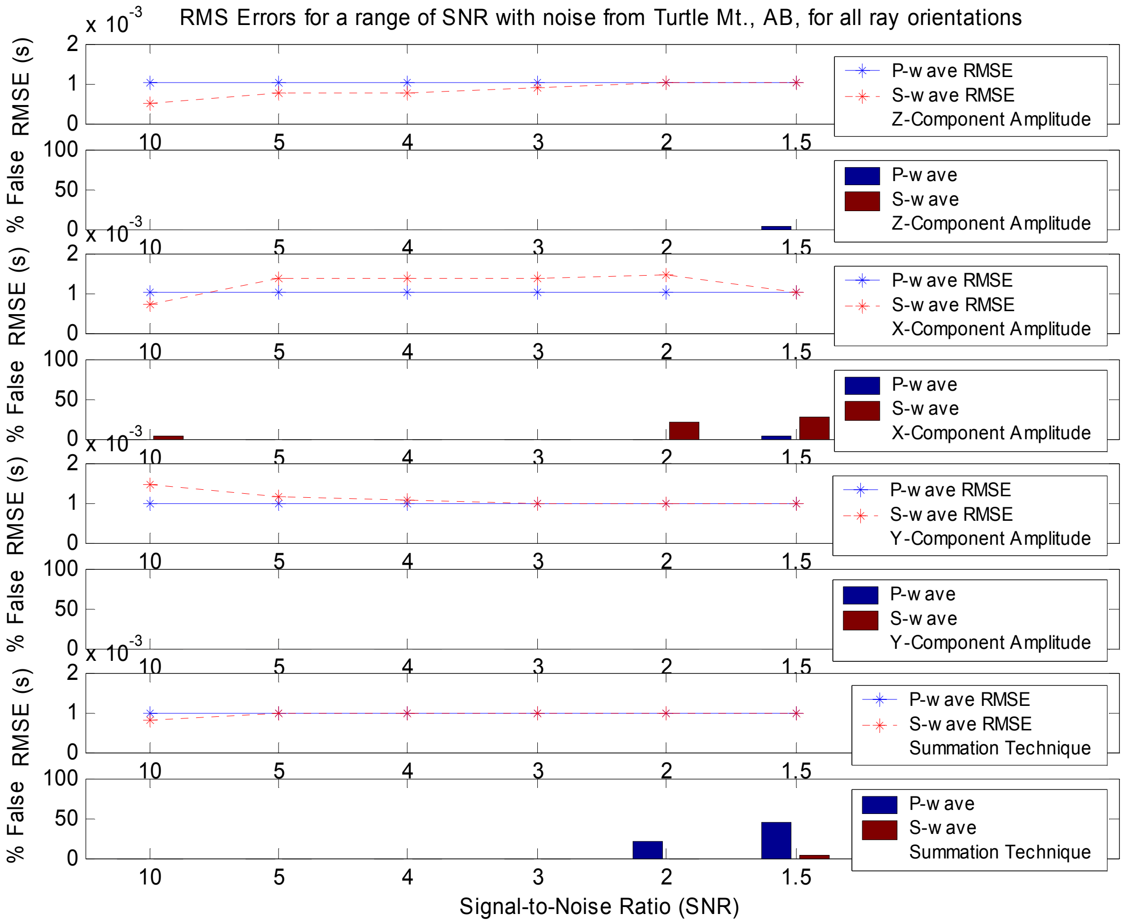

Figure 2-39 RMS errors and percentage of false triggered or undetected events for background noise taken from Turtle Mt., AB, with a SNR ranging from 10 to 1.5 and an onset time correction applied.

As the SNR of the random background noise was decreased the S-wave errors increased slightly from 0.8ms to a maximum of 1.8ms on the summation and x-component amplitude techniques, see Figure 2-37. While for the z- and y-component amplitude techniques the S-wave errors fluctuated between 1.3ms and 1ms as the SNR was reduced. The P-wave errors remained constant at around 1ms on all the functions as the SNR was reduced with the exception of an SNR of 1.5, where it slightly increased. The number of undetected or grossly erroneous triggers for the P-and S-wave was tremendously different from previous methods; see Figure 2-11 and Figure 2-25. It was found that almost none of the P-waves went undetected or were grossly erroneous as the SNR was diminished to 1.5. Similar results are seen for the S-wave, with the exception of the x-component function, where it had a slight percentage of error that was less than 10 percent and the summation technique where a 5 percent error was read for all SNR. These errors did not increase in accordance with the SNR reduction. The striking characteristic of this AR-AIC technique is that the percentages of P-and S-waves that are undetected or grossly erroneous appear to be non-existent with the exceptions that were noted, despite the diminishing SNR.

When the background noise was taken directly from a microseismic event recorded at Turtle Mt., AB, the S-wave picking errors were slightly affected as the SNR was decreased, see Figure 2-39. The P-wave errors remained constant at about 1ms on all the functions as the SNR was reduced. As the SNR was decreased the percentage of undetected or erroneous events for the P-wave increased slightly when the SNR was between 2 and 1.5 for the summation function. The S-wave's percentage of false detections increased when the SNR was between 2 and 1.5 on the x-component function.

From the AR-AIC's response to varying frequencies, relative amplitudes and background noise's it can be seen that the summation function produces smaller errors for both wave arrivals compared to the individual component functions.

P-and S-wave arrival time interval's influence on the picking

Using synthetic data with known arrival times, I investigate how the AR-AIC technique responds to a decrease in the time interval between the arrival of the primary and secondary waves. Time intervals examined are 70ms, 30ms, 25ms, 20ms, 15ms and 10ms. These will illustrate the limitations of the AR-AIC technique to resolve the S-wave arrival from the P-wave coda. Notice that the time interval used for the ‘standard’ synthetic model is taken to be 0.070s.

Figure 2-40 illustrates the summation technique calculations for the AR-AIC. Results are displayed for the z-component of this signal for arrival time intervals of 15ms and 10ms. Figure 2-41 displays the percentage of undetected or vastly erroneous events that result when the time intervals is between 70ms and 10ms. It is important to emphasize that as a result of the ray orientations examined the maximum percentage of undetected events for the 3-component magnitude calculations, as well as the summation technique are not always 100%. This is because specific ray orientations have only one wave arrival that can be detected. Possible values are displayed in Figure 2-42.

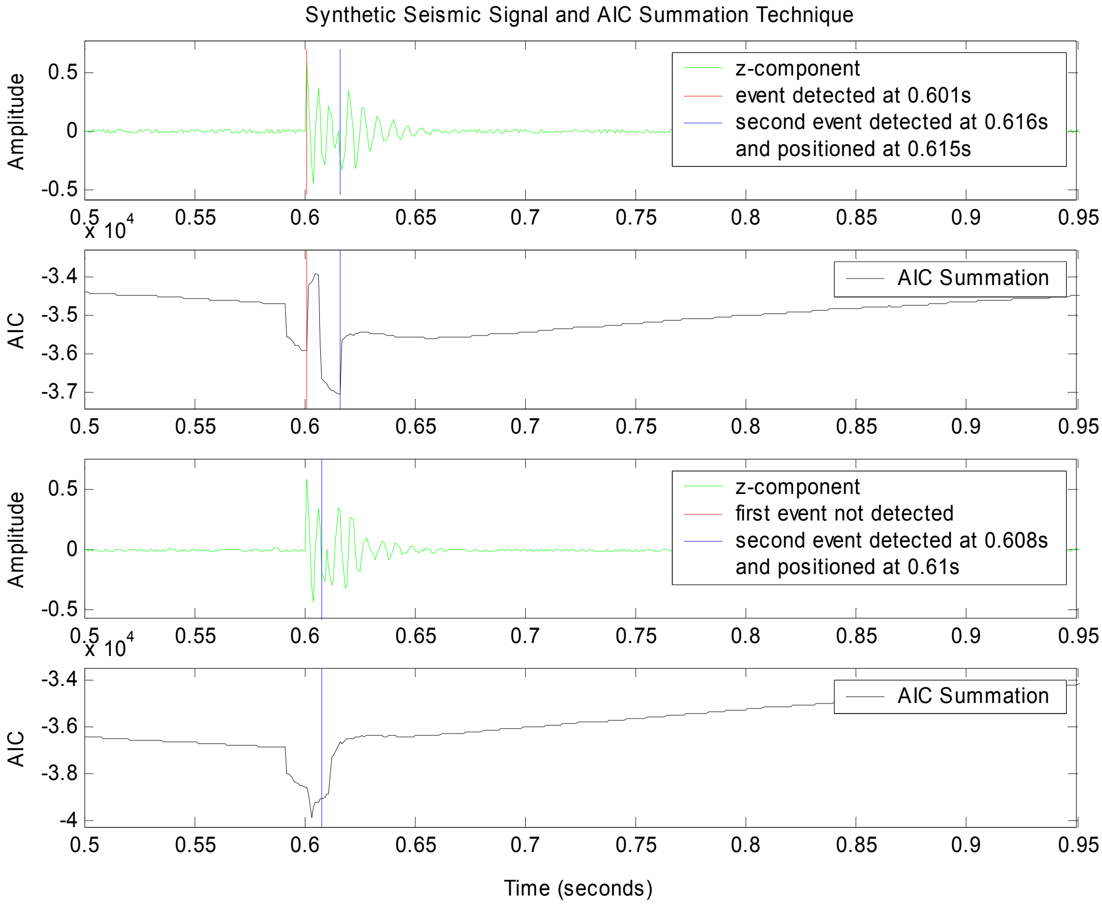

Figure 2-40 top to bottom: Z-component amplitude for synthetic event with an azimuth and an inclination of 30° and an arrival time interval of 15ms; AIC Summation results; Z-component amplitude for synthetic event with an azimuth and an inclination of 30° and an arrival time interval of 10ms; AIC Summation results. Red line indicates the detection of the P-wave arrival time. Blue line represents the second event arrival time, corresponding here to the S-wave.

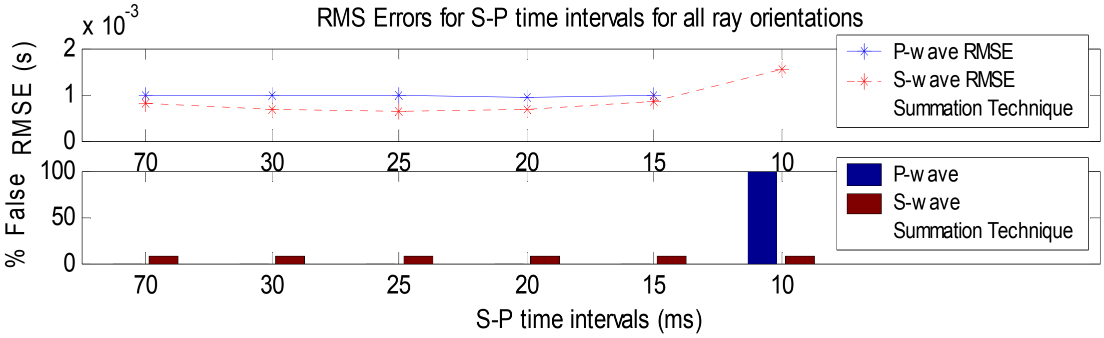

Figure 2-41 RMS errors and percentage of false triggered or undetected events for an arrival time interval ranging from 70ms to 10ms.

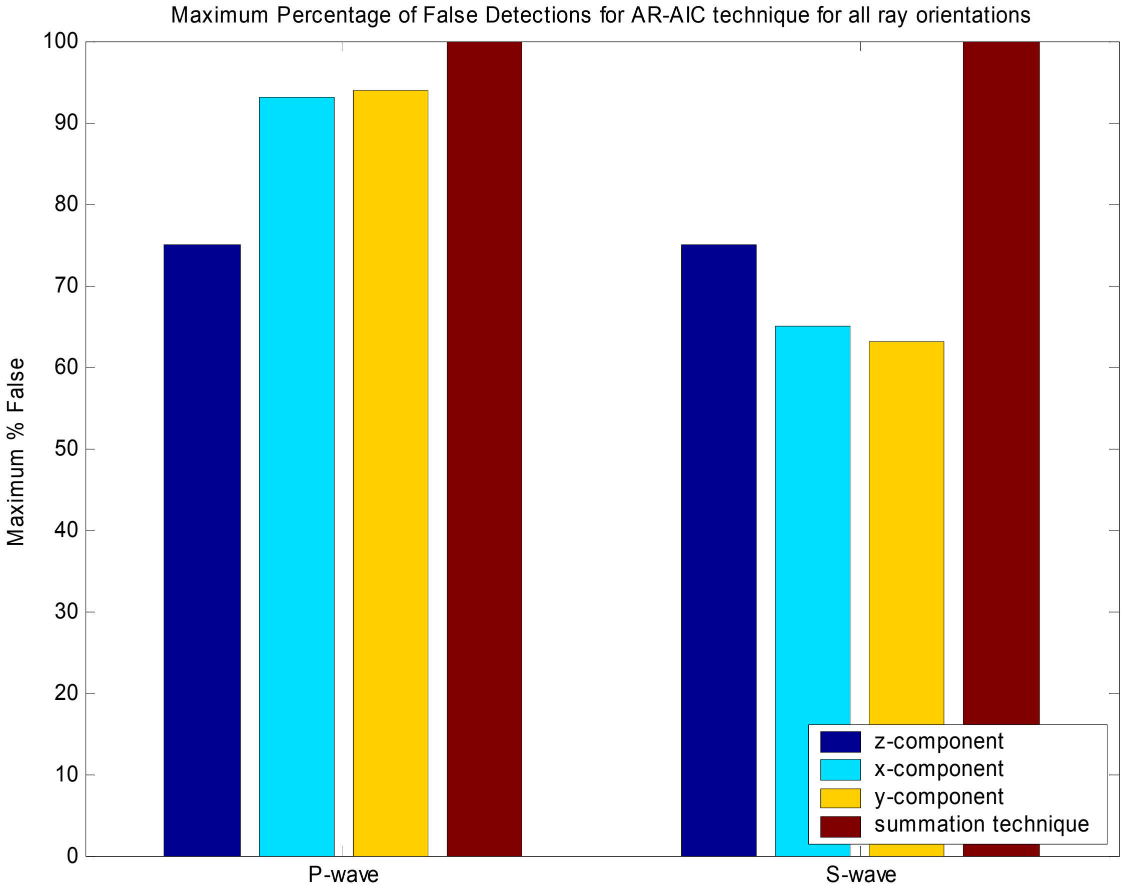

Figure 2-42 Maximum possible percentage of false detections for the AR-AIC technique.

Figure 2-40 illustrates the key restrictive calculations in detecting the arrivals of two distinct seismic events for the AR-AIC method. For the 3-C technique when the time interval is between 15ms and 10ms, the two distinct minimum pedestals merge for the summation of the AIC's. Programming limitations result in the global minimum AIC not being selected when the arrival time interval is less than 15ms. This is why the P-wave is labelled as being undetected in Figure 2-40 and Figure 2-41. In reality the S-waves should have been undetected.

From Figure 2-41 it can be seen that for all ray orientations the summation technique loses the ability to distinguish the P-and S-wave arrivals when the arrival interval is forced to 10ms. Thus, the minimum time interval for which the S-wave can be resolved from the P-wave coda is between 15ms and 10ms, since the summation technique is considered superior to the individual component methods. The onset picking errors for the S-wave fluctuate as the arrival time interval is reduced from 70ms to 10ms for all functions, however, the P-wave remains constant at 1ms. Programming limitations do not allow the reduction of the arrival time interval beyond 10ms.

S-Transform Technique

2.4.3 S-Transform Technique Theory

Using the generalized S-transform it is possible to identify the arrival time of a wave from a seismogram that is severely contaminated with noises by analyzing the time-frequency content. Pinnegar and Manshina (2003) have proposed a generalized S-transform that may improve the resolution of the onset times of seismic events. The S-transform is a blend of the wavelet transform and the short-time Fourier transform and is invertible (Pinnegar and Manshina, 2003). This spectral localization technique is discussed further by Pinnegar and Manshina (2003).

The S-transform is performed on the total energy function defined in section 2.3.1. Figure 2-43 illustrates the seismic traces, their energy function and its S-transform.

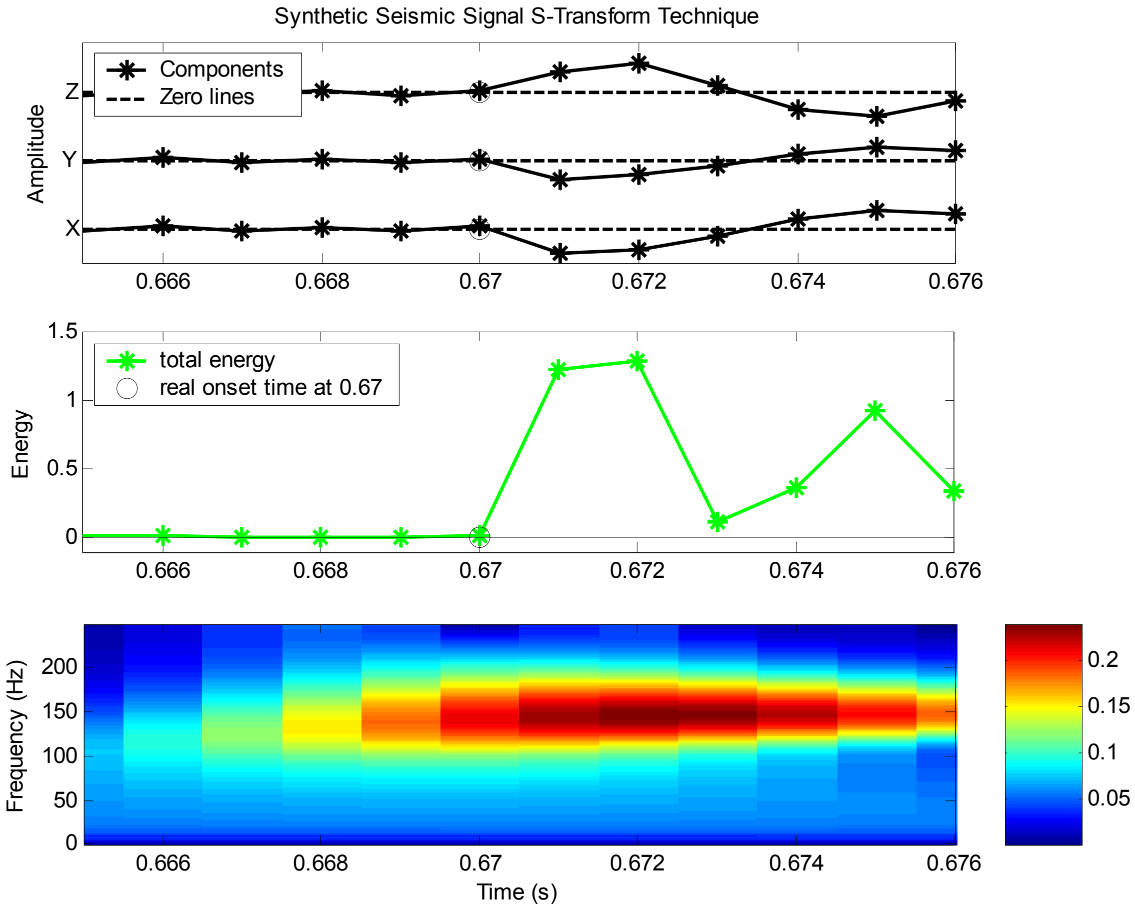

Figure 2-43 Schematic diagram illustrating computations performed on data to reach S-Transform.

A user-defined threshold must be surpassed to detect an event. Figure 2-44 portrays the S-transform from Figure 2-43 and its threshold. Here I use a threshold that is one-third of the maximum value of the S-transform at a specified time and frequency region. This threshold value will change throughout this study to better resolve the arrival times.

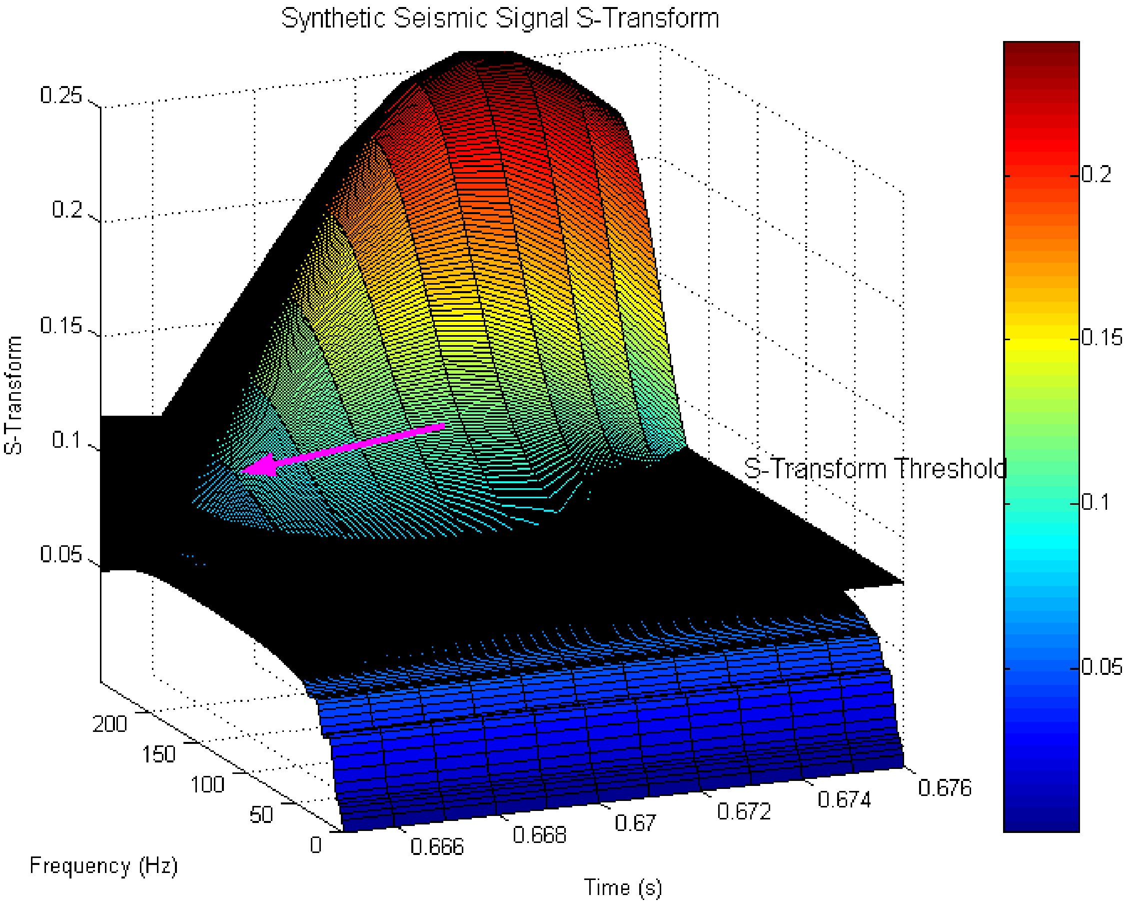

Figure 2-44 S-transform for the synthetic seismic event shown in Figure 2-43. Note that the black surface is the S-transform threshold and the purple arrow indicates region where it is surpassed.

The steps performed in this S-transform technique are expressed in Figure 2-45. First, the energy of the 3-components is resolved and then its S-transform is computed. A threshold then must be surpassed by the S-transform to trigger the method; the maximum of the S-transform is taken within a window along the frequency value, which initially surpassed the threshold at this specific trigger time. Figure 2-45 illustrates how the S-transform function begins to raise prior to the true onset-time, thus the onset-time correction used previously is not applicable. As well, the S-transform reaches its maximum amplitude after the true onset-time, however at that value the corresponding time is closer to the true onset-time than the trigger time. Thus I take this time as the maximum S-transform corrected onset-time (MOC).

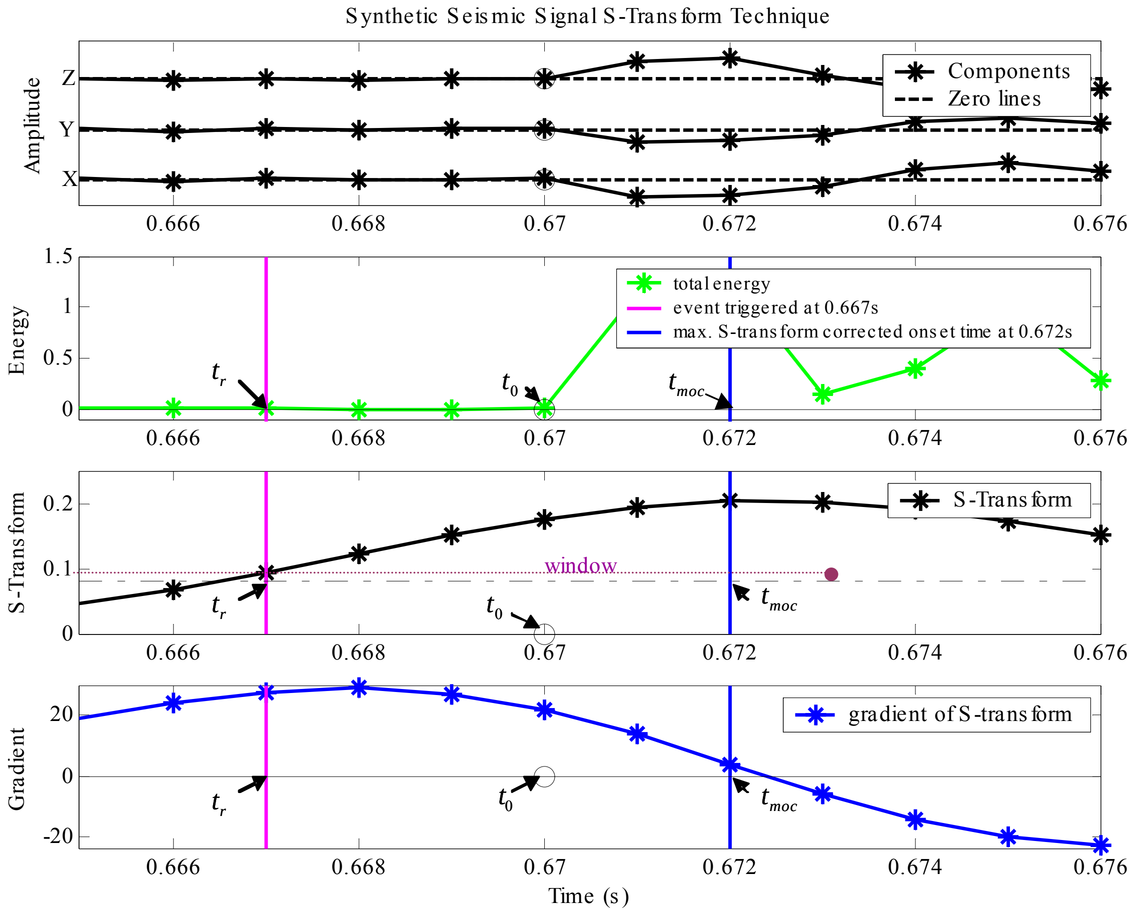

Figure 2-45 Schematic diagram showing the steps performed for the S-transform technique.

2.4.4 S-Transform Technique Analysis using Synthetic Data

Using the synthetic microseismic events depicted in previous sections I aim to support a simplistic evaluation of this S-transform technique for picking events. Calgary Scientific has executed an S-transform on the total energy of my synthetic 3-component signals generated using an azimuth and an inclination of 30º. Using a pre-defined threshold level for the amplitude of the S-transform and a maximum S-transform onset-time correction, the arrival time of the P-and S-waves are resolved.

The value of SNR is altered using the standard synthetic model. Unlike my previous analyzes, these calculations are not performed over one hundred iterations to remove the possible influence of the random background noise.

To inspect the impact of background noise on onset-time picking and detection of P- and S-wave arrivals, I have attempted a variety of SNR's ranging from 1.5 to 10. The standard background noise I have chosen is a series of random numbers that are normally distributed, with zero mean. The S-transform for a background noise that constitutes a SNR of 3 is illustrated for a wave propagating with an azimuth and an inclination of 30° in Figure 2-46. The results for a ray oriented with an azimuth and an inclination of 30° and a random background noise with a SNR ranging from 10 to 1.5 are illustrated in Figure 2-47.

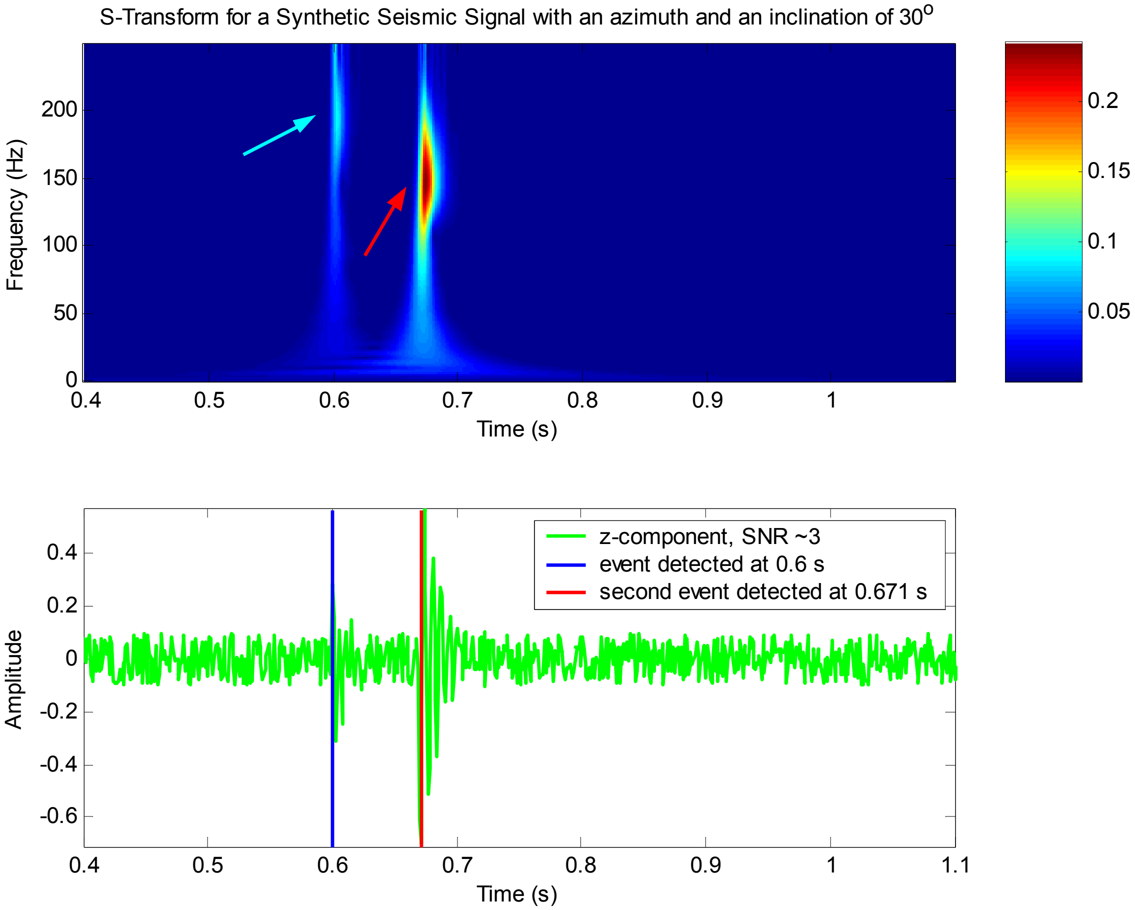

Figure 2-46 top to bottom: S-transform of total energy for synthetic event with an azimuth and inclination of 30° and a SNR of 3. Blue and red arrows represent the P- and S-wave arrivals; Arrival time picks for P-and S-wave generated from above, displayed on the z-component. Blue and red lines represent the P-and S-wave arrival picks.

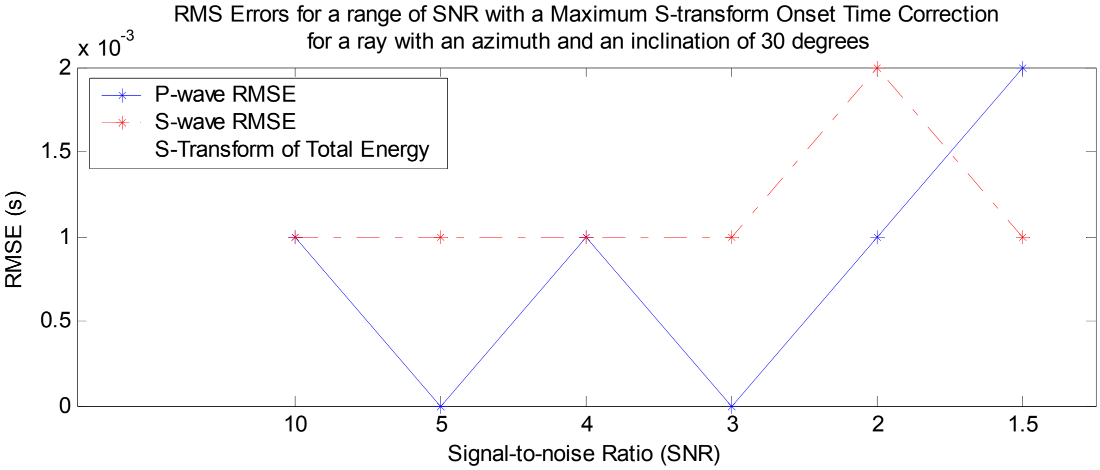

Figure 2-47 RMS errors for random background noise with a SNR ranging from 10 to 1.5.

Figure 2-46 illustrates the S-transforms response to the arrival of two separate waves. As the random background SNR was decreased from 10 to 2, the P-wave errors fluctuated between 1ms and 0ms. For a SNR of 1.5 the P-wave error increased to 2ms for the total energy of the signal oriented with an azimuth and inclination of 30º, see Figure 2-47. The S-wave RMS errors were constant at 1ms for a SNR of 10 to 3, then rose to 2ms and fell down to 1ms as the SNR was further reduced to 1.5. It is important to note that the corrected onset-time for this technique can only resolve time to the nearest millisecond. Although the errors for both waves are fairly large ranging between at 0ms and 2ms, it is a preliminary development to the capabilities of the S-transform; thus, showing the potential of S-transforms for seismic event detection.

2.5 Synthetic Analysis Conclusions

Using synthetic signals, I was able to determine the effectiveness of the energy techniques, multi-window amplitude techniques, AR-AIC techniques, and S-transform techniques at detecting P-and S-wave arrivals.

Comparing two energy techniques that both use the STA threshold; one with the onset-time correction and one without, I found the overall errors to decrease with the application of the onset-time correction. This is especially evident for the S-wave's error, which was reduced by at least half. The number of events undetected or grossly erroneous remained the same despite the onset-time correction with the exception of the lowest frequencies of 40Hz and 20Hz for the P-and S-waves, respectively. It is important to notice that the percentage of undetected events as the SNR was reduced using a background noise taken from Turtle Mt., AB, appeared to be quite large, despite the onset-time corrections. Therefore, the energy technique may not be suitable for the detection of events in low SNR environments.

In general, when contrasting the energy technique with an onset-time correction to the multi-window amplitude technique the picking errors were found to be lowered by an order of magnitude for frequencies larger than 40Hz, and 20Hz, for the P-and S-waves, respectively. As well, the volume of undetected or erroneous events was found to be larger for the multi-window technique as the SNR was decreased using a random background noise; yet, when using a background noise from Turtle Mt., AB, the amount for the P-wave is very similar and the S-wave is much lower. Thus, the SNR that the multi-window technique is applicable for is not clearly resolved. The multi-window technique was found to resolve the S-wave from the P-wave coda past the arrival time interval of 25ms to 20ms, where the energy technique was unsuccessful. However, caution should be taken when applying the multi-window technique to an environment where the S-wave amplitude is not greater than the P-wave's.

Overall, the AR-AIC technique had picking errors an order of magnitude greater than the multi-window technique. The numbers of undetected or erroneous events for the AR-AIC technique were found to severely diminish in comparison to the multi-technique. Consequently, the AR-AIC technique was determined to be the most suitable for all SNR environments. The AR-AIC method was also found to resolve the S-wave arrival from the P-wave coda to within an arrival time interval of 15ms to 10ms. Thus, this technique would provide more stability in resolving a smaller arrival time interval for all SNR environments and even when the S-wave's amplitude is less than the P-wave's amplitude.

Preliminary results from the application of the S-transform to the total energy of a 3-C seismic signal are insightful. Despite the S-transform's results having an error that was an order of magnitude larger than the multi-window technique it was satisfying to see that the errors were minimally influenced by the reduction of the SNR, unlike some of the other detection algorithms previously attempted.

In summary, there appears to be a trade-off between the accuracy of the onset-time picking and the volume of events correctly detected. If one were most concerned with the detection of events, in particular for a sufficiently low SNR environment then the application of an initial trigger program and then the AR-AIC technique would be appropriate. However, if the exactness of the onset-time pick is of utmost importance, perhaps because the accuracy of the hypocenter is of significance, then the multi-window amplitude technique would be more fitting. As well, it is important to have prior knowledge of the distance range between possible microseismic events and the distance between receivers, since the minimum arrival time interval for the resolution of both waves varies between methods.

CHAPTER THREE: Case Study I: Turtle Mt., Alberta

3.1 Introduction to the Frank Slide at Turtle Mt., Alberta

On the morning of April 29th, 1903, a slab of limestone weighing 70,000,000 tons fell down from Turtle Mountain killing approximately 70 people and destroying the town of Frank in the Crowsnest Pass of south-western Alberta (Bingham, 1996). Coal mining in the mountain was initially blamed for the catastrophe, but further investigation revealed a strong relationship of the pre-existing geological structure of the mountain to its innate instability (McConnell and Brock, 1904; Daly et al., 1912; Allan, 1933; Jones, 1993). Figure 3-1 illustrates the state of Turtle Mt. around August 2004.

Figure 3-1 The Frank Slide at Turtle Mt, AB viewed from the southeast. The light-coloured vertical streak near the north summit (on the right of the cliff face) illustrates current rockfall activities (Stewart et al., 2004).

3.2 Geology of Turtle Mt., Alberta

The mountain consists of layers of limestone, conglomerate, sandstone, shale, and coal; that have been pushed from the west and consequently folded to form an anticline. This westward force has continued to create a fault, the Turtle Mountain Thrust Fault, under the fold (Field and McIntyre, 2003). Figure 3-2 displays the Turtle Mt., Alberta, regional geology, and the location of two cross-sections, which are depicted in Figure 3-3. Geologists pinpointed this unstable structure of the mountain to be the primary cause of the Frank Slide (Field and McIntyre, 2003). Coal mining and the threat of gas extraction in the nearby valley provide ongoing concern to the communities in the Crowsnest area. A seismic monitoring system has been constructed on Turtle Mountain by the University of Calgary (Stewart et al., 2004). Assessment of such a monitoring system in this region could provide the predecessor for a warning system for a rockslide event.

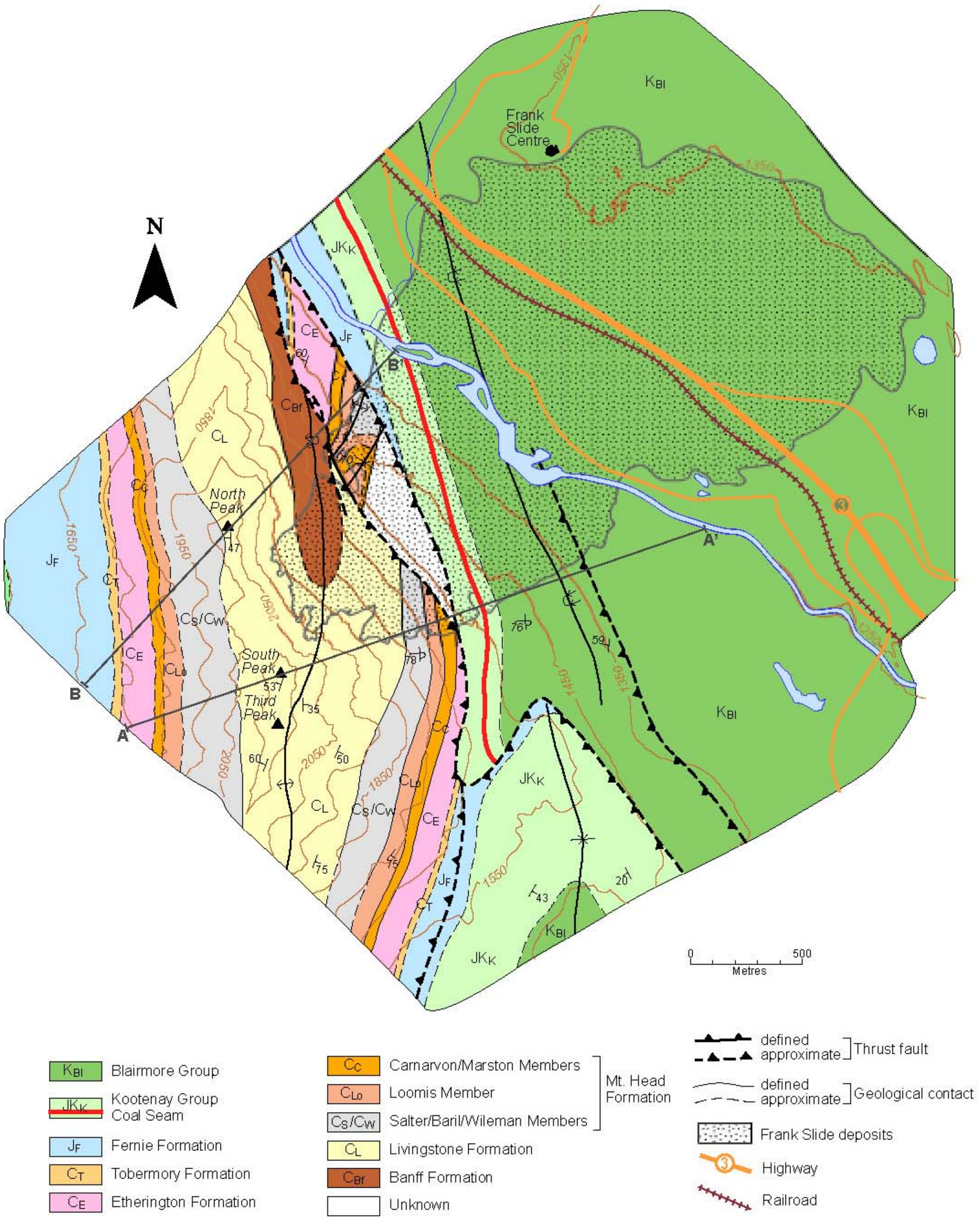

Figure 3-2 Turtle Mt., Alberta geology map (Langenberg et al., 2005)

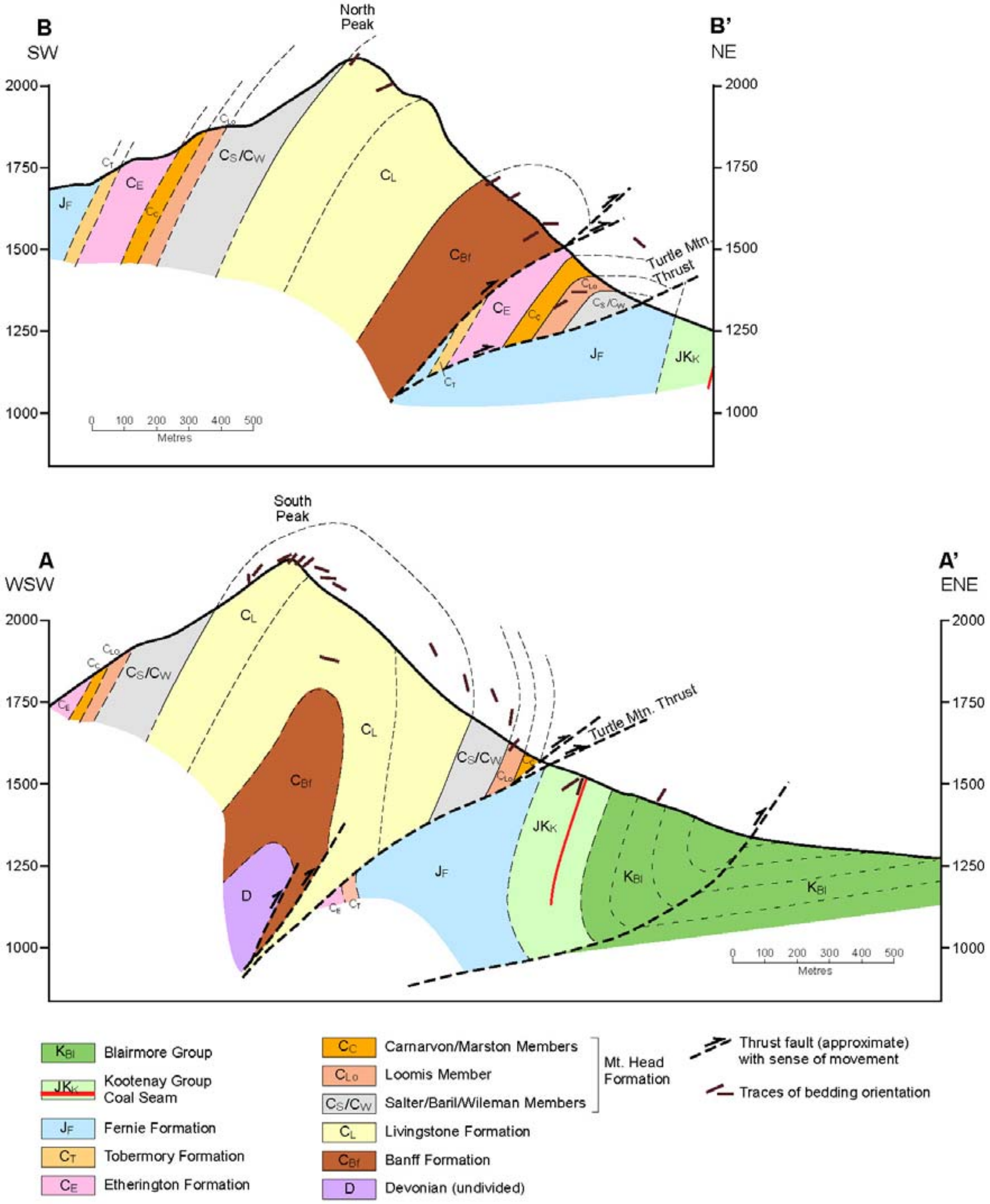

Figure 3-3 Cross-sections B-B' and A-A' showing geology of Turtle Mt., Alberta (Langenberg et al., 2005).

Limestone samples collected by Stewart et al. (2004) were found to have an average P-wave velocity of 5340m/s and an average S-wave velocity of 2794m/s, and a resultant Vp/Vs value of 1.91. Stewart et al. (2004) attribute their higher P-wave velocity to their unfractured samples. Stewart et al. (2004) also made measurements on coal samples and found the average P-and S-wave velocities to be 2497m/s and 1145m/s, respectively, giving a higher Vp/Vs value of 2.18.

3.3 Turtle Mt., Alberta Seismic Network

During 2004, six stations each consisting of one 3-component 28 Hz seismometers, with 1ms sampling were deployed throughout the mountain region (Stewart et al., 2004). Figure 3-4 illustrates the locations of the six stations labelled South Peak, Third Peak, Ridge, Relay, Pit and River, along with the location of the Frank Slide Interpretive Centre (FSIC).

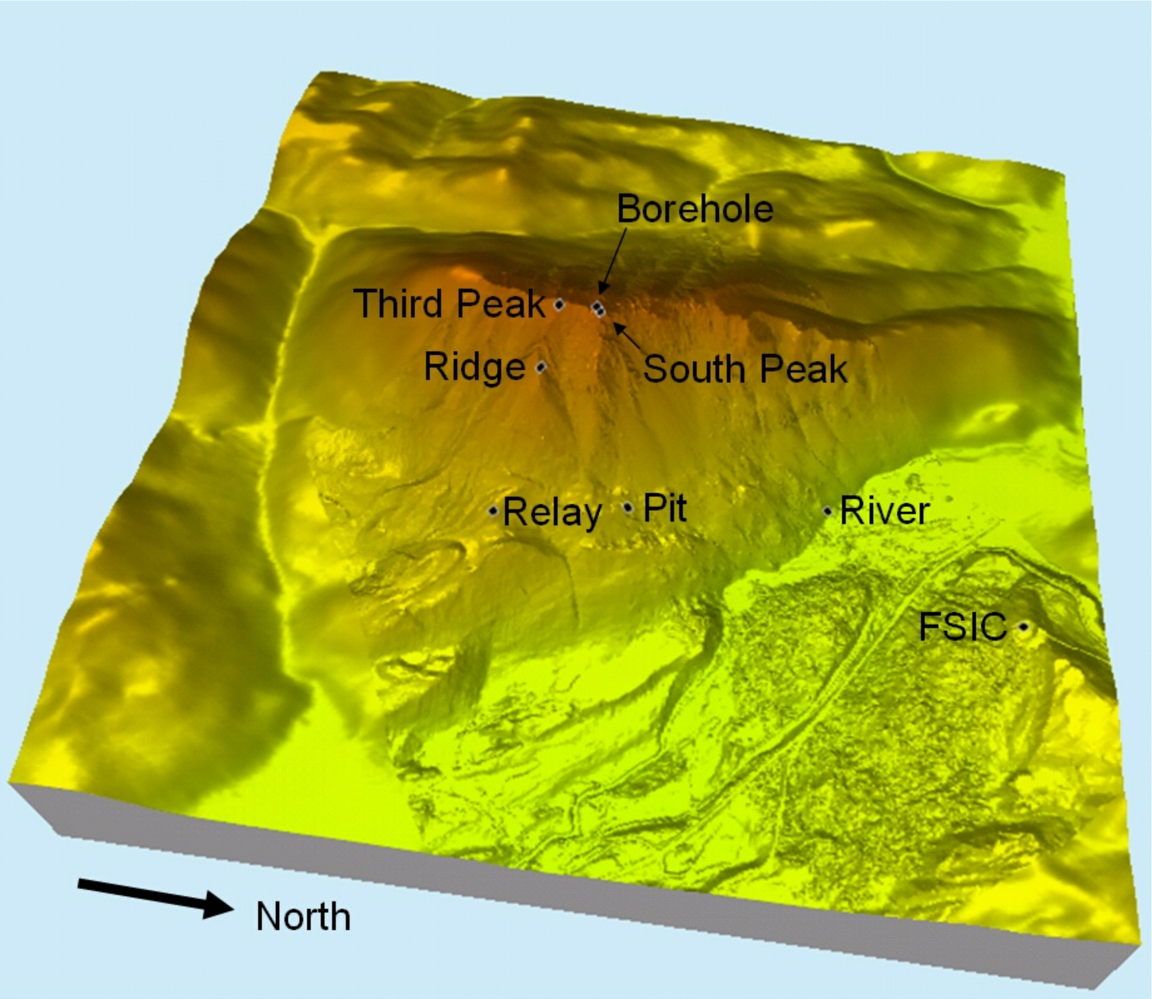

Figure 3-4 3-D view of Turtle Mt., AB looking west-southwest. The locations of the 6 Stations are labelled along with the Frank Slide Interpretive Centre (FSIC) and the borehole where geophones are also located. (Courtesy of Henry Bland)

3.4 Description of Turtle Mt. data

Data recorded by the University of Calgary using 3-C seismometers positioned on Turtle Mt. at six stations will be analyzed using the methods discussed in Chapter 2, excluding the energy technique without an onset-time correction applied. Figure 3-5 displays the seismic event recorded on 5 of the 6 stations on December 9th, 2004 at Turtle Mt., AB. From Figure 3-5 it can be seen that the P-wave arrival is somewhat difficult to pick on most of the stations as the event is emergent. An emergent event is articulated as when the initial arrival of the seismic event is hidden within the background noise and the seismic event must emerge to greater amplitudes to even be identified. As well, the S-wave arrival is not distinguishable at all from the P-wave coda on any of the stations. Thus, in this work I will be focusing on the detection of the P-wave arrival only.

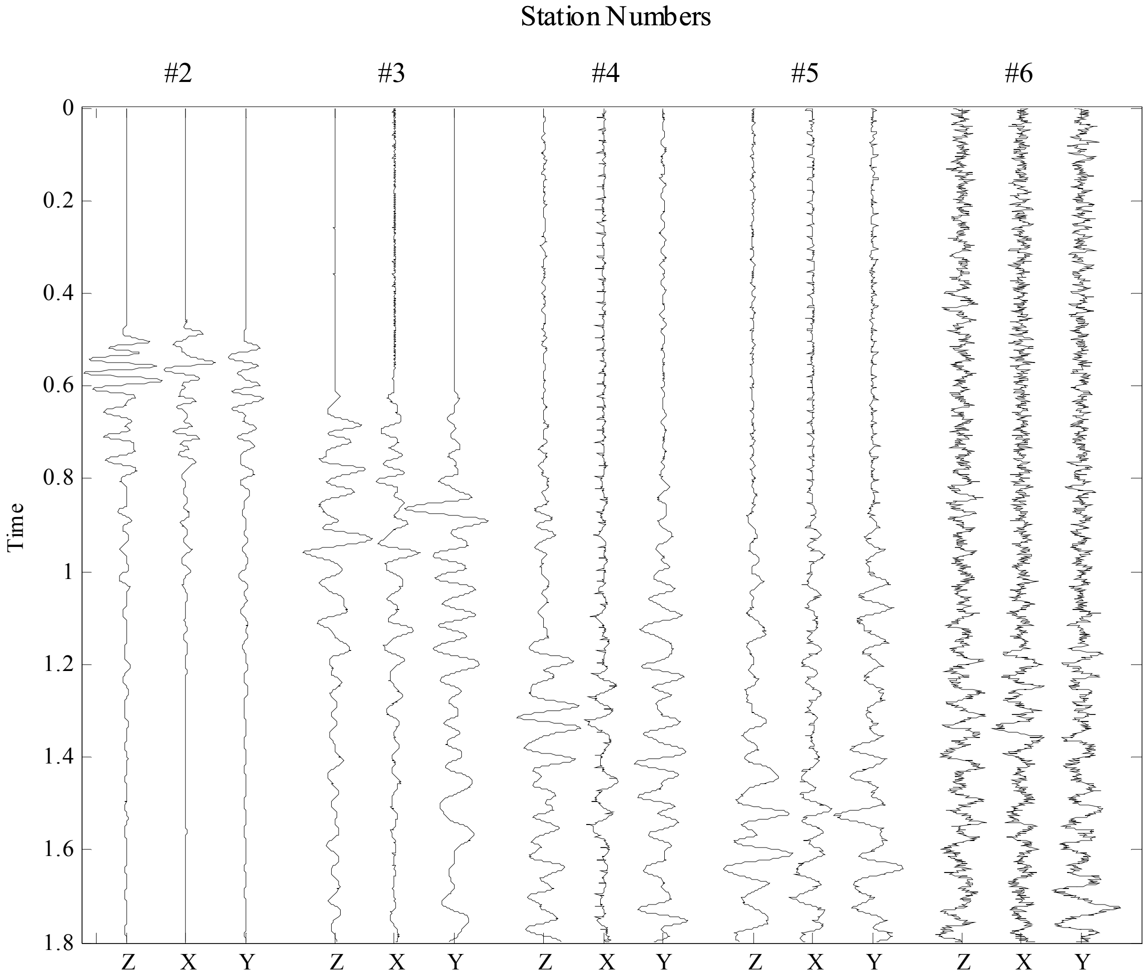

Figure 3-5 Data recorded at Turtle Mt., AB during a seismic event on December 9th, 2004 with various amplitude gain applied.

3.5 Analysis of data from Turtle Mt., Alberta

To investigate the detection and picking methods interrogated in chapter 2, I have applied them to data acquired by the University of Calgary at Turtle Mt., Alberta. Figure

3-6 displays the total energy of the 3-C recordings at all five stations for a microseismic event, along with my manual picks for the arrival of the P-waves.

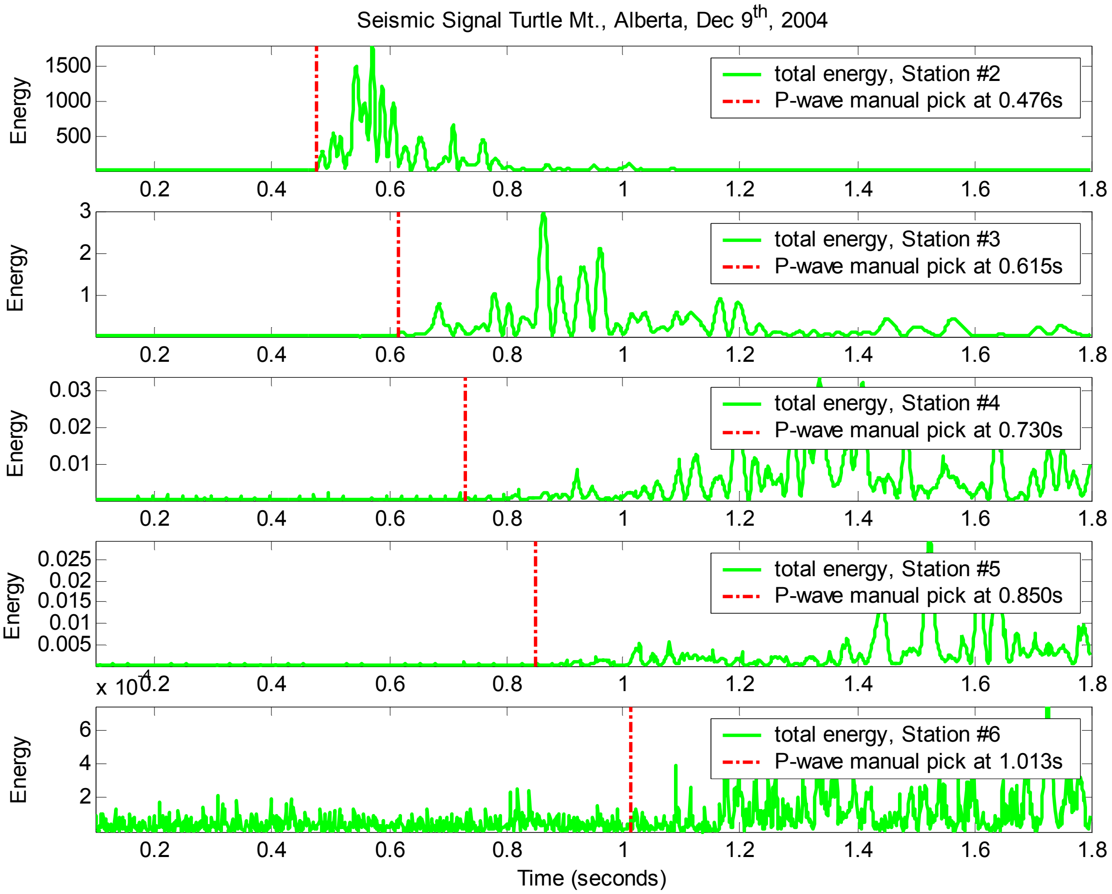

Figure 3-6 Total energy on stations #2 through #6. Red line indicates the first P-wave arrival time picked manually.

Here, I employ the energy technique with an onset-time correction applied. I use only the total energy of the 3-C seismic record, as it was shown previously to be the most robust energy technique in Chapter 2. As well, I apply the multi-window technique, using the 3-C magnitude function; the AR-AIC technique using the summation of the AIC's for all 3-components; and finally, the S-transform technique applied to the total energy of the 3-C signals.

3.5.1 Energy Technique

To determine the detection and arrival times for the data acquired at Turtle Mt., Alberta, I utilize the energy technique with an onset-time correction applied to the total energy of the 3-C seismic record. The results from the energy technique are displayed in Figure 3-7 and Figure 3-8. The RMS errors associated with the picks for all stations are displayed in Figure 3-9. The RMS errors associated with the picks for station #2 are displayed for comparison with the other techniques in Figure 3-19.

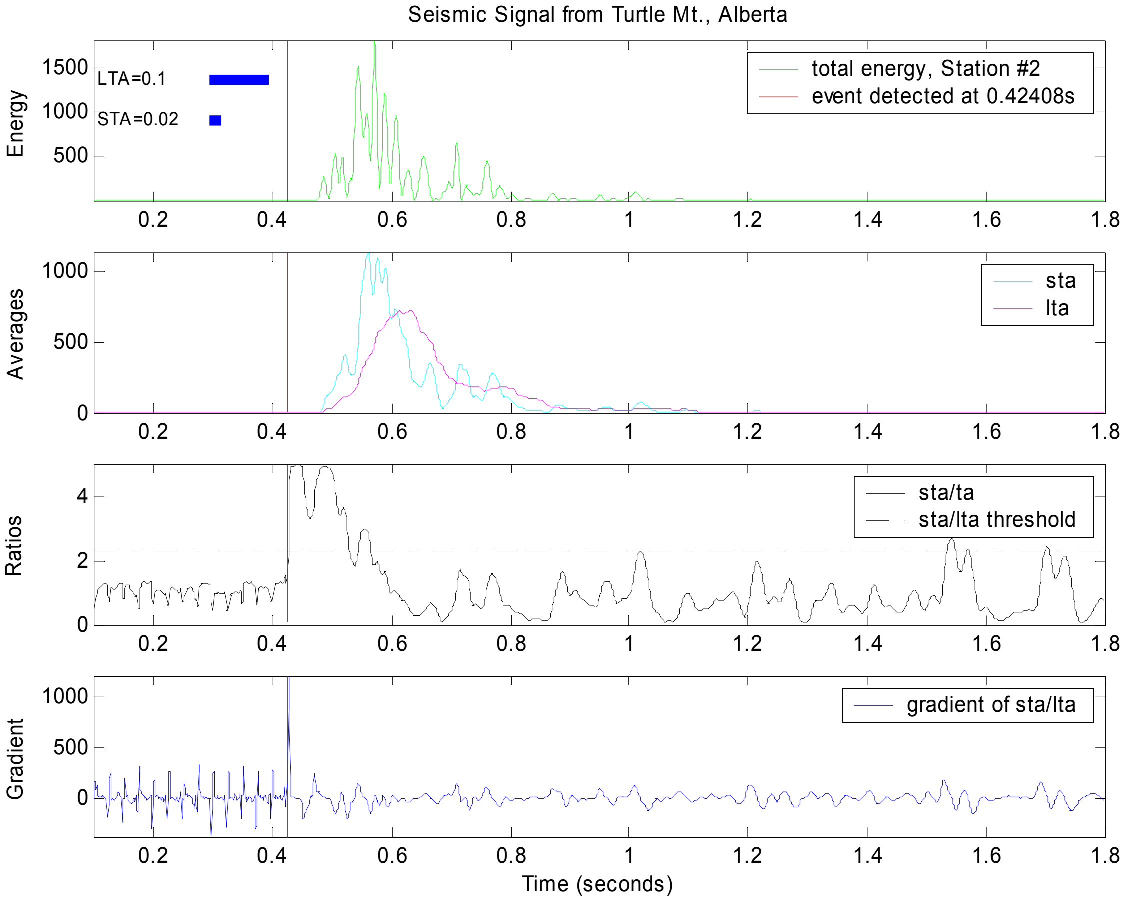

Figure 3-7 Total energy on station #2; STA and LTA; STA/LTA; Gradient of the STA/LTA. Red line indicates the first P-wave arrival time picked with the STA threshold of 0.02 and STA/LTA threshold of 2.3.

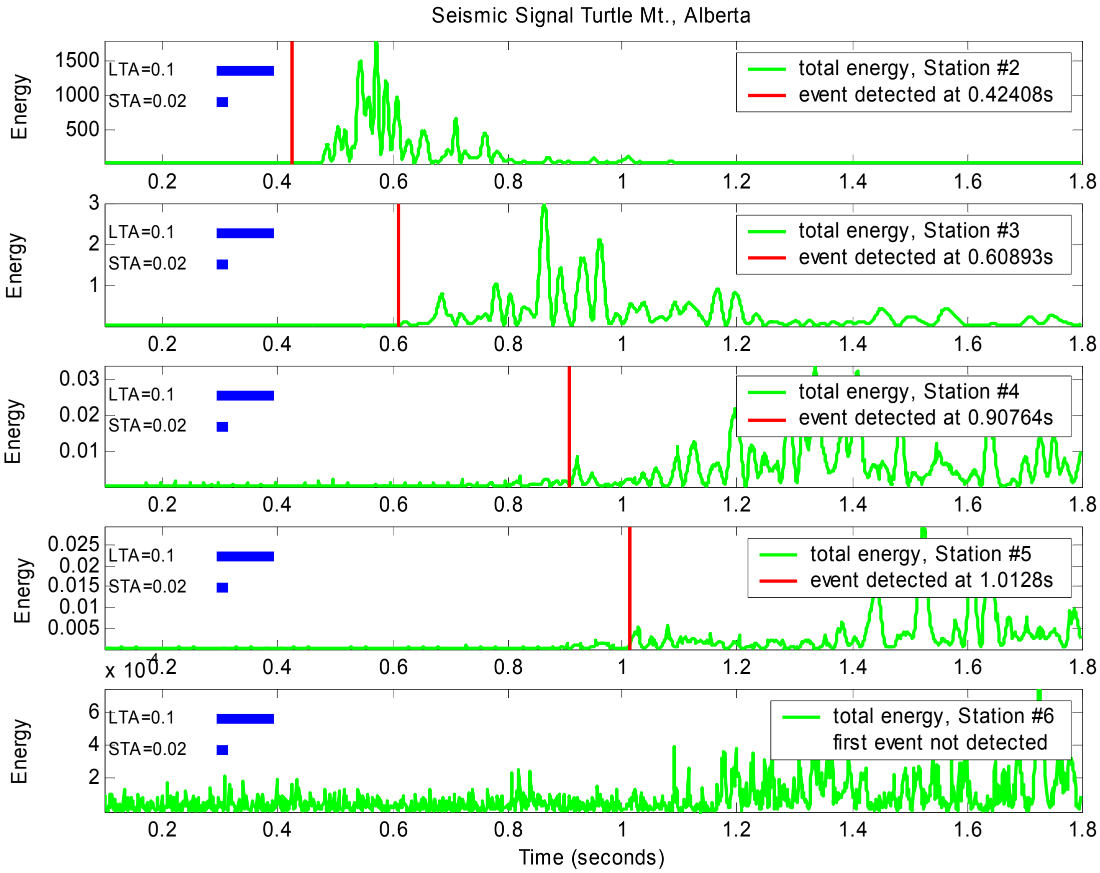

Figure 3-8 Total energy on stations #2 through #6. Red line indicates the first P-wave arrival time picked with the STA threshold of 0.02 and STA/LTA threshold of 2.3.

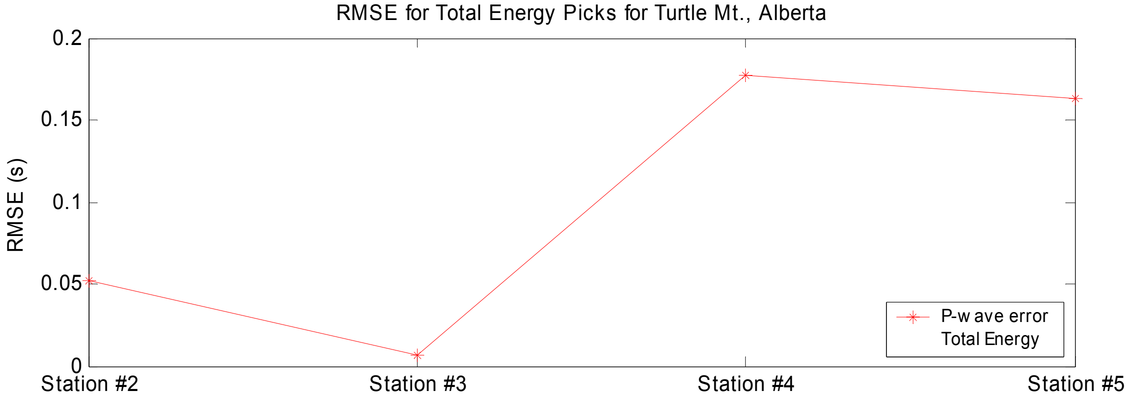

Figure 3-9 RMS errors for Turtle Mt., Alberta data using the total energy technique. Note that station #6 did not detect the P-wave arrival.

The RMS errors associated with the total energy technique are quite large for the P-wave on all stations with the exception of station #3 at 6ms, see Figure 3-9. These P-wave errors are most likely due to the signal's emergent character; that is the signal does not appear to have a crisp first arrival and its amplitude tends to increase after the events arrival instead of immediately decreasing.

3.5.2 Multi-window Amplitude Technique

Using the multi-window technique as discussed in chapter 2, I attempt to discern the detection and arrival times for the data acquired at Turtle Mt., Alberta. The results from the multi-window technique are displayed in Figure 3-10 for station #2 and Figure 3-11 for all stations.

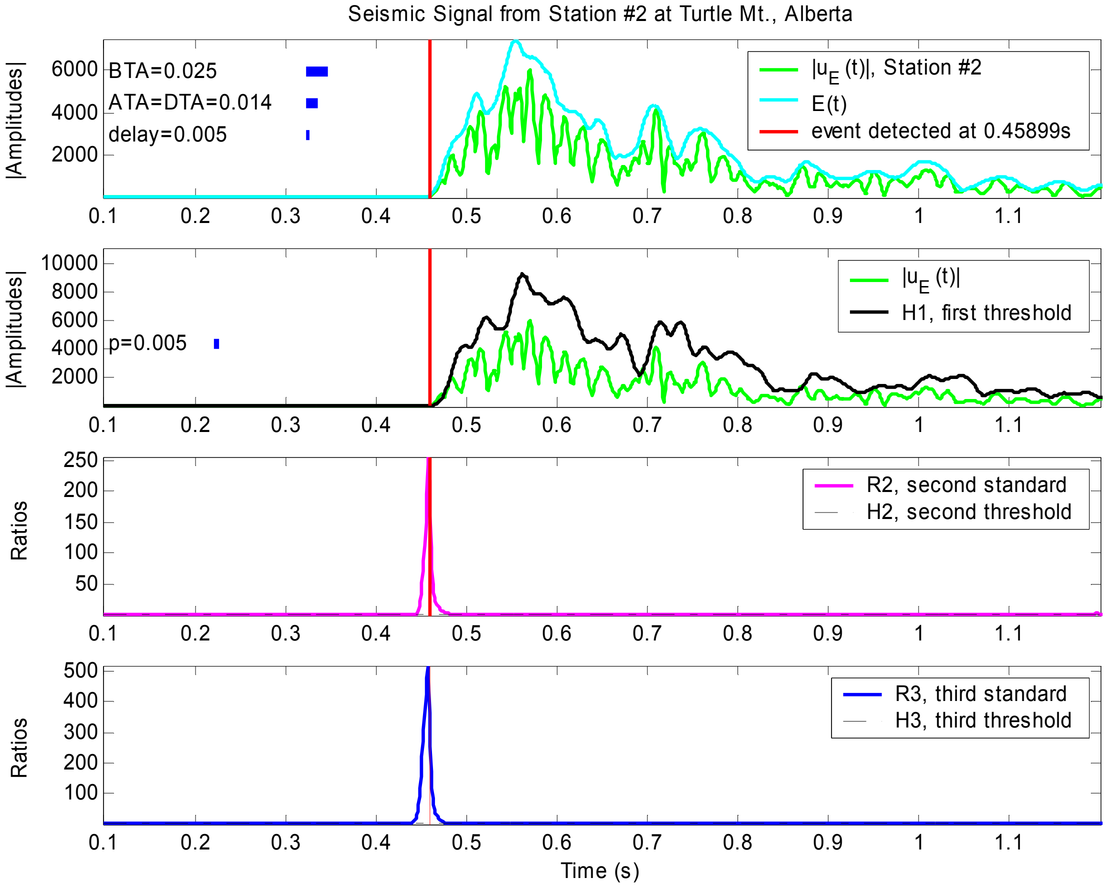

Figure 3-10 Total absolute amplitude calculated for the record at Station #2, Turtle Mt., Alberta. Diagrams from top to bottom represent the absolute value of the synthetic seismogram (green) and its envelope (light blue); first standard $|u(t)|$ (green) and variable threshold H_1 (black); second standard R_2 (magenta) and threshold H_2 (black, dashed); third standard R_3 (blue curve) and threshold H_3 (black,dashed). Note that the red line indicates first P-wave detected.

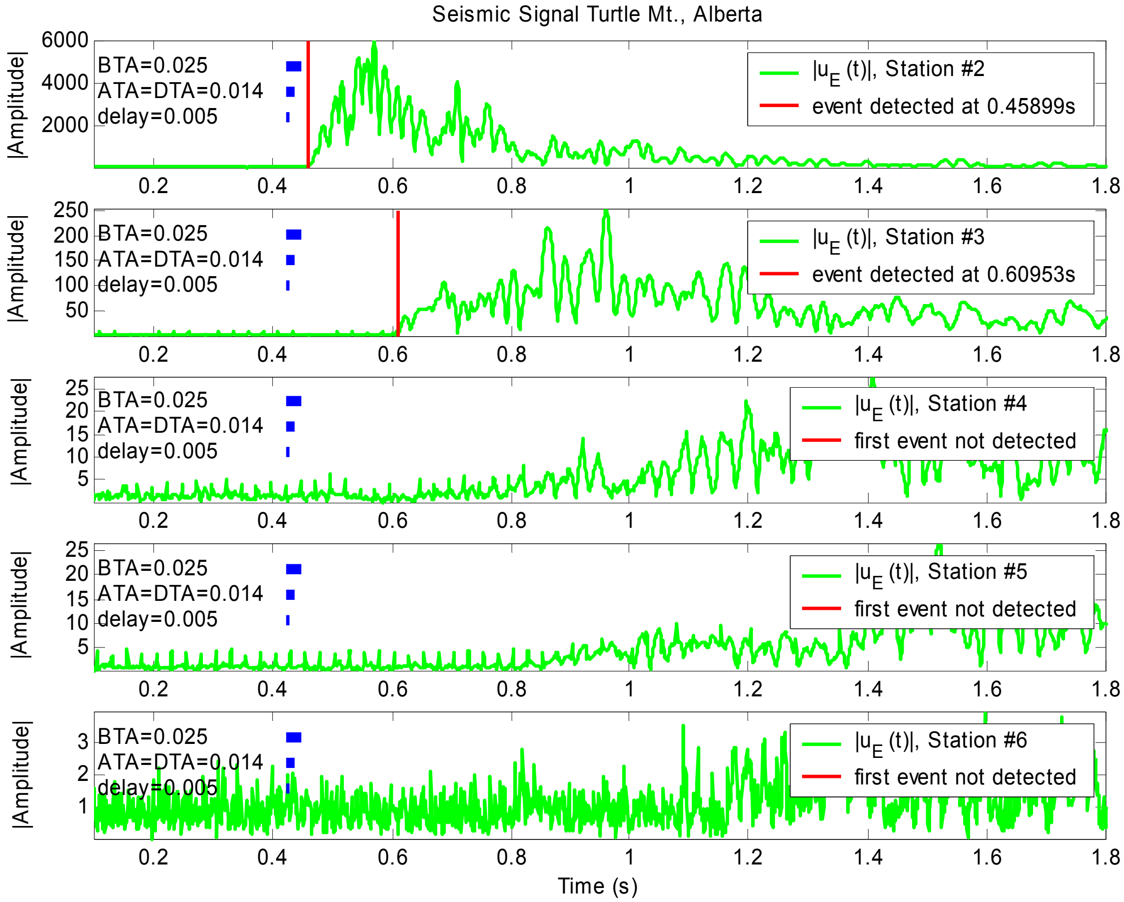

Figure 3-11 Total absolute amplitude on all stations for Turtle Mt., Alberta. Red lines are first arrival time picks.

The total 3-C multi-window technique results are dissatisfying for the P-wave detection on all stations as only the first two stations actually recorded an event. Station #2 and #3 were the only stations to detect an event and the RMS errors associated with the onset-time picks were found to be 17ms and 5.5ms, respectively. These undetected events are directly related to the event being emergent; as the first threshold was most likely not surpassed, see Figure 3-10. The RMS errors associated with the picks for Station #2 are displayed for comparison with the other techniques in Figure 3-19.

3.5.3 Autoregressive – Akaike Information Criteria (AR-AIC)

Using the AR-AIC summation technique as discussed in chapter 2, I aim to select the arrival times for the data acquired at Turtle Mt., Alberta. The results from the AR-AIC technique are displayed in Figure 3-12 and Figure 3-13. The RMS errors associated with the picks for all stations are displayed in Figure 3-14. The RMS errors associated with the picks for station #2 are displayed for comparison with the other techniques in Figure 3-19.

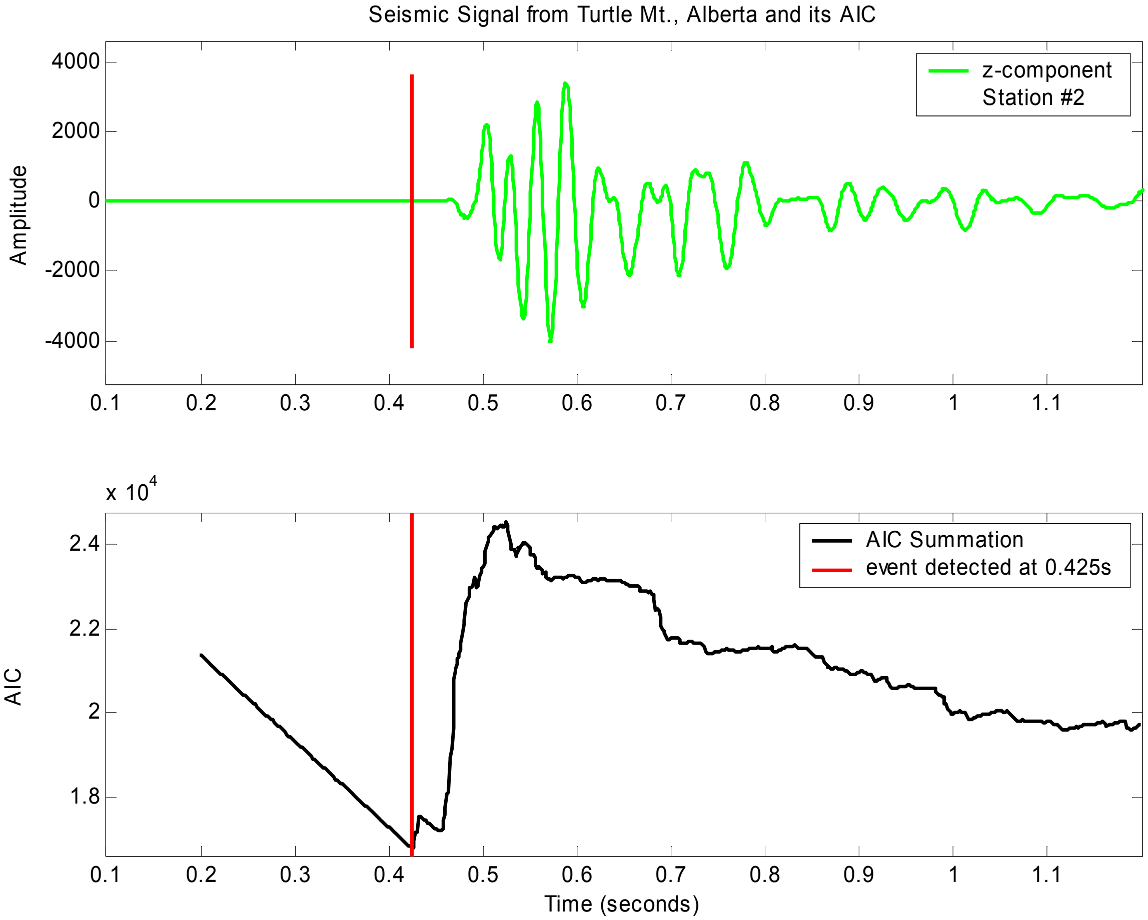

Figure 3-12 (i) Z-component amplitude on station #2, Turtle Mt., Alberta;(ii) AIC for the AR model used in the summation of 3-C technique. Red line indicates the detection of the P-wave arrival time.

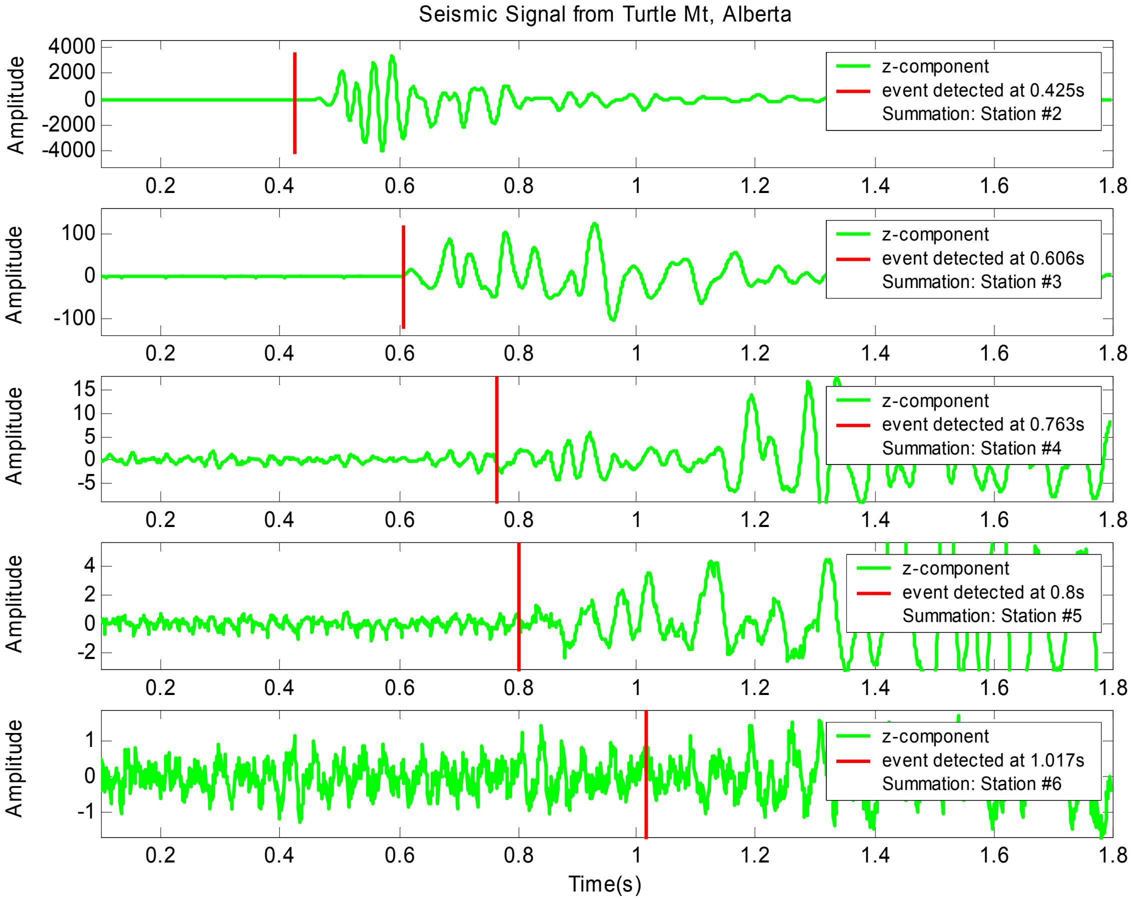

Figure 3-13 Z-component amplitude on all 5 stations at Turtle Mt., Alberta. Red line indicates the detection of the P-wave arrival time using the AR-AIC 3-C summation technique.

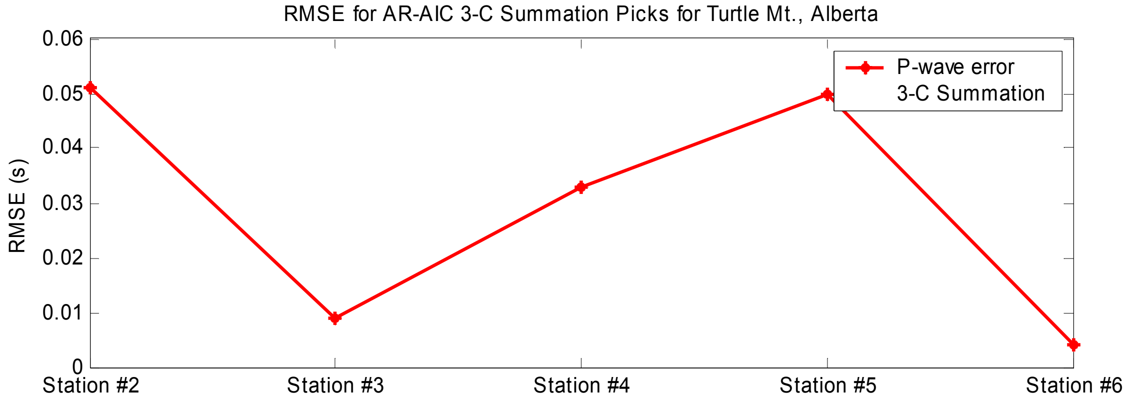

Figure 3-14 RMS errors for Turtle Mt., Alberta data using the AR-AIC 3-C summation technique.

The RMS errors associated with the AR-AIC 3-C summation technique are somewhat reasonable for the P-wave on stations #3 and #6 with values around 9ms and 6ms, respectively, see Figure 3-14. However, for the situation at stations #4 and #5, it is most likely that the arrival of the P-wave was not sufficiently distinct from background noise. Thus, there was not a clear minimum AIC for those P-wave arrivals. It is gratifying to see that the AR-AIC technique was able to detect the P-wave arrivals on more stations than the energy and multi-window technique. This emphasizes the results from chapter 2, with regards to the AR-AIC having a greater ability to resolve events in low SNR environments.

3.5.4 S-Transform Technique

Using the S-transform technique applied to the total energy of the 3-C signal as discussed in chapter 2, I aim to select the arrival times for the data acquired at Turtle Mt., Alberta. The results from the S-transform technique are displayed in Figure 3-15 and Figure 3-16. The RMS errors associated with the picks for all stations are displayed in Figure 3-17. The RMS errors associated with the picks for station #2 are displayed for comparison with the other techniques in Figure 3-19.

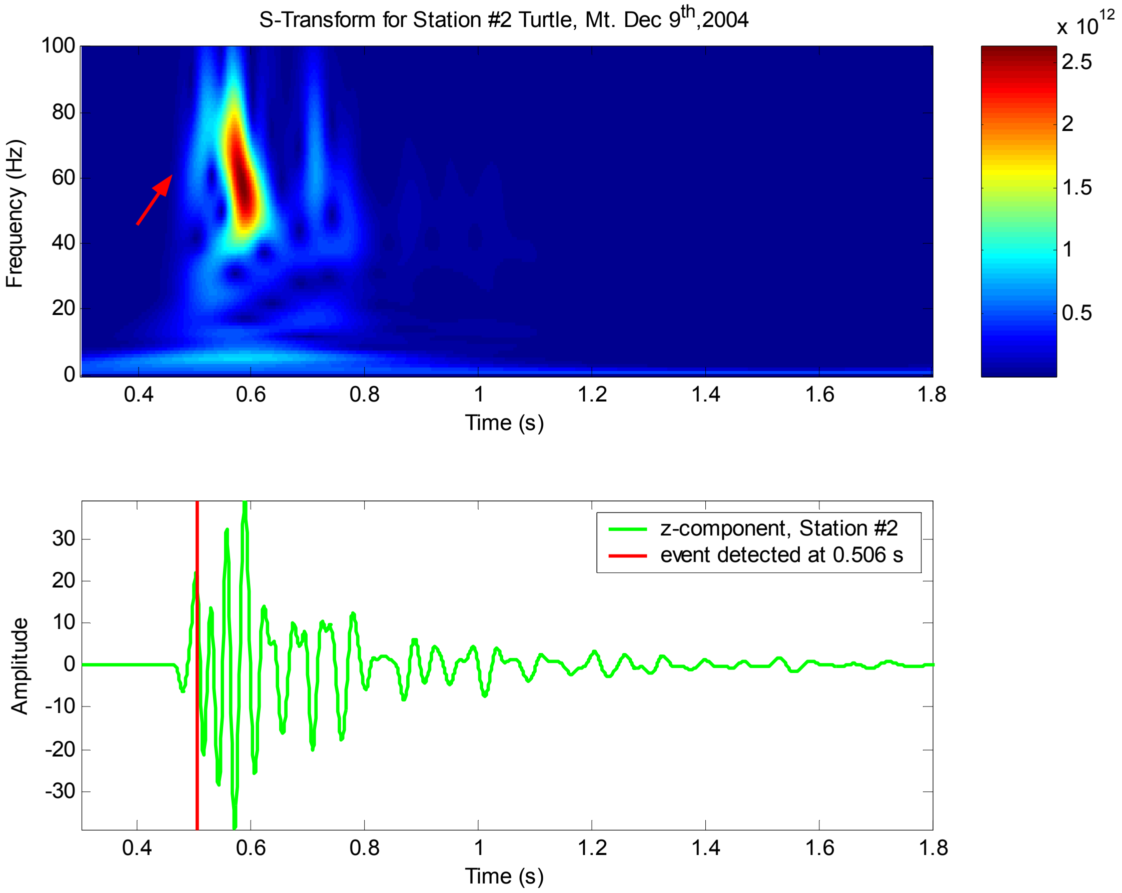

Figure 3-15 top: S-transform of the total energy for station #2 at Turtle Mt., AB. Red arrow represents the P-wave arrival. Bottom: Arrival time picks for P-wave generated from S-transform displayed on the z-component. Red lines represent the P-wave arrival pick.

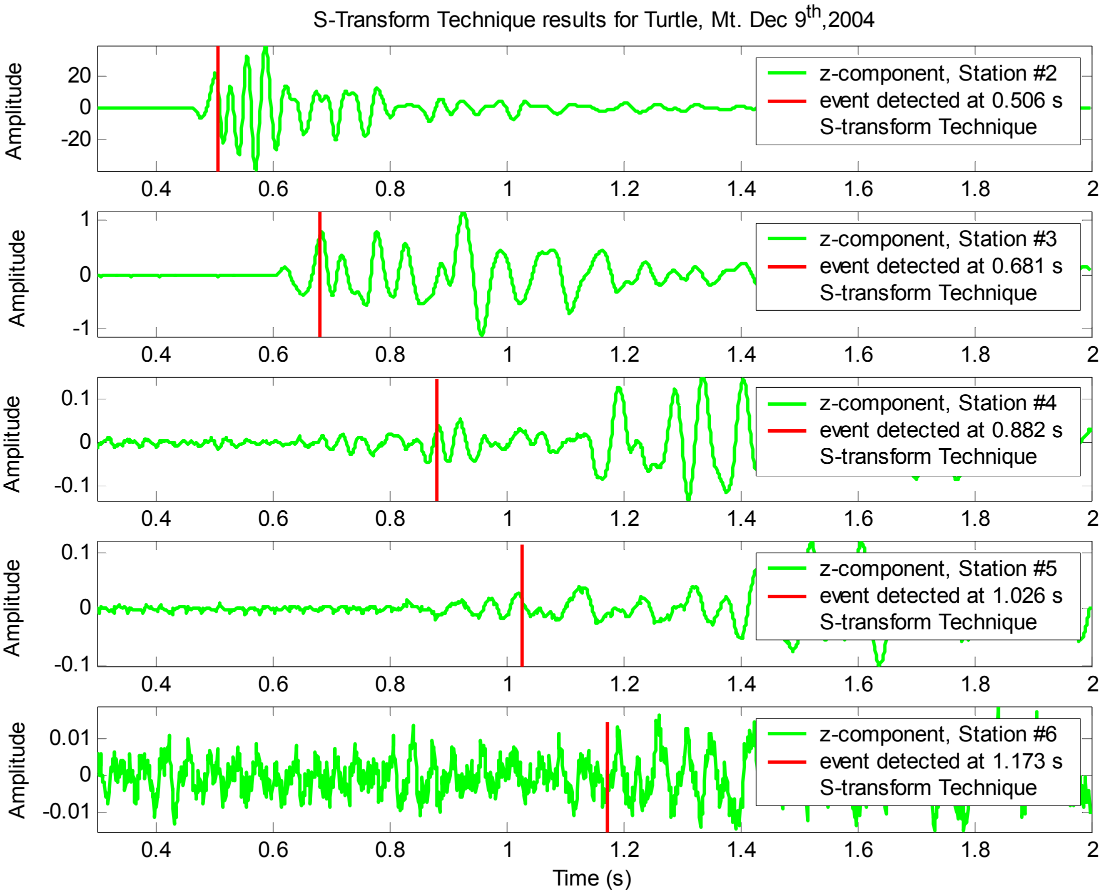

Figure 3-16 Arrival time picks (red) for P-wave generated from S-transform of total energy for stations displayed on their z-components.

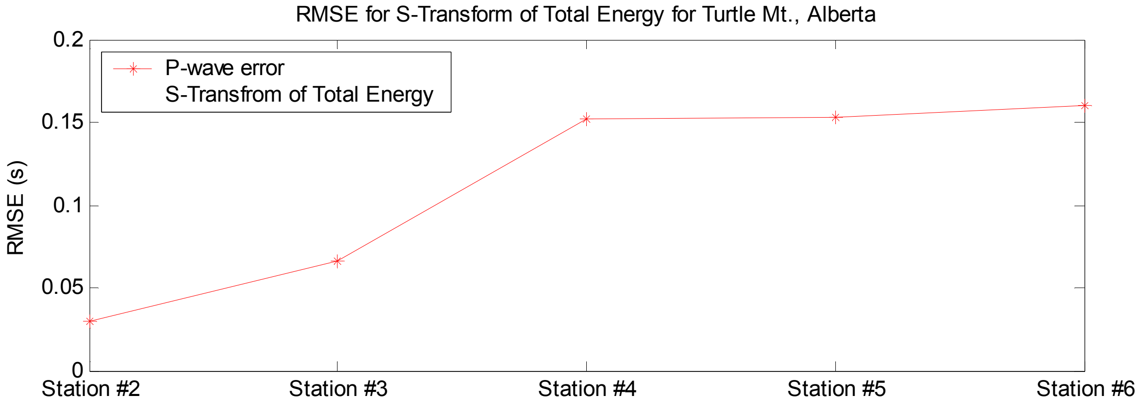

Figure 3-17 RMS errors for S-transform of total energy for stations at Turtle Mt., Alberta.

The RMS errors associated with the S-transform technique are fairly large on all stations; this is most likely a result of the emergent nature of the P-wave arrival. Thus, the amplitude of the S-transform does not surpass the threshold value near the actual arrival of the P-wave. Despite the application of a maximum S-transform onset-time correction, it is most likely that the maximum of this emergent P-wave arrival will not return the onset-time pick to the visual arrival. It is pleasing to see that the S-transform technique was able to detect the P-wave arrivals on all stations. This reinforces the results from chapter 2, with regards to the S-transform having a greater ability to resolve events in low SNR environments.

3.6 Location of Seismic Event at Turtle Mt., Alberta

The location of the seismic event or hypocentre is the information that is desired by seismologists, geologists and geotechnical engineers. To determine the hypocenter of a seismic event the P-wave arrivals or P-and S-wave arrival time intervals from multiple stations are required. Also, the locations of the stations and the velocity of the local geology are needed. The P-wave arrival times from the five stations that did record the seismic event at Turtle Mt., AB on December 9th, 2004, along with the velocities of the local geology can be used to determine the hypocenter.

Here, I have used a hypocenter location algorithm that uses a homogeneous velocity model of 4500m/s. From the manual P-wave arrival picks displayed in Figure 3-6 the location of the hypocenter for this seismic event was determined with the assistance of Dr. Z. Chen in the CREWES project at the University of Calgary, Alberta. The position of the seismic event recorded on December 9th, 2004 at Turtle Mt., Alberta, is displayed on a contour map of the Turtle Mt. in Figure 3-18 and is contained in Table

3.6-1. As seen in Table 3.6-1, the errors associated with the accuracy of the hypocenter location are very large, thus indicating the P-wave arrival time picks have comparable uncertainty. This is a reflection of the difficulties associated with even manually picking onset-times.

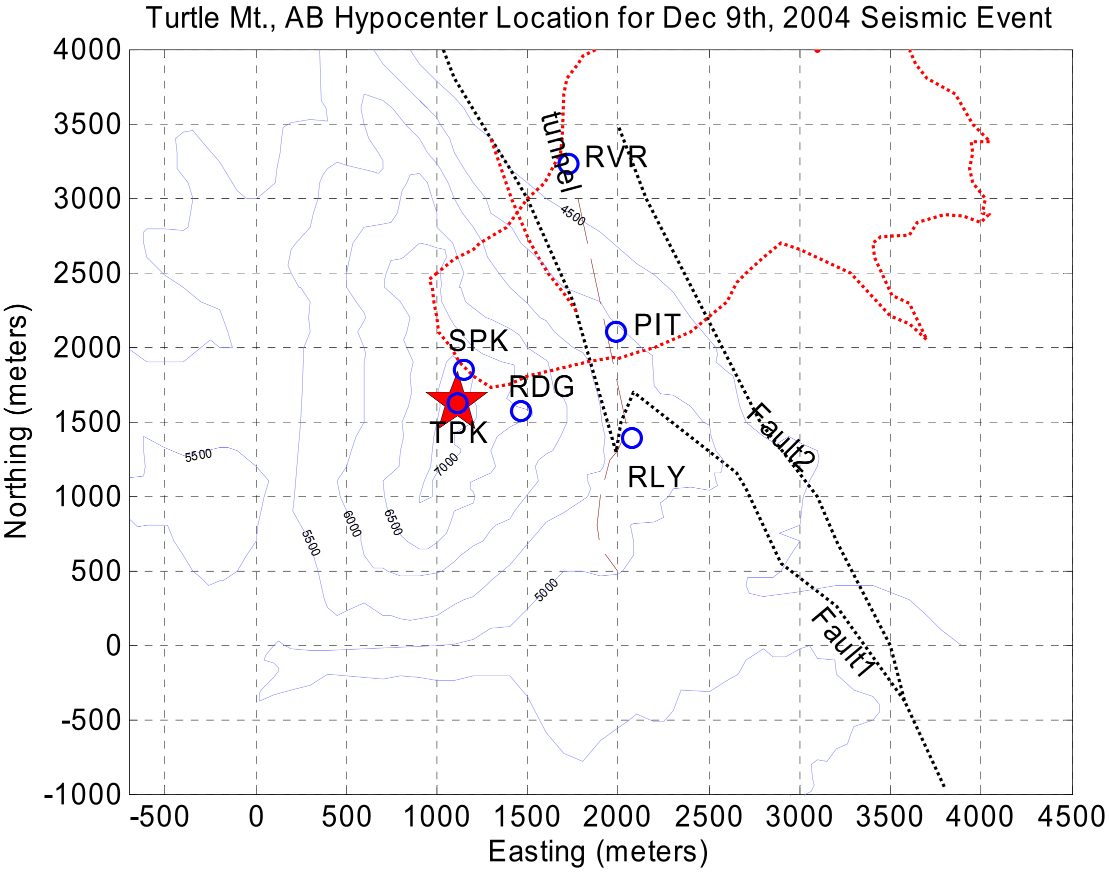

Figure 3-18 Contour map of Turtle Mt. region, displaying the location of the seismic event recorded on Dec 9th, 2004. Red star is location of epicentre; hypocenter is located at about 5m in depth. As well, the red dashed area represents the Frank slide deposits; black dotted lines represent the thrust faults; brown line represents a projection of the tunnel created during coal production. See Table 3.6-1 for hypocenter coordinates and errors and Table 3.6-2 for notation of station locations.

Table 3.6-1 Hypocenter coordinates and errors for Dec 9th, 2004 seismic event at Turtle Mt., AB.

Coordinate Direction	Hypocenter	Error
Easting (m)	1114.02	+/- 686
Northing (m)	1625.88	+/- 1361
Depth (m)	-5.31	+/- 1181

Table 3.6-2 Station naming convention for Figure 3-18

Acronyms	Station Name	Station Number
SPK	South Peak	1
TPK	Third Peak	2
RDG	Ridge	3
RLY	Relay	4
PIT	Pit	5
RVR	River	6

3.7 Conclusion

To summarize, from the data acquired at Turtle Mt. the detection and picking of the P-wave arrivals was attempted using the energy, multi-window, AR-AIC, and S-transform technique. The selection of P-wave arrival times on all stations was complicated by the emergent nature of the seismic events.

The P-wave arrival times picked on station #2 for the energy, multi-window, AR-AIC, and S-transform techniques are displayed for assessment in Figure 3-19. From Figure 3-19 it can be seen that the multi-window technique resolves the P-wave arrival with the least amount of diversion from my manual picks on Station #2. As well, for this particular station the energy and AR-AIC techniques P-wave errors are quite similar at around 50ms. Lastly the S-transform P-wave pick for Station #2 is in the middle of the pack with an error of 30ms.

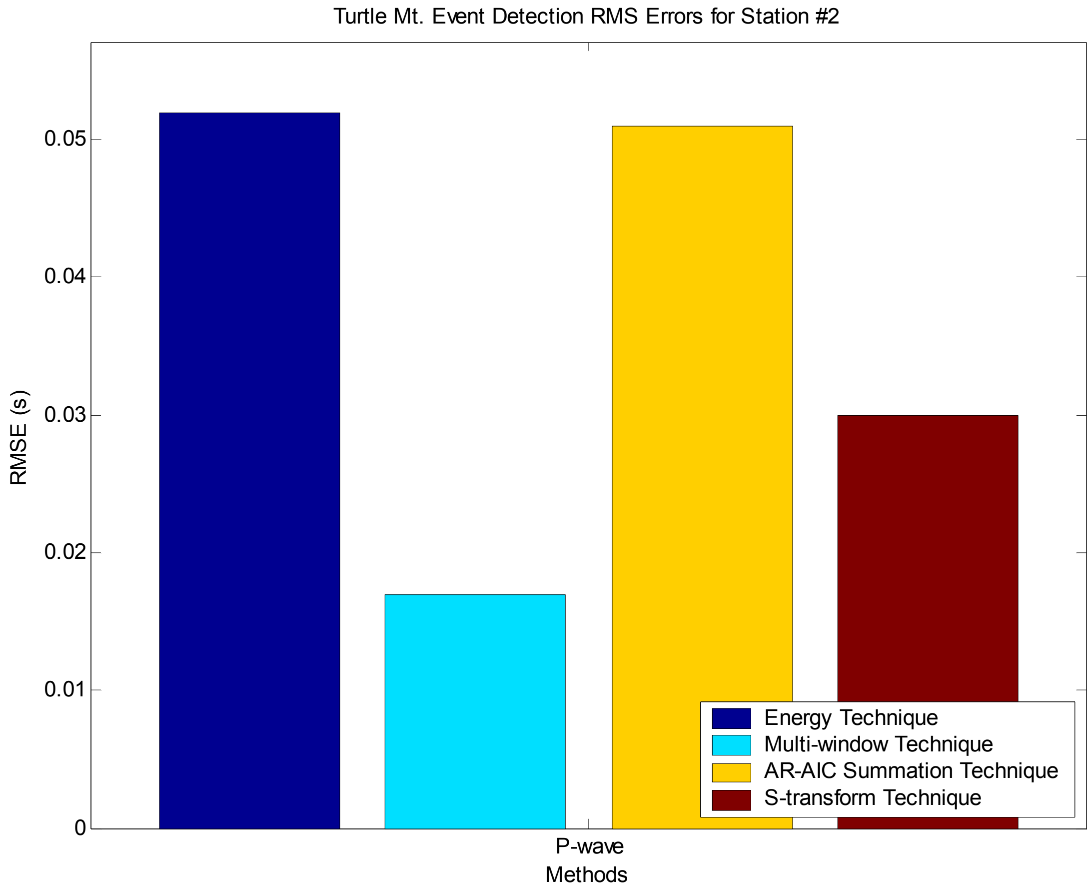

Figure 3-19 RMS errors for various techniques for a seismic event recorded on Station #2, Turtle Mt., AB.

The energy technique was able to resolve the P-wave arrival on four out of the five stations, however, with a larger RMS error. The multi-window techniques were only able to detect events on stations #2 and #3 and were within a reasonable error. The AR-AIC summation technique proved to have a greater ability to select the P-wave arrivals, as it resolved the arrivals on all five stations where two were within an error of 10ms. Finally, the S-transform technique was able to detect the arrival times of the P-waves on all stations. Although, the RMS errors for three out of the five stations were between 150ms and 160ms for an initial investigation this technique does look promising. Perhaps with a more computationally intensive algorithm these errors may be minimized.

CHAPTER FOUR: Case Study II: Cold Lake, AB

4.1 Cold Lake, Alberta, Background

The Cold Lake oil-sand deposits are located in northern Alberta; they are composed of bitumen, sand, clay and water (Imperial Oil, 2004). Figure 4-1 displays the location of Cold Lake, Alberta, and Figure 4-2 shows the stratigraphy of the Cold Lake area.

Figure 4-1 Map of western Canada illustrating the location of the Cold Lake deposit (Talebi et al., 1998).

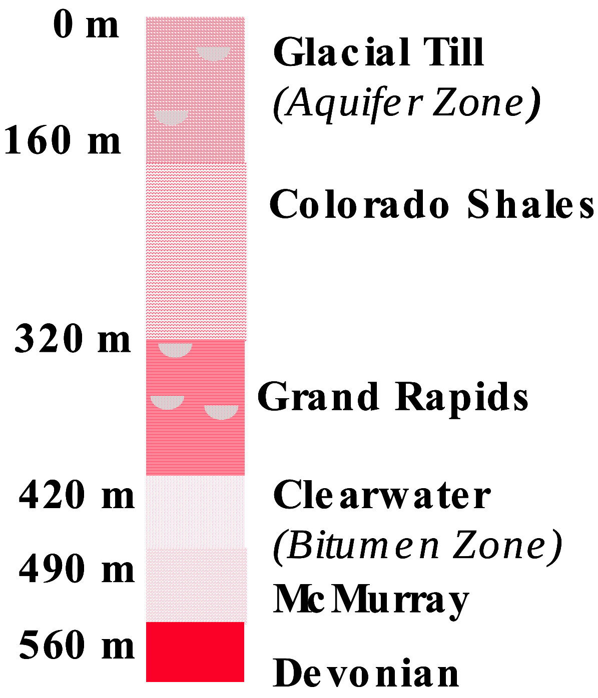

Figure 4-2 Cold Lake Stratigraphy (Courtesy of Henry Bland).

The producing reservoir is the Clearwater sands. The bitumen is situated at 400 meters below the surface; thus, it cannot be recovered by surface mining (Imperial Oil, 2004). Imperial Oil's advancements in oil recovery have resulted in a process called cyclic steam-stimulation (CSS) (Imperial Oil, 2004). Their procedure injects steam into the oil-sands reservoir to warm the bitumen permitting its movement (Imperial Oil, 2004). Figure 4-3 illustrates the three-stage process of CSS.

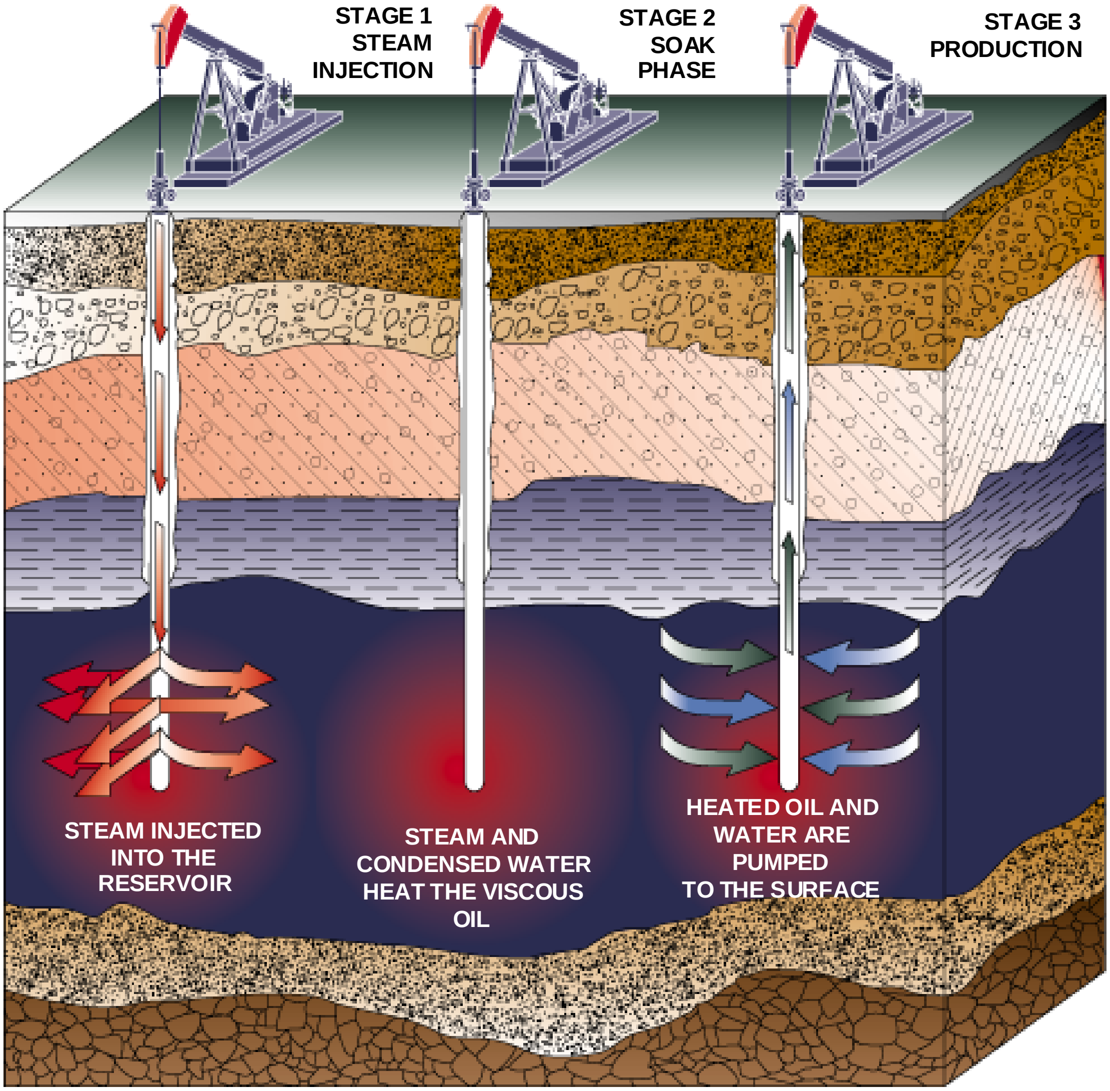

Figure 4-3 Cyclic steam stimulation has been successfully employed by Imperial Oil Res. Ltd. to extract heavy oil. The three-stage process taking place all in the same well is as follows; stage 1, steam is injected into the reservoir; stage 2, steam and condensed water heat the viscous oil; stage 3, heated oil and water are pumped to the surface (Imperial Oil, 2004).

During the CSS process, microseismic data was recorded by Imperial Oil using five, 3-C geophones positioned at intervals down a near-by borehole and recorded at a sample rate of 0.33ms. Analysis of quantities of data acquired before, during and after such production stages could result in the ability to map fluid movement with microseismicity.

4.2 Analysis of data from Cold Lake, Alberta

To investigate the effectiveness of the algorithms interrogated in chapter 2 to detect and pick the arrivals of seismic waves, I have applied them to data acquired by Imperial Oil at Cold Lake, Alberta. Figure 4-4 displays the seismic event recorded on all 5 stations at Cold Lake. From Figure 4-4 it can be seen that the amplitude of the signal has been clipped and the y-component on Station #3 is dead and did not record this event. These problems may cause difficulties with locating the S-wave arrival. Figure 4-5 displays the total energy of the 3-C recordings at all five stations for a microseismic event, along with my manual picks for the arrival of a P-and S-wave.

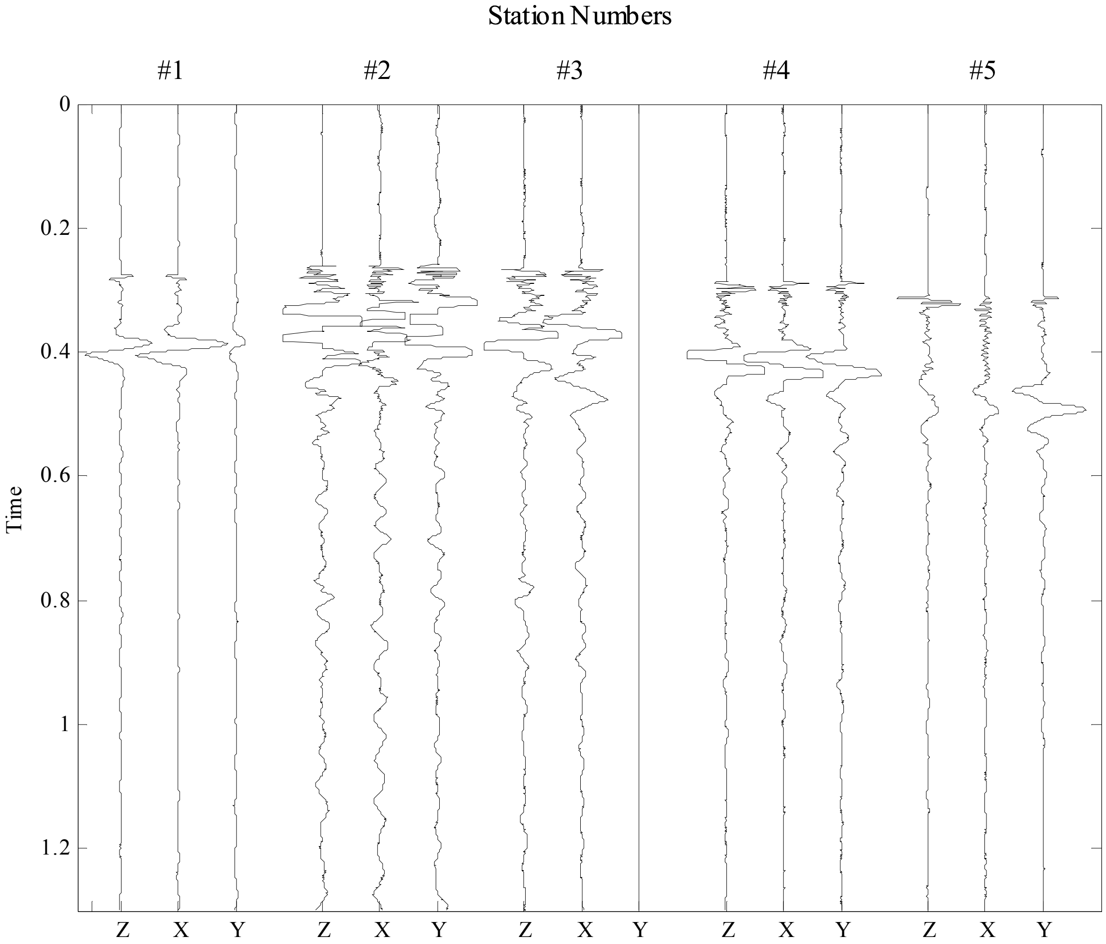

Figure 4-4 Data recorded at Cold Lake, Alberta during CSS with various amplitude gain applied.

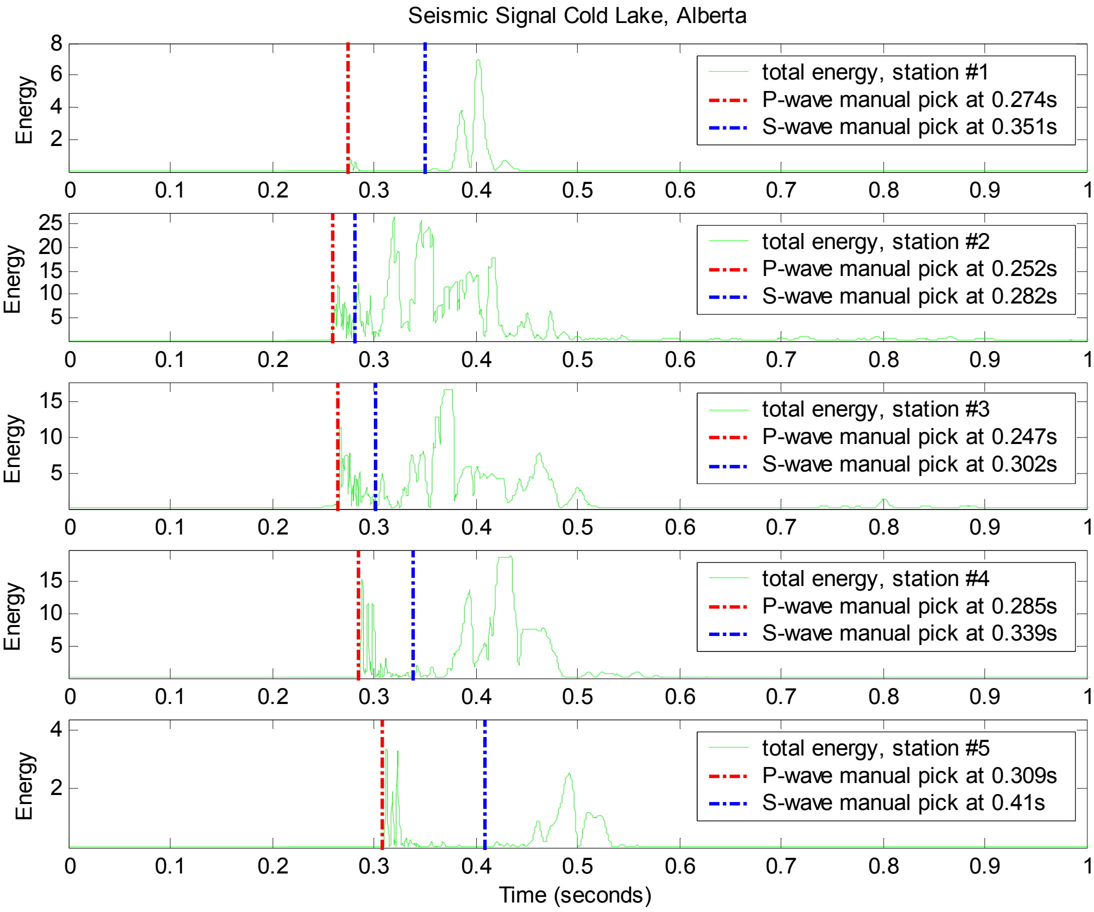

Figure 4-5 Total energy calculated for the seismic event recorded at stations #1 through #5. Red line indicates the first P-wave arrival time picked manually. Blue line represents the second event arrival time picked manually.

In this chapter, I employ the energy technique with an onset-time correction applied to detect and pick the arrivals of seismic events on data from Cold Lake, AB. I use only the total energy of the 3-C seismic record, as it was shown to be the most robust energy technique in chapter 2. As well, I apply the multi-window technique, using the 3-C magnitude function. Finally, I apply the AR-AIC technique using the summation of the AIC's for all 3-components, as this function was also shown to be the most robust AR-AIC algorithm in chapter 2. It is important to notice that this data has been clipped accidentally by the geophone, as the gain settings were not correct, thus the amplitude of the S-wave has been cut-off.

4.2.1 Energy Technique

To determine the detection and arrival times for the data acquired at Cold Lake, Alberta, I utilize the energy technique with an onset-time correction applied and using only the total energy of the 3-C seismic record. The results from the energy technique are displayed in Figure 4-6 and Figure 4-7. The RMS errors associated with the picks for all stations are displayed in Figure 4-8. The RMS errors associated with the picks for Station #1 are displayed for comparison with the other techniques in Figure 4-15.

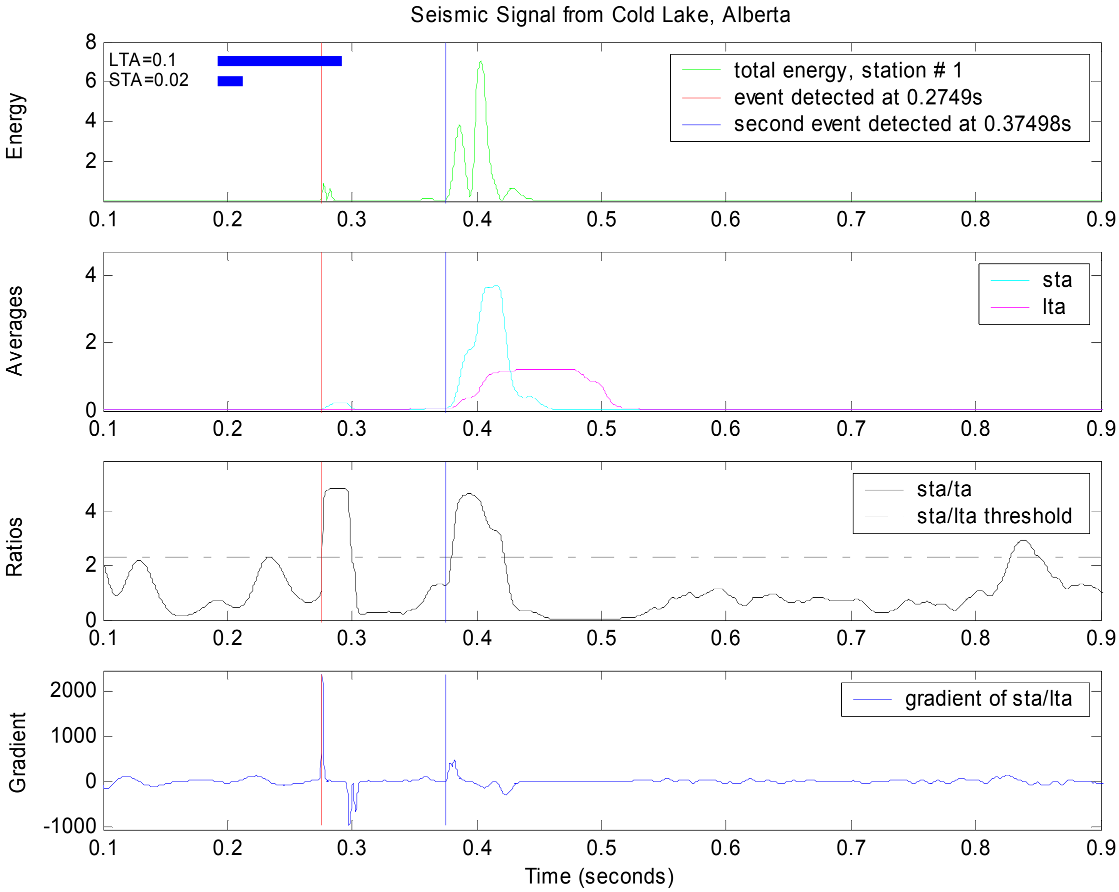

Figure 4-6 From top to bottom: Total energy on station #1; STA and LTA; STA/LTA; Gradient of the STA/LTA. Red line indicates the first P-wave arrival time picked with the STA threshold of 0.02 and STA/LTA threshold of 2.3. Blue line represents the second event arrival time, corresponding here to the S-wave.

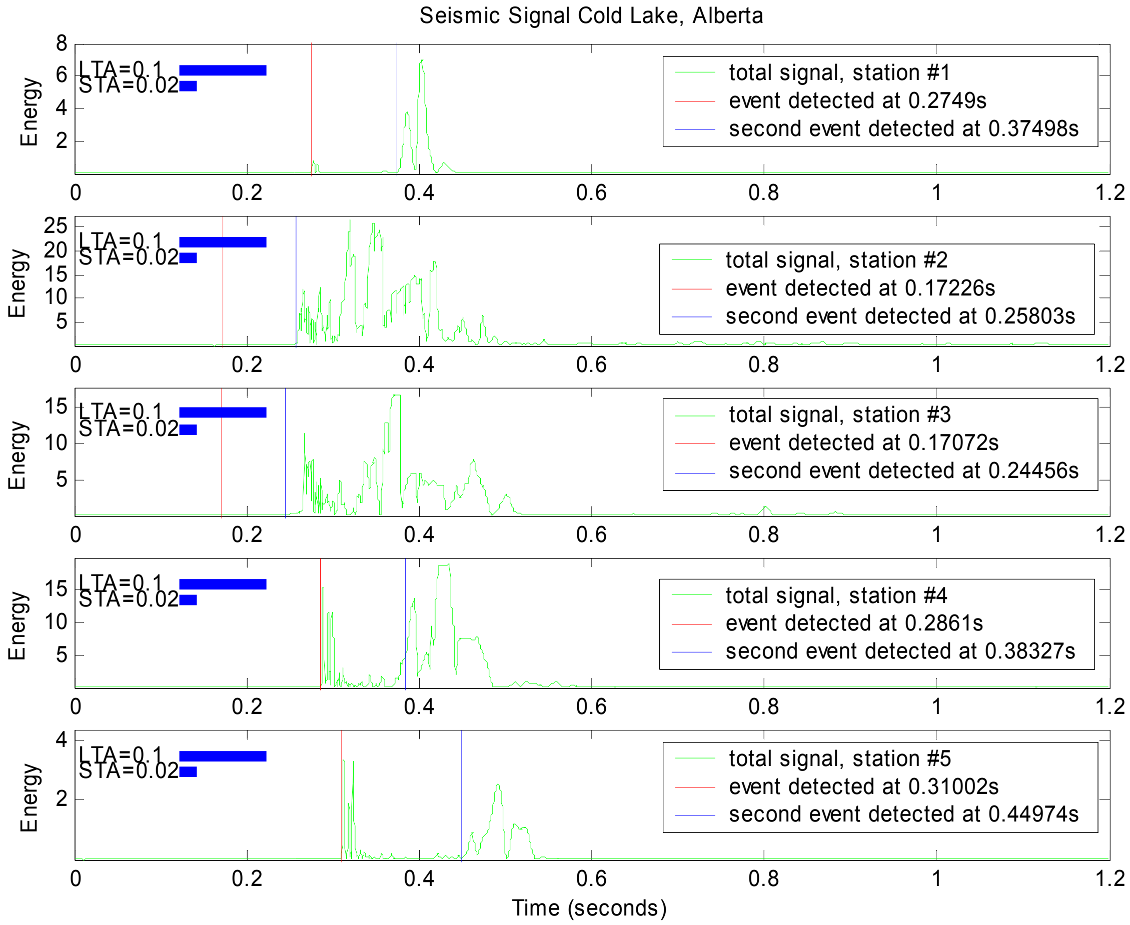

Figure 4-7 Total energy on stations #1 through #5. Red line indicates the first P-wave arrival time picked with the STA threshold of 0.02 and STA/LTA threshold of 2.3. Blue line represents the second event arrival time, sometimes corresponding here to the S-wave.

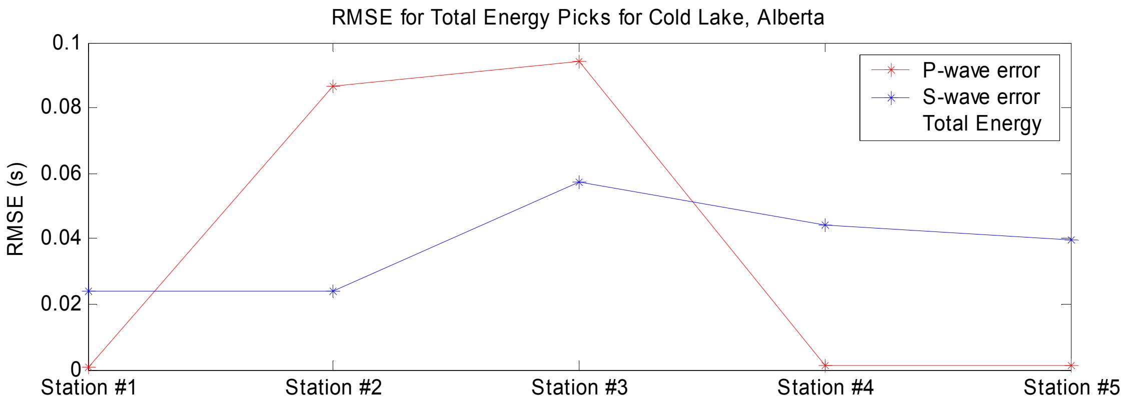

Figure 4-8 RMS errors for Cold Lake, Alberta data using the total energy technique.

The RMS errors associated with the total energy technique are quite low for the P-wave on Stations #1, #4, and #5, at around 1ms, see Figure 4-8. However, the RMS errors for the P-wave on Stations #2 and #3 are extremely erroneous; looking at Figure 4-7 it is obvious that these picks were false triggers. The S-wave RMS errors appear to be consistently large, with the exception of Stations #2 and #3, as the S-wave pick actually corresponds to the P-wave pick. These large S-wave errors may be a result of the Cold Lake data being clipped in error by the recording system.

4.2.2 Multi-window Amplitude Technique

Using the multi-window technique as discussed in chapter 2, I attempt to discern the detection and arrival times for the data acquired at Cold Lake, Alberta. The results from the multi-window technique are displayed in Figure 4-9 and Figure 4-10. The RMS errors associated with the picks for all stations are displayed in Figure 4-11. The RMS errors associated with the picks for Station #1 are displayed for comparison with the other techniques in Figure 4-15.

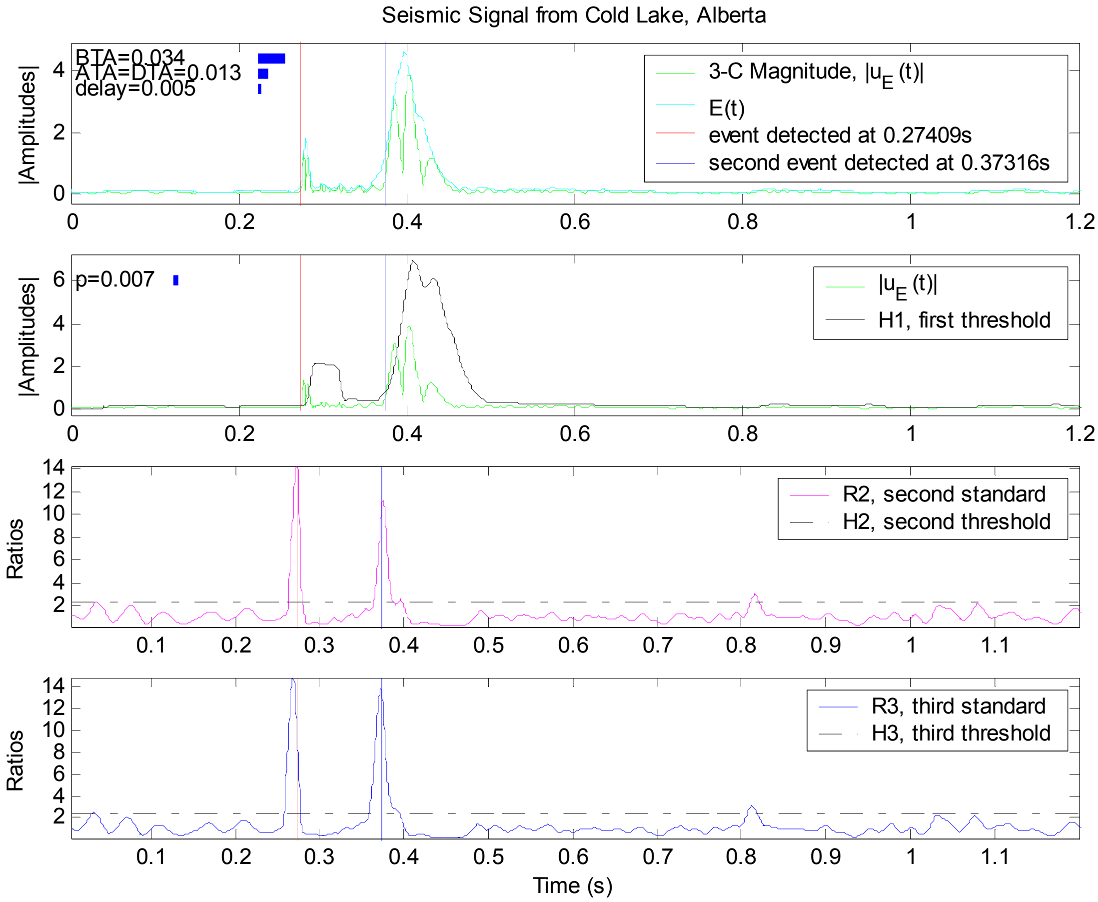

Figure 4-9 3-C magnitude on Station #1, Cold Lake, Alberta. Diagrams from top to bottom represent the sum of the absolute values for the 3-C seismogram (green) and its envelope (light blue); first standard $|u(t)|$ (green) and variable threshold H_1 (black); second standard R_2 (magenta) and threshold H_2 (black, dashed); third standard R_3 (blue curve) and threshold H_3 (black,dashed). Red and blue lines are first and second arrival time picks.

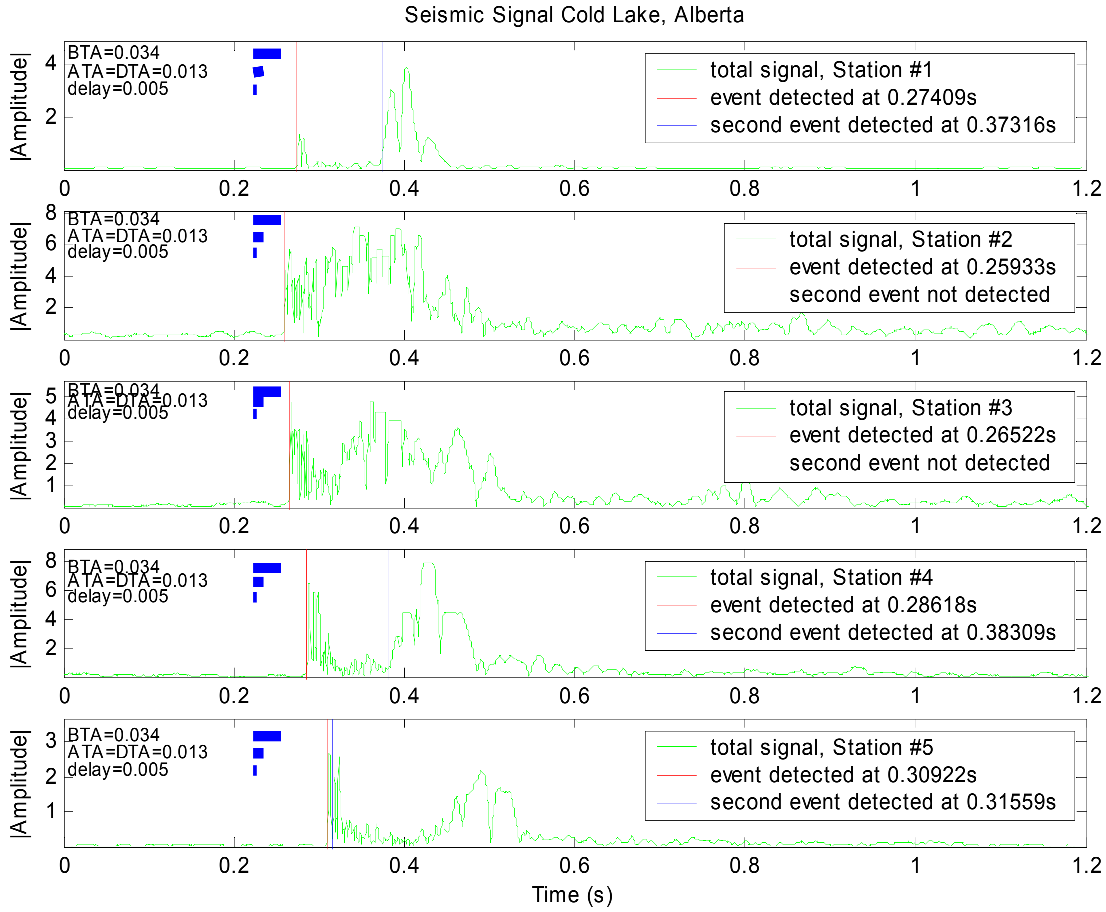

Figure 4-10 3-C magnitude functions technique computed on all stations for Cold Lake, Alberta. Red and blue lines are first and second arrival time picks.

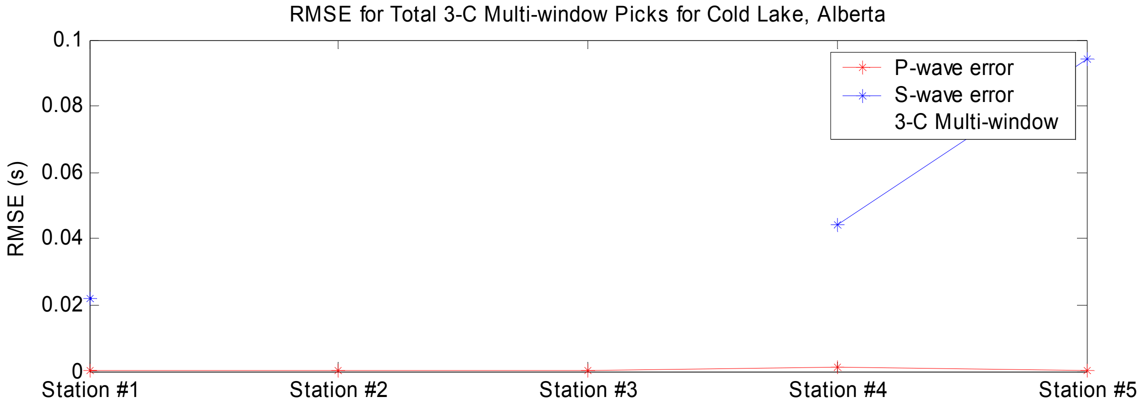

Figure 4-11 RMS errors for Cold Lake, Alberta data using the 3-C magnitude multi-window technique. Note the S-wave was not detected on Stations #2 and #3.

The RMS errors associated with the 3-C magnitude function for the multi-window technique are satisfying for the P-wave on all stations at less than or equal to 1ms, see Figure 4-11. Unfortunately, the S-wave was not detected on two of the five stations and of those detected the errors were quite large. The undetected S-waves were directly related to the regrettably clipped data, as the first threshold was most likely not surpassed. This illustrates my notion in chapter 2, section 2.3; that the multi-window technique would not fare well if the S-wave amplitude was less than the P-wave's, although this may rarely by the case, apart from this clipping situation.

4.2.3 Autoregressive – Akaike Information Criteria (AR-AIC)

Using the AR-AIC summation technique as discussed in chapter 2, I aim to select the arrival times for the data acquired at Cold Lake, Alberta. The results from the AR-AIC technique are displayed in Figure 4-12 and Figure 4-13. The RMS errors associated with the picks for all stations are displayed in Figure 4-14. The RMS errors associated with the picks for Station #1 are displayed for comparison with the other techniques in Figure 4-15.

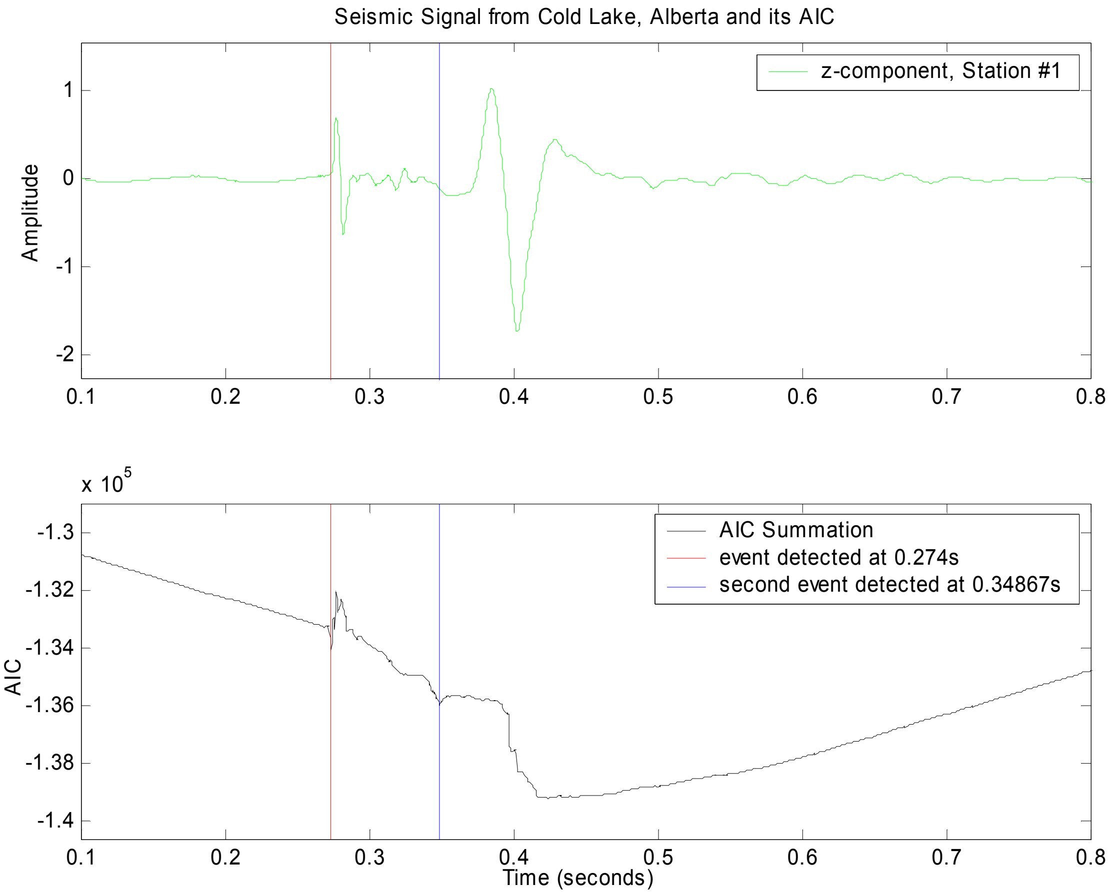

Figure 4-12 Z-component amplitude on Station #1, Cold Lake, Alberta; AIC for the AR model used in the summation of 3-C technique. Red line indicates the detection of the P-wave arrival time. Blue line represents the second event arrival time, corresponding here to the S-wave.

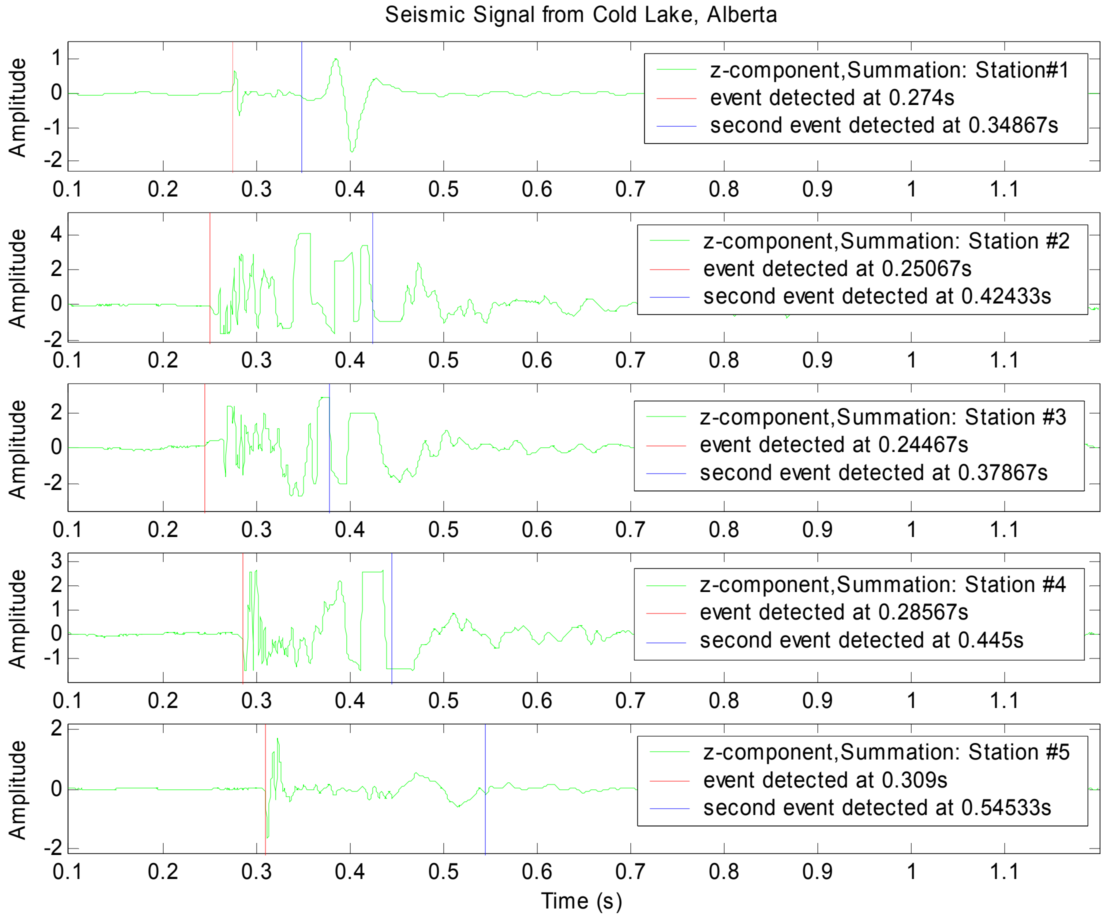

Figure 4-13 Z-component amplitude for all 5 stations at Cold Lake, Alberta. Red line indicates the detection of the P-wave arrival time using the AR-AIC 3-C summation technique. Blue line represents the second event arrival time, corresponding here to the S-wave.

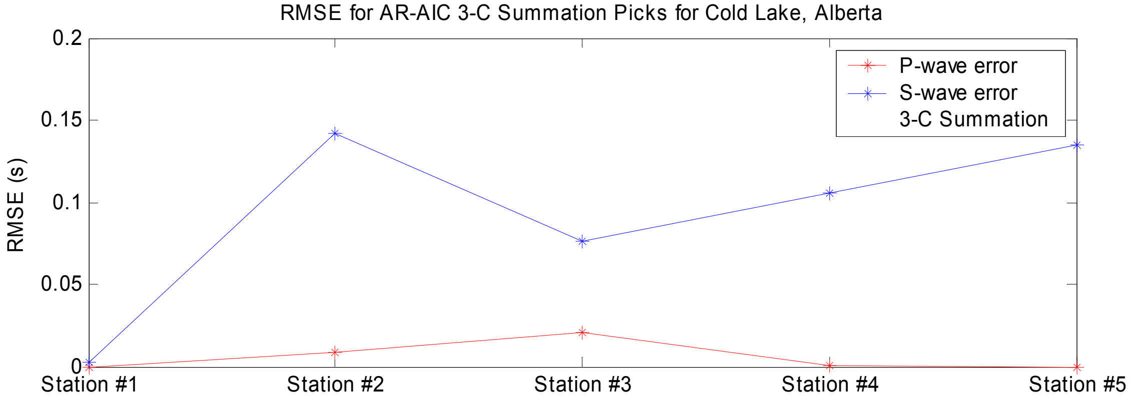

Figure 4-14 RMS errors for Cold Lake, Alberta data using the AR-AIC 3-C summation technique.

The RMS errors associated with the AR-AIC 3-C summation technique are satisfying for the P-wave on stations #1, #4, and #5 with values around 1ms, see Figure 4-14. The S-wave RMS errors were far greater for all stations except the first. The AR-AIC technique does rely upon a distinct amplitude characteristic between the seismic event and background. However, for the situation at stations #2 through #5, it is most likely that the arrival of the S-wave was not sufficiently distinct from the coda of the P-wave. Thus, there is not a clear minimum AIC for the S-wave arrival. I do not feel that the S-wave RMS errors are directly related to the undesirably clipped data.

4.3 Conclusion

To summarize, despite the data acquired during production periods at Cold Lake, AB having their amplitudes clipped, the energy, multi-window and AR-AIC methods were all able to delimit the P-wave arrival time on Station #1 to within around 1ms of my manual picks, see Figure 4-15. While the S-wave arrival time on Station #1 was found to be significantly in error using the energy and multi-window technique, the AR-AIC 3-C summation technique resolved an RMS error of 2.3ms.

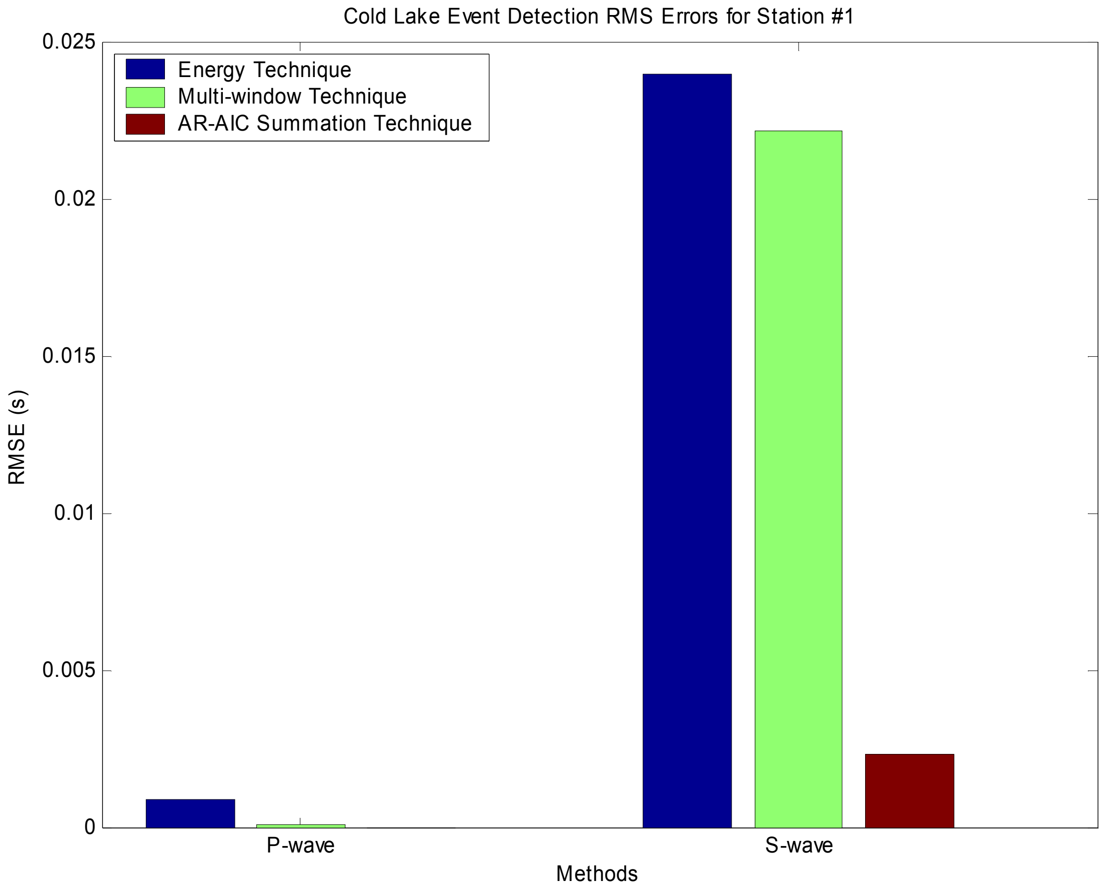

Figure 4-15 RMS errors for various techniques for a seismic event recorded on Station #1, Cold Lake, AB.

Data recorded at stations #2 and #3 proved to be the most difficult for all methods attempted, although the multi-window technique was able to resolve the P-wave arrival times to within 1ms of my manual picks.

Overall, the results are satisfying for the P-wave arrival time picks for all methods, however, the S-wave arrival detection and onset-time picks were not pleasing for the majority of the stations and methods. For the energy and multi-window technique the difficulty with the S-wave detection and time picks was directly related to the clipping of the data. The AR-AIC 3-C summation technique did not perform as well as anticipated for the selection of the S-wave arrival time.

CHAPTER FIVE: Conclusion and Discussion

Accurate and dependable selections of the P-and S-wave arrival times are of immense importance in seismic event location and recognition for many applications. The objective of this thesis is to analyze a variety of event detection and onset-time picking methods in hopes of formulating a more robust algorithm. The methods assessed consist of energy, multi-window, AR-AIC and S-transform techniques.

Synthetic microseismic data were used to assess the energy, multi-window, AR-AIC, and S-transform procedures. Each technique, excluding the S-transform, was evaluated by altering the dominant frequencies and relative amplitudes of the P-and S-waves, and finally, by varying the style of background noises and their SNR's. A few of these techniques were selected to evaluate their capabilities for resolving the S-wave arrival from the P-wave coda. The RMS errors of each method were compared to discern their competency.

Overall, there was found to be a trade-off between the accuracy of the onset-time pick and the number of events detected. The energy and multi-window techniques were found to leave a large number of events undetected when the SNR was reduced, although their accuracy was phenomenal. The energy technique was found to be unsuitable for a low SNR environment. The multi-window technique had a contradicting response to the reduction of the SNR when using a random background noise compared to noise taken from a real seismogram. The AR-AIC and S-transform procedures were found to detect more events and have precise, although less accurate, results when decreasing the SNR. The AR-AIC technique was found to be suitable for all SNR settings. Unfortunately, the

AR-AIC procedure does require an initial trigger technique, thus, its ability to detect more events in a variety of SNR's may deteriorate.

The aptitude of the energy, multi-window and AR-AIC techniques for resolving the S-wave arrival from the P-wave coda were enlightening. The multi-window technique was able to resolve the two arrivals beyond the arrival time interval of 25ms to 20ms, where the energy procedure failed. The AR-AIC procedure had a greater ability to discriminate the P-and S-waves arrivals; to within an arrival time interval of 15ms to 10ms. Thus, for events that are positioned reasonably close to the receivers, the energy technique is not feasible.

Algorithms deemed successful at detecting and picking the arrival times of the P- and S-wave using synthetic data were then assessed with data from Turtle Mt., Alberta, and Cold Lake, Alberta.

The detection and picking of the P-wave arrivals was attempted on data acquired at Turtle Mt. using the energy, multi-window, AR-AIC, and S-transform technique. The selection of P-wave arrival times on all stations was complicated by the emergent nature of the seismic events.

The multi-window procedure failed to detect two of the five S-wave events, while the energy technique faired slightly better, detecting events on four of the five stations, although three of the picks were vastly erroneous. The AR-AIC summation technique proved to have a superior capability at selecting the P-wave arrivals, as it resolved the arrivals on all five stations. The S-transform technique's capacity to select the arrival times of the P-waves on all stations was quite remarkable. Despite the RMS errors for three out of the five stations being between 150ms and 160ms this method shows potential.

The detection and picking of the P-and S-wave arrivals was attempted on data acquired at Cold Lake using the energy, multi-window and AR-AIC techniques. The selection of S-wave arrival times on all stations was complicated by the regrettably amplitude clipped nature of the seismic recordings.

Generally, the results for the selection of the P-wave arrival times are pleasing for all methods on the majority of the stations. However, the S-wave arrival time picks were not satisfying for most of the stations and methods. The difficulties with the S-wave detection and time picks for the energy and multi-window techniques were a direct result of the amplitude clipping. The AR-AIC 3-C summation procedure did not perform as well as expected for the S-wave arrival time pick in comparison to the synthetic results.

In conclusion, prior knowledge of the expectant P-and S-wave arrival intervals, amplitudes and frequencies and the SNR environment is of the utmost importance when selecting an appropriate detection and picking technique. This work establishes a trade-off between the accuracy of onset-time picking and the number of undetected events. It also demonstrates the difficulties associated with data acquired in an oilfield and mountainous region. The AR-AIC and S-transform technique had the ability to resolve emergent events, while the energy and multi-window procedures were inhibited in their detection of the S-wave arrivals when the amplitudes of the data were clipped.

Results from the applications of synthetic seismic events show that for a relatively low SNR environment the AR-AIC technique would be the most applicable as it can still pick the onset time for both the P- and S-wave to within 1ms. Whereas, for a relatively higher SNR setting the multi-window amplitude technique would provide the most accurate onset time picks for both the P- and S-wave.

The objectives of this thesis were met as four methods used to detect and select the onset times for microseismic events were interrogated. A two-step onset time correction was created and applied in the energy and multi-window techniques to improve the resolution of onset times. As well, a simplistic correction was fashioned and employed in the S-transform technique to recover the onset time. Thus, the application of these onset time corrections produced more accurate and robust algorithms.

Further examination of the S-transform technique would provide a more stable automatic event picking method. Unfortunately, such scrutiny was not in the scope of this work.

The onset-time correction applied in this work uses a basic line relation to recover arrival time of waves. There is more work that may be performed to test other relations such as quadratic, cubic, or sinusoidal functions. A variety of relations may better mimic the initial arrival character of the seismic event and this can then be used to backtrack from the trigger time to the true onset time.

REFERENCES

Akaike, H., 1973, Information theory and an extension of the maximum likelihood principle, In: Petrov, B. and Csaki, F. (eds), 2nd International symposium on Information Theory, 267-281.

Aki, K. and Richards, P.G., 1980, Quantitative Seismology: Theory and Methods, (2), W.H. Freeman Co., San Francisco, CA.

Aki , K. and Richards, P.G., 2002, Quantitative Seismology second edition: University Science Books, Saulsalito, CA.

Aki, K., 1976, Scaling low seismic spectrum: J. Geophys. Res., 72, 1217-1231.

Allan, J.A., 1933, Third Report on the stability of Turtle Mountain: Department of Public Works, Edmonton, Alberta, 28 pp.

Bai, C-Y. and Kennett, B.L.N., 2000, Automatic phase-picking and event location by full use of a single three-component broadband seismogram: Bull. Seis. Soc. Am., 90 (1), 187-198.

Bai, C-Y. and Kennett, B.L.N., 2001, Phase identification and attribute analysis of broadband seismograms at far-regional distances: J. Seis., 5 (2), 217-231.

Berkeley Digital Seismic Network (BDSN), 2004: http://seismo.berkeley.edu/bdsn/bdsn_overview.html

Bingham, D.K., 1996, Seismic monitoring of Turtle Mountain: Internal report, Alberta Environment Protection. Government of Alberta.

Chen, Z. and Stewart, R., 2005, Multi-window algorithm for detecting seismic first arrivals: CSEG abstracts, 355-358.

Daly, R.A., Miller, W.G., and Rice, G.S., 1912, Report of the commission appointed to investigate Turtle Mountain, Frank, Alberta: Geol. Surv. Canada, Mem. 27, 34 pp.

Douglas, A., 1997, Bandpass Filtering to Reduce Noise on Seismograms: Is There a Better Way?: Bull. Seis. Soc. Am., 87 (4), 770-777.

Earle, P.S. and Shearer, P.M., 1994, Characterization of global seismograms using an automatic-picking algorithm: Bull. Seis. Soc. Am., 84, 366-376.

Federation of American Scientists (FAS), Comprehensive Test Ban Treaty Chronology, 2004: http://www.fas.org/nuke/control/ctbt/chron1.htm

Field, M., and McIntyre, D., 2003, On the Edge of Destruction: Canada's deadliest rockslide: Mitchell Press, Vancouver, B.C.

Freeman, H.W., 1966a, The "little variable factor" a statistical decision of the readings of seismograms: Bull. Seis. Soc. Am., 56,593-604.

Freeman, H.W., 1966b, A statistical discussion of Pn residuals from explosions: Bull. Seis. Soc. Am., 56, 677-695.

Freeman, H.W., 1968, Seismological measurements and measurement error: Bull. Seis. Soc. Am., 58, 1261-1271.

Imperial Oil Ltd., 2004: http://www.limperiale.ca/Canada-English/Investors/Operating/Natural_Resources/I_O_NaturalOilSandsDisclosure04.asp

Jones, P.B., 1993, Structural geology of the modern Frank slide and ancient Bluff `Mountain Slide, Crowsnest, Alberta: Bull. Can. Petrol. Geol. 41 (2), 232-243.

Kanasewich, E.R., 1986, Turtle Mountain Seismicity Study Phase II (Alberta Environment Research Proposal RMD 80-32G): Report to Alberta Environment.

Kendall, J., Al-Anboori, A., Caddick, J., Teanby, N., 2005, Microseismic Monitoring and Seismic Anisotropy in Oilfields: EOS Trans. AGU, 86 (18), Jt. Assem. Suppl., Abstract #S34A-06.

Kitagawa, J. and Akaike, H., 1978, Procedure for the modeling of non-stationary time series: Ann. Inst. Statist. Math., 30, 351-363.

Kullback, S. and Leibler, R.A., 1951, On information and sufficiency: Ann. Inst. Statist. Math., 22, 79-86.

Langenberg, C.W., Pana, D. and Richards, B., 2005, Stratigraphy and Structural Geology of Turtle Mountain near Frank, Alberta: EUB/AGS internal report.

Lee, W.H.K. and Stewart, S.W., 1981, Principles and Applications of Microearthquake Networks. Academic Press, New York, NY, 293 pp.

Leonard, M., 2000, Comparison of Manual and Automatic Onset Time Picking: Bull. Seis. Soc. Am., 90 (6), 1384-1390.

Leonard, M., and Kennett, B.L.N., 1999, Multi-component autoregressive techniques for the analysis of seismograms: Phys. Earth Planet. Int., 113, 247-263.

Maeda, N., 1985, A method for reading and checking phase time in auto-processing system of seismic wave data: Zisin, 38 (2), 365-379 (in Japanese with English abstract).

Maxwell, S.C., Urbancic, T.I., 2001, The role of passive microseismic monitoring in the instrumented oil field: Leading Edge, 20, 636-639.

McConnell, R.G. and Brock, R.W., 1904, Report of the Great Landslide at Frank, Alberta, Canada: Canadian Department of the Interior, Annual Report, 1902-1903, Part 8, 17 pp.

Oye, V. and Roth, M., 2003, Automated seismic event location for hydrocarbon reservoirs: Computers & Geosciences, 29, 851-863.

Ozaki, T. and Tong, H., 1975, On the fitting of non-stationary autoregressive models in the time series analysis: Proc. 8th Hawaii Inter. Conf. Sys. Sc., Western Periodical Company.

Pearce, R.G., and Barley, B.J., 1977, The effect of noise on seismograms: Geophys. J. Roy. Astron. Soc., 48, 543-547.

Pinnegar, C.R. and Mansinha, L., 2003, The S-transform with windows of arbitrary and varying shape: Geophysics, 68 (1), 381-385.

Rutledge, J.T., Phillips, W.S., Schuessler, B.K., 1998, Reservoir Characterization using oil-production-induced microseismicity, Clinton county, Kentucky: Tectonophysics, 289, 129-152.

Saari, J., 1991, Automated phase picker and source location algorithm for local distances using a single three-component seismic station: Tectonophysics, 189, 307-315.

Sleeman, R., and van Eck, T., 1999, Robust automatic P-phase picking: an online implementation in the analysis of broadband seismogram recordings: Phys. Earth Planet. Int. 113, 265-275.

Stewart, R.R., Bland, H., Chen, Z., and Thurston, J., 2004, A microseismic monitoring system and investigation, Turtle Mtn, Alberta: Report submitted to Alberta Environment by Gennix Technology Corp.

Stewart, R.R., Huddleston, P.D., and Kan, T.K., 1984, Seismic versus sonic velocities: A vertical seismic profiling study: Geophys., 49 (8), 1153-1168.

Takanami, T. and Kitagawa, G., 1988, A new efficient procedure for the estimation of onset times of seismic waves: J. Phys. Earth, 36, 267-290.

Takanami, T. and Kitagawa, G., 1991, Estimation of the arrival times of seismic waves by multivariate time series models: Ann. Inst. Statist. Math., 43, 407-433.

Takanami, T. and Kitagawa, G., 1993, Multivariate time-series models to estimate the arrival times of S waves: Computers and Geosciences, 19, 295-301.

Takanami, T.,1991, A Study of Detection and Extraction Methods for Microearthquake Waves by Autoregressive Models: J. Fac. Sci., Hokkaido Univ., Ser. VII (Geophysics), 9 (1), 67-196.

Talebi, S., Nechtschein, S. and Boone, T.J., 1998, Seismicity and Casing Failures Due to Steam Stimulation in Oil Sands: Pure Appl. Geophys., 153, 219-233.

Tong, C. and Kennett, B.L.N., 1996, Automatic seismic event recognition and later phase identification for broadband seismograms: Bull. Seis. Soc. Am., 86, 1896-1909.

Vidale, J.E., 1986, Complex polarization analysis of particle motion: Bull. Seis. Soc. Am., 76, 1393-1405.

Wiechert, D.H., and Horner, R.B., 1981, Microseismic monitoring in Blairmore, Alberta: Pacific Geoscience Centre, Dept. Energy, Mines, Resources: Internal report 81-4.

Withers, M., Aster, R., Young, C., Beiriger, J., Harris, M., Moore, S., and Trujillo, J., 1998, A comparison of selected trigger algorithms for automated global seismic phase and event detection: Bull. Seis. Soc. Am., 88, 95-106.